107080

ANL-02/05

ARGONNE RECORD COPY
DO NOT DESTROY

Energy Technology Division
Energy Technology Division
Energy Technology Division
Energy Technology Division
Energy Technology Division
Energy Technology Division
Energy Technology Division
Energy Technology Division
Energy Technology Division
Energy Technology Division
Energy Technology Division
Energy Technology Division
Energy Technology Division
Energy Technology Division
Energy Technology Division
Energy Technology Division
Energy Technology Division
Energy Technology Division
Energy Technology Division
Energy Technology Division
Energy Technology Division
Energy Technology Division
Energy Technology Division
Energy Technology Division
Energy Technology Division
Energy Technology Division
Energy Technology Division
Energy Technology Division
Energy Technology Division
Energy Technology Division
Energy Technology Division

Study of Metal Dusting Phenomenon and Development of Materials Resistant to Metal Dusting:

Annual Report

K. Natesan
Energy Technology Division

February 2002

Argonne National Laboratory, Argonne, Illinois 60439
operated by The University of Chicago
for the United States Department of Energy under Contract W-31-109-Eng-38

Energy Technology Division
Energy Technology Division
Energy Technology Division
Energy Technology Division
Energy Technology Division
Energy Technology Division
Energy Technology Division
Energy Technology Division
Energy Technology Division
Energy Technology Division

Argonne National Laboratory, with facilities in the states of Illinois and Idaho, is owned by the United States Government and operated by The University of Chicago under the provisions of a contract with the Department of Energy.

DISCLAIMER

This report was prepared as an account of work sponsored by an agency of the United States Government. Neither the United States Government nor any agency thereof, nor The University of Chicago, nor any of their employees or officers, makes any warranty, express or implied, or assumes any legal liability or responsibility for the accuracy, completeness, or usefulness of any information, apparatus, product, or process disclosed, or represents that its use would not infringe privately owned rights. Reference herein to any specific commercial product, process, or service by trade name, trademark, manufacturer, or otherwise, does not necessarily constitute or imply its endorsement, recommendation, or favoring by the United States Government or any agency thereof. The views and opinions of document authors expressed herein do not necessarily state or reflect those of the United States Government or any agency thereof, Argonne National Laboratory, or The University of Chicago.

Available electronically at http://www.doe.gov/bridge

Available for a processing fee to U.S. Department of Energy and its contractors, in paper, from:

U.S. Department of Energy
Office of Scientific and Technical Information
P.O. Box 62
Oak Ridge, TN 37831-0062
phone: (865) 576-8401
fax: (865) 576-5728
email: reports@adonis.osti.gov

ARGONNE NATIONAL LABORATORY
9700 South Cass Avenue
Argonne, Illinois 60439-4838

ANL-02/05

Study of Metal Dusting Phenomenon and Development of Materials Resistant to Metal Dusting

ANNUAL REPORT
For the Period January to December 2001

Prepared by

K. Natesan
Energy Technology Division

February 2002

Work supported at Argonne National Laboratory

by

THE U. S. DEPARTMENT OF ENERGY
Office of Industrial Technologies
Project Manager: C. Sorrell

CONTENTS

FIGURES iv
TABLES viii
ABSTRACT 1
PROJECT DESCRIPTION 1
OBJECTIVES 2
STEERING GROUP AND MTI PROJECT MEETINGS 2
APPROACH 3
PROJECT TASKS 4
BACKGROUND 4
Process Environments 4
Metal Dusting Mechanism 7
TECHNICAL PROGRESS 8
Gas Phase Reactions 8
Carbon Activity Calculations 9
EXPERIMENTAL PROGRAM 13
Equipment Description 13
Materials 17
Specimen Preparation 19
TEST RESULTS AND DISCUSSION 20
Key Variables for Carbon Deposition and Metal Dusting 20
Characteristics of Carbon Deposits 23
Proposed Metal Dusting Mechanism 33
Metal Dusting of Pure Metals 35
Behavior of Fe- and Ni-Base Alloys 42
DISCUSSION OF METAL DUSTING INITIATION 53
PERFORMANCE OF PACK-DIFFUSION COATINGS 61
PROJECT SUMMARY 66
ACKNOWLEDGMENTS 70
REFERENCES 70

FIGURES

1. Carbon activity curves calculated as a function of temperature for Gas Mixture 1. 10
2. Carbon activity curves calculated as a function of temperature for Gas Mixture 2. 11
3. Carbon activity curves calculated as a function of temperature for Gas Mixture 3. 11
4. Schematic diagram for three test facilities set up for metal dusting experiments. 14
5. Schematic diagram of furnace assembly and gas flow arrangement used for metal dusting experiments. 15
6. Schematic diagram of steam and gas flow scheme used for metal dusting experiments. 16
7. Schematic diagram of quartz specimen holder and test coupon arrangement used for metal dusting experiments. 17
8. Macrophotograph of specimens after 100-h exposure in Runs 2 and 3 conducted at 593°C. 22
9. Macrophotograph of specimens after 100-h exposure in Runs 4 and 5 conducted at 704°C. 22
10. Macrophotograph of specimens after 5-h exposure in Runs 6 and 7 conducted at 593°C. 23
11. Macrophotograph of specimens after 72-h exposure in Runs 8 and 9 conducted at 593°C. 24
12. Structure of graphite. 24
13. Raman spectra of carbon "soot" from Runs 4, 5, and 7 along with Raman spectra of polycrystalline graphite and pencil "lead". 26
14. XRD pattern of coke and surface layer on iron sample after exposure to Gas 4 at 593°C for 100 h. 27
15. Temperature dependence of magnetization of metal dusting product obtained in Run 4 at 593°C. 28
16. Peak widths of [002] diffraction from graphite and coke. 28
17. Peak widths of [002] diffraction from glassy carbon, graphite, and coke. 29
18. Raman spectra of graphite, glassy carbon, and coke made at 593°C and 704°C. 30

19. Raman spectra of coke made at 593°C and 704°C. 31
20. Raman spectra of coke, carbon on alloy sample surface, and carbon in sample defects. 32
21. SEM cross section of Fe-Al alloy after metal dusting experiment at 593°C. 32
22. Proposed process for carbon crystallization after deposition in metal-dusting environment. 34
23. Proposed process for catalytic crystallization. 34
24. Weight change data for pure Fe specimens exposed in Runs 1 through 7. 36
25. Post test SEM photomicrograph of metallographic cross section of iron. 37
26. Schematic of metal dusting process in the degradation of Fe. 37
27. Raman spectra for carbon adhered to Ni specimens from Runs 3-7. 39
28. SEM photomicrographs of Ni surfaces before and after exposure in a metal dusting experiment. 39
29. SEM photomicrograph of cross section of Ni after testing. 40
30. Typical XRD pattern of the product of metal dusting experiment involving Ni. 40
31. XRD [002] diffraction peaks for graphite, coke, and carbon on the surface of Ni. 41
32. XRD [002] diffraction peaks for carbon black and coke. 41
33. XRD [002] diffraction peaks of glassy carbon with and without 10% Ni. 42
34. Macrophotographs of Fe-base alloy specimens after 1000-h exposure at 593°C in Run 15 in Gas 2 with 23.1 vol.% H_2O and Run 19 in Gas 2 with 2 vol.% H_2O. 43
35. SEM photomicrographs of surfaces of T91, 803, APMT, and 153MA after 1000-h exposure in Run 15. 44
36. SEM photomicrographs of surfaces of Alloy 800, 310 ss, 321 ss, and MA956 after 1000-h exposure in Run 15. 45
37. SEM photomicrographs of surfaces of 253MA, 321L, 4C54, and 38815 after 1000-h exposure in Run 15. 45
38. Higher magnification SEM photomicrographs of surfaces of MA956, 38815, 253MA, and APMT after 1000-h exposure in Run 15. 46
39. SEM photomicrographs of surfaces of 600, 601, 690, and 617 after 1000-h exposure in Run 16. 46
40. SEM photomicrographs of surfaces of 602CA, 214, 230, and 45TM after 1000-h exposure in Run 16. 47

41. SEM photomicrographs of cross sections of T91, 800, and 321 after 1000-h exposure in Run 15. 48

42. SEM photomicrographs of cross sections of 600, 690, 602CA, and 45TM after 1000-h exposure in Run 16. 48

43. Raman spectra for carbon adhered to several alloys with different Cr contents after 1000-h exposure in a metal dusting environment in Run 15 at 593°C. 49

44. Raman spectra for surfaces of several Fe-base alloys with different Cr contents after 1000-h exposure in a metal dusting environment in Run 15 at 593°C. 50

45. Raman spectra for surfaces of several Ni-base alloys with different Cr contents after 1000-h exposure in a metal dusting environment in Run 16 at 593°C. 50

46. Raman spectra for surfaces of several 300-series stainless steel alloys and Alloy 800 after 1000-h exposure in a metal dusting environment at 593°C. 51

47. Raman spectra for surfaces of several 300-series stainless steel alloys and Alloy 800 after 1000-h exposure in a metal dusting environment at 593°C. 52

48. Raman spectra for surfaces of several Al-containing alloys after 1000-h exposure in a metal dusting environment at 593°C. 54

49. 593°C Raman spectra for surfaces of several Al-containing alloys after 1000-h exposure in a metal dusting environment at 593°C. 55

50. Raman spectra for surfaces of several Si-containing alloys after 1000-h exposure in a metal dusting environment at 593°C. 56

51. Comparison of Raman spectra for surfaces of several Si-containing alloys after 1000-h exposure in a metal dusting environment at 593°C. 57

52. Oxygen/carbon thermochemical diagrams for Fe, Cr, and Ni calculated for 593°C. 60

53. SEM photomicrograph of cross section of alonized T22 steel and EDX elemental depth profiles of Al and Fe for the specimen in the as-coated condition. 63

54. SEM photomicrograph of cross section of alonized 321 stainless steel and EDX elemental depth profiles of Al, Fe, Cr, and Ni for the specimen in the as-coated condition. 63

55. SEM photomicrograph of cross section of alonized Alloy 800 and EDX elemental depth profiles of Al, Fe, Cr, and Ni for the specimen in the as-coated condition. 64

56. SEM photomicrograph of cross section of ChromePlexed T22 steel and EDX elemental depth profiles of Si, Fe, and Cr for the specimen in the as-coated condition. 64

57. SEM photomicrograph of cross section of ChromePlexed 321 stainless steel and EDX elemental depth profiles of Si, Fe, Cr, and Ni for the specimen in the as-coated condition. 65

58. SEM photomicrograph of cross section of ChromePlexed Alloy 800 and EDX elemental depth profiles of Si, Fe, Cr, and Ni for the specimen in the as-coated condition. 65

59. SEM photomicrograph of surface of alonized T22 steel after oxidation at 900°C in air and after oxidation at 900°C followed by metal dusting exposure for 142 h at 593°C. 66

60. SEM photomicrograph of surface of alonized 321 stainless steel after oxidation at 900°C in air and after oxidation at 900°C followed by metal dusting exposure for 142 h at 593°C. 67

61. SEM photomicrograph of surface of alonized Alloy 800 after oxidation at 900°C in air and after oxidation at 900°C followed by metal dusting exposure for 142 h at 593°C. 67

62. SEM photomicrograph of surface of ChromePlexed T22 steel after oxidation at 900°C in air and after oxidation at 900°C followed by metal dusting exposure for 142 h at 593°C. 68

63. SEM photomicrograph of surface of ChromePlexed 321 stainless steel after oxidation at 900°C in air and after oxidation at 900°C followed by metal dusting exposure for 142 h at 593°C. 68

64. SEM photomicrograph of surface of ChromePlexed Alloy 800 after oxidation at 900°C in air and after oxidation at 900°C followed by metal dusting exposure for 142 h at 593°C. 69

TABLES

1. Chemical compositions of gas mixtures relevant for metal dusting study. 9
2. Carbon activity values at 593 and 704°C based on reactions 1, 2, and equilibrium. 10
3. Nominal chemical compositions of alloys selected for the experimental program. 18
4. Experimental conditions for laboratory runs. 21
5. Crystallite dimension and interlayer plane distance of graphite, coke, and glassy carbon. 29
6. Gas chemistries used in metal dusting research. 58
7. Carbon activity and oxygen partial pressure values at 593°C for gas mixtures used by various researchers. 59

ABSTRACT

The deposition of carbon from cabonaceous gaseous environments is prevalent in many chemical and petrochemical processes such as reforming systems, syngas production systems, iron reduction plants, and others. One of the major consequences of carbon deposition is the degradation of structural materials by a phenomenon known as "metal dusting." There are two major issues of importance in metal dusting. First is formation of carbon and subsequent deposition of carbon on metallic materials. Second is the initiation of metal dusting degradation of the alloy. Details are presented on a research program that is underway at Argonne National Laboratory to study the metal dusting phenomenon from a fundamental scientific base involving laboratory research in simulated process conditions and field testing of materials in actual process environments. The project has participation from the U.S. chemical industry, alloy manufacturers, and the Materials Technology Institute, which serves the chemical process industry.

PROJECT DESCRIPTION

Project Title: Study of Metal Dusting Phenomenon and Development of Materials Resistant to Metal Dusting

Principal Investigators: Ken Natesan (Argonne National Laboratory)
Ken Baumert (Air Products and Chemicals Inc.)

ANL Participants in the Project: K. Natesan, Z. Zeng, W. K. Soppet, D. L. Rink, and V. Maroni

Organizations Participating in the Project:

- Materials Technology Institute
- Air Products and Chemicals Inc.
- ExxonMobil Chemical Company
- DuPont Chemical Company
- Allied Signal (part of Honeywell)
- Haynes International
- AvestaPolarit
- Sandvik Steel
- Duraloy Technologies
- Special Metals
- Krupp VDM
- Schmidt & Clemens
- Alon Surface Technologies
- MetalTek International
- Spectrum Metals
- Allegheny Ludlum

OBJECTIVES

The overall objective of this project is to study the metal dusting phenomenon from a fundamental scientific base involving laboratory research in simulated process environments and field testing of materials in actual process environments with participation from the U.S. chemical industry, alloy manufacturers, and the Materials Technology Institute (MTI), which serves the chemical process industry. Another objective is to develop a user-friendly knowledge base of materials/corrosion information for application in the chemical and petrochemical industries.

The effort at Argonne National Laboratory (ANL) involves testing off-the-shelf and surface-engineered materials in simulated process environments, developing a user-friendly computerized database of metal dusting/corrosion/mechanical properties of materials, and gaining a fundamental understanding of the metal dusting and associated carburization phenomenon. As part of this effort, alloy manufacturers contributed materials for both laboratory and field testing, participated in a Steering Committee for the project, and conducted in-house evaluation of materials.

STEERING GROUP AND MTI PROJECT MEETINGS

A list of Steering Committee meetings/teleconferences and MTI meetings, in which the project was discussed, is given below:

December 10, 1999	Teleconference
January 25, 2000	Air Products and Chemicals Inc., Allentown, PA
February 21, 2000	MTI meeting, Clearwater Beach, FL
March 16, 2000	Teleconference
June 5, 2000	MTI meeting in St. Louis, MO
July 28, 2000	DuPont Experimental Station, Wilmington, DE
August 31, 2000	Teleconference
October 10, 2000	Teleconference
October 23, 2000	MTI meeting, Charlotte, NC
January 29, 2001	Argonne National Laboratory, Argonne, IL
February 26, 2001	MTI meeting, Clearwater Beach, FL
March 14, 2001	In conjunction with NACE meeting, Houston, TX
June 4, 2001	MTI meeting, Memphis, TN
June 29, 2001	Teleconference

APPROACH

The technical approach involves several steps conducted either sequentially or in parallel and includes participation of MTI members and Argonne National Laboratory in the organization of the work plan and in the conduct of the proposed research to address the metal dusting issue. MTI member companies supplied their in-house metal-dusting data collected over the years and will make available, in the future, their facilities for exposure of candidate alloys and surface-engineered materials for evaluation and assessment.

The approach involves characterization, using thermodynamic modeling, of environments prevalent in several process streams in terms of their chemical activities for carbon, oxygen, and other elements. The results are used to assess the chemical potential and temperature windows for metal dusting to initiate and propagate in metallic materials. The thermodynamic assessment would also establish the consequences of equilibrium and nonequilibrium gas chemistries on the metal dusting process.

The corrosion behavior of commercial alloys in chemical process industries is being evaluated to identify conditions in which metal dusting occurs in practice. MTI has collected metal dusting data (both proprietary and published data from the open literature) for several materials from its member companies. This information is used to establish the effects of alloy chemistry, temperature range, pressure range, exposure time, and exposure environment on the corrosion process by metal dusting.

Bench-scale laboratory experiments are conducted at Argonne with candidate commercial alloys, developmental alloys, and surface-engineered materials, including coatings. Surface modification includes development of oxide scales on candidate alloys by exposures in air and low-pO2 environments. Surface engineering includes development of pack diffusion coatings and claddings. Experiments are conducted in a wide range of gas chemistries and temperatures that encompass the environments prevalent in various process systems, such as in reformers for the production of hydrogen, ammonia, and methanol. Results are used to establish the conditions for the onset of metal dusting and to evaluate the influence of alloy chemistry on the occurrence of metal dusting.

Candidate commercial alloys, developmental alloys, and surface-engineered alloys will be exposed, at a later date, in several locations in process streams from production plants for hydrogen, methanol, ammonia, and other hydrogen-bearing compounds. Microstructures of the exposed specimens are characterized to assess their propensity to metal dusting. The field-exposure results and the laboratory test data are used to develop performance envelopes for alloys in service with minimum risk of metal dusting.

PROJECT TASKS

Project research focuses on the following tasks:

- Characterize chemical process environments using computer modeling of gas phase reactions
- Perform corrosion testing of off-the-shelf candidate alloys in simulated metal dusting environments
- Develop surface-engineered materials based on results of corrosion tests
- Evaluate the role of system pressure in the initiation of corrosion/metal dusting of materials
- Perform corrosion tests on surface-engineered materials in simulated chemical environments over a wide temperature and pressure range
- Expose candidate alloys and surface engineered materials in several locations in pilot and/or production systems that produce hydrogen, methanol, syngas, and ammonia
- Select the best candidates from monolithic alloys and surface engineered materials and fabricate tube sections for exposure in pilot and/or production units for evaluation
- Develop a database on metal dusting, corrosion, and mechanical properties of materials

BACKGROUND

Process Environments

The predominant process for hydrogen production is steam reforming of light hydrocarbons e.g., natural gas, liquefied petroleum gas, naphtha, or refinery off-gases. This process has been used extensively in the past for hydrogen production and is expected to continue in most of the installations required to meet the increasing demand for hydrogen in the future. The demand for hydrogen is growing in many industries, and refineries in particular must increase hydrogen use to make products acceptable to the environment and to limit production of very heavy resid. Refiners consider hydrogen a

utility, and they emphasize availability, trouble-free response to changing demand, and low-cost investment.

Production capacity in hydrogen plants may range from <100 $N \cdot m^3/h$ to >100,000 $N \cdot m^3/h$. For larger capacities, from 1000 $N \cdot m^3/h$ and upward, hydrocarbons are the predominant feedstocks. The production processes may be partial oxidation or steam reforming; for both types of processes, the primary process step is followed by shift conversion and final purification of product hydrogen.

Production of synthesis gas (mixtures of carbon monoxide and hydrogen) is an important first step in the manufacture of numerous chemicals. The most common process for producing synthesis gas is steam reforming, where hydrocarbons are converted by reaction with steam over a nickel catalyst at high temperatures. The synthesis gas from the steam reformer is purified in order to meet the requirements of the downstream process. It can be separated into pure H_2, pure CO, H_2/CO mixtures, etc. Pure CO is required for the production of isocyanates, polycarbonates, and acetic acid, while for example, synthesis of oxo-alcohols requires an H_2/CO mixture with a molar ratio close to 1. By decreasing the steam/carbon ratio and by increasing the outlet temperature from the reformer furnace, great savings in feedstock consumption and in investment can be obtained.

The steam reformer is the heart of the unit for production of synthesis gas. In the steam reformer, hydrocarbon feedstock is reacted with steam to synthesis gas by the reactions:

$$C_nH_m + n\,H_2O = n\,CO + (n + m/2)\,H_2 \quad (1)$$

$$CH_2 + H_2O = CO + 2H_2 \quad (2)$$

$$CO + H_2O = CO_2 + H_2 \quad (3)$$

All higher hydrocarbons ($n \geq 2$) are completely and irreversibly converted by the first reaction, while in the next two reactions, the strongly endothermic methane-reforming reaction (2) and the exothermic shift reaction (3) are close to equilibrium in the outlet of the steam reformer. The reactions take place over a nickel catalyst placed inside metal tubes. The tubes are arranged in a furnace where burners firing on the outside of the tubes supply the heat.

Metal dusting is a catastrophic corrosion phenomenon that leads to the disintegration of structural metals and alloys into dust composed of fine particles of the metal/alloy and carbon. This phenomenon has been observed in the chemical and petrochemical industries, in reformer and direct-reduction plants, in processes that generate syngas, and in other processes where hydrocarbons or other strongly carburizing atmospheres

are present. Failures have been reported in ammonia plants since reduced energy requirements result in a lower steam/H_2 ratio, whereas CO/CO_2 ratios have tended to increase.

Metal dusting is a process of highly accelerated material wastage that is preceded by the saturation of a material with carbon. The phenomenon is typified by the disintegration of a material (iron- or nickel-base) to a mixture of carbon dust, metal particles, and possibly oxides and carbides. This is usually a localized form of attack, resulting in pits and grooves. Metal dusting occurs at intermediate temperatures of 400-800°C, but this type of corrosion is possible at any temperature at which the carbon activity (a_C) in the gas phase is >1. Such high carbon activities are prevalent in certain locations in several chemical processes, such as methanol production, hydrocarbon and ammonia synthesis, hydrogen production, and syngas generation. Several of these chemical systems have reported metal/component failures by metal dusting. For CO-H_2-H_2O mixtures, carbon activity, which is the thermodynamic driving force for metal dusting, increases with decreasing temperature. Carbon activity values >1000 can be obtained at 500°C in several of the process streams.

Materials can be protected against metal dusting by adding sulfur-containing compounds, such as H_2S, to the process gas. Sulfur in the gas "poisons" the metal surfaces and prevents both carbon ingress and graphite nucleation. However, in many catalytic processes, sulfur-bearing substances cannot be injected since they deactivate the catalysts. To prevent material wastage under such conditions, an appropriate material with high resistance to metal dusting is needed.

Important reactions, which can occur in the typical metal dusting environment, are:

$$2CO = CO_2 + C \quad (4)$$

$$H_2 + CO = H_2O + C \quad (5)$$

$$H_2O + CO = CO_2 + H_2 \quad (6)$$

$$H_2O + CH_4 = CO + 3H_2 \quad (7)$$

Reactions (4) and (5) can produce carbon; Reaction (6) deals with water-gas shift, and Reaction (7) with methane-steam reforming. The dominant reaction in a chemical process can be any one of the above reactions or a combination of them, and the carbon activity will be influenced by the dominant reaction, process temperature, and pressure. Most of the structural materials based on Fe, Ni, and Co are susceptible to this type of degradation even though the conditions of temperature, environmental chemistry, and incubation and kinetic factors for this occurrence may be different.

In a hydrogen plant, the major process components are the fuel gas reformer, process gas boiler, and high- and low-temperature shift reactors. The syngas from the reformer

contains various amounts of gases, such as H_2 (60%), CO (15%), CO_2 (5%), CH_4 (10%), steam (10%), and trace amounts of other compounds. It is produced primarily by steam reforming and partial oxidation of hydrocarbons at temperatures of 800-1400°C. The hot gases are contained in refractory-lined equipment and quenched to about 300°C in a waste-heat boiler or cooled by direct injection of water to the process stream. Most processes deliberately avoid transferring heat through the 800-400°C range because metal dusting occurs at these temperatures, and at present, no alloy can resist this type of corrosion over the long term. Consequently, the energy in high-temperature syngas is not recovered in an efficient manner.

Another example relevant to metal dusting is the formation of filamental coke in several petrochemical processes, which eventually leads to failure of heater alloys by metal dusting. The coke formation involves several sequential steps, such as dissociative chemisorption of hydrocarbon, stepwise dehydrogenation, surface and volume diffusion of carbon, carbide precipitation and transport under a temperature gradient, and regeneration of catalyst or decoking under oxidizing conditions. Further, the process entails cyclic deposition and decoking. Some models have been proposed in the literature for coke formation, which involves dissociative chemisorption and stepwise dehydrogenation leading to adsorption of C and H on the surface sites on the catalyst, diffusion of carbon through the metal and precipitation on the grain boundaries or at the metal/support interfaces, lifting of metal crystallites from the surface of the catalyst, and transport of crystallites to the top of the growing filaments.

Alternatively, C species may react on the surface to develop an encapsulating film, leading to the deactivation of the catalyst. Competition between C accumulation on the surface and C diffusion away from the active sites determines whether the catalyst becomes deactivated or not. This is determined by the composition of gas, hydrogen pressure, and temperature.

Metal Dusting Mechanism

Metal dusting is a high-temperature corrosion phenomenon that occurs in Fe-, Co-, or Ni-base alloys in strongly carburizing gas atmospheres at carbon activities (a_C) >1 in the temperature range of 425-900°C (≈800-1600°F).[1-9] During the metal dusting process, corrosion of metals and alloys occurs, accompanied by formation of fine metal carbide or pure metal and carbon dust. Dusting-related failures have occurred most often in the petroleum and petrochemical industries. This deterioration has been studied for more than 50 years,[10] but its mechanism and driving force are not evident in all cases and no clear approach is currently available to mitigate this problem.

Hochman proposed the following mechanism for the metal dusting of iron: (a) carbon from the gas phase deposits on the metal surface and dissolves in the metal; (b) cementite forms as carbon diffuses into the Fe and the metal becomes supersaturated; and (c) metastable cementite decomposes to Fe and graphite.[4] Grabke and coworkers

conducted studies and provided additional details on the possible mechanism.[5-7, 9] According to them, the final product is graphite and Fe. However, there is no conclusive evidence that metallic Fe is present in every case of metal dusting. It is not clear what drives the formation and decomposition of cementite under the same conditions of temperature, pressure, and composition. It is easy to understand that graphite crystallizes from a supersaturated solution. Nevertheless, whether or not recrystallization would lead to decomposition of cementite is not yet clear. The formation and decomposition of chemical bonds require a sizeable free energy change. Cementite is a product of metal dusting, but it is not clear that this compound is essential to initiate metal dusting or is only a product of this step. Furthermore, the susceptibility of even complex Fe- and Ni-base alloys, in which cementite rarely can form, to this mode of degradation suggests that the mechanism is fairly complex and that a single mechanism may not be operative in all cases.

Even though metal dusting is widely prevalent, the general approach to minimize the problem in industry is the unsatisfactory one of excluding the temperature/process conditions that are conducive for the attack. Fixes, such as sulfur poisoning of surface sites and preoxidation of alloy to stabilize chromia on high-Cr alloys, are applied case-by-case, primarily based on past experience of materials performance in such environments.

Several other examples can be cited, such as hydrogen production by reforming reaction, but it is evident from the information presented above that metal dusting of materials is an issue in several chemical/petrochemical processes, and a detailed understanding of the causes for metal dusting and long-term solutions to minimize the problem could lead to substantial improvements in process efficiency, materials performance, process downtime, and reliability of operation. Further, the knowledge base developed in the U.S. will aid in the advancement of processes in the domestic industry, lead to development of better and improved metal-dusting-resistant alloys, and result in establishment of a data bank for selecting suitable materials for application in different process environments.

TECHNICAL PROGRESS

Gas Phase Reactions

Chemical process environments were characterized by computer modeling of gas-phase reactions under both equilibrium and nonequilibrium conditions. Calculations were made to evaluate carbon activities for different gas mixtures as a function of temperature at atmospheric pressure (14.7 psia) and at plant system pressures. Chemical compositions are listed in Table 1 for several gas mixtures that include the reformer streams and laboratory simulation environments. Carbon deposition process can be influenced by two possible reactions, as follows:

Table 1. Chemical compositions of gas mixtures relevant for metal dusting study

	Composition in mol %						
Gas species	Gas 1	Gas 2	Gas 3	Gas 4	Gas 5	Gas 6	Gas 7
CH_4	4.1	1.1	0.2	-	-	-	-
CO	7.2	18	8.4	17.5	17.6	12.7	70.0
CO_2	5.7	5.6	5	8.3	8.3	10.1	4.0
H_2	43.8	52	36.3	74.2	72.2	77.2	25.25
H_2O	39.2	23	35	0	1.96	0	0.007
N_2	-	-	15	-	-	-	-
Ar	-	-	0.1	-	-	-	-

Gases 1, 2,and 3: Reformer outlet gases.

Gases 4, 5, and 6: Used in ANL experiments.

Gas 7: Used in Special Metals Program.

$$CO(g) + H_2(g) = C + H_2O(g) \quad (1)$$

$$2CO(g) = C + CO_2(g) \quad (2)$$

Since the gas composition is maintained fairly constant during the passage through the waste-heat boiler, either Reaction 1 or Reaction 2 may dictate the carbon activity in the stream at different temperatures. If it is dictated by Reaction 1, the carbon activity will be directly proportional to H_2 and CO partial pressures and inversely proportional to H_2O partial pressure. On the other hand, if the carbon activity is dictated by Reaction 2, then it will be directly proportional to the square of the CO partial pressure and inversely proportional to CO_2 partial pressure. In addition, if gas phase equilibrium does prevail, albeit at high temperatures and/or for long residence times, then the calculated carbon activity value will be the same (i.e., irrespective of Reaction 1 or 2) since thermodynamically the gas composition will adjust to give the most stable (lowest free energy) composition. Therefore, carbon activity was calculated as a function of temperature from 496°C or 925°F to the maximum test temperature and for 1 atm to the maximum test pressure for various gas mixtures (Table 1) assuming Reaction 1 or 2 is dominant and the gas phase is in thermodynamic equilibrium.

Carbon Activity Calculations

Table 2 lists the carbon activity values calculated for the seven gas mixtures (Table 1) at 593 and 704°C (1100 and 1300°F), based on whether Reaction 1 or 2 was dominant or equilibrium between different gas species prevailed at the elevated temperature. Figures 1-3 show plots of carbon activity as a function of temperature for the three gas mixtures listed in Table 1. Figure 1 shows six curves for Gas Mixture 1, as follows:

Table 2. Carbon activity values at 593°C (1100°F) and 704°C (1300°F) based on reactions 1, 2, and equilibrium. Calculated for gas mixtures listed in Table 1.

	593°C (1100°F)			704°C (1300°F)		
Gas #	Rxn 1	Rxn 2	Eqm	Rxn 1	Rxn 2	Eqm
1	0.4	1.2	0.3	0.05	0.08	0.09
2	2.0	7.9	0.7	0.24	0.53	0.25
3	0.4	1.9	0.2	0.05	0.13	0.04
4	∞	5.0	1.3	∞	0.34	0.8
5	32.3	5.0	1.2	3.8	0.34	0.7
6	∞	2.2	0.01	∞	0.15	0.02
7	117.4	165.4	32.6	13.8	11.1	6.2

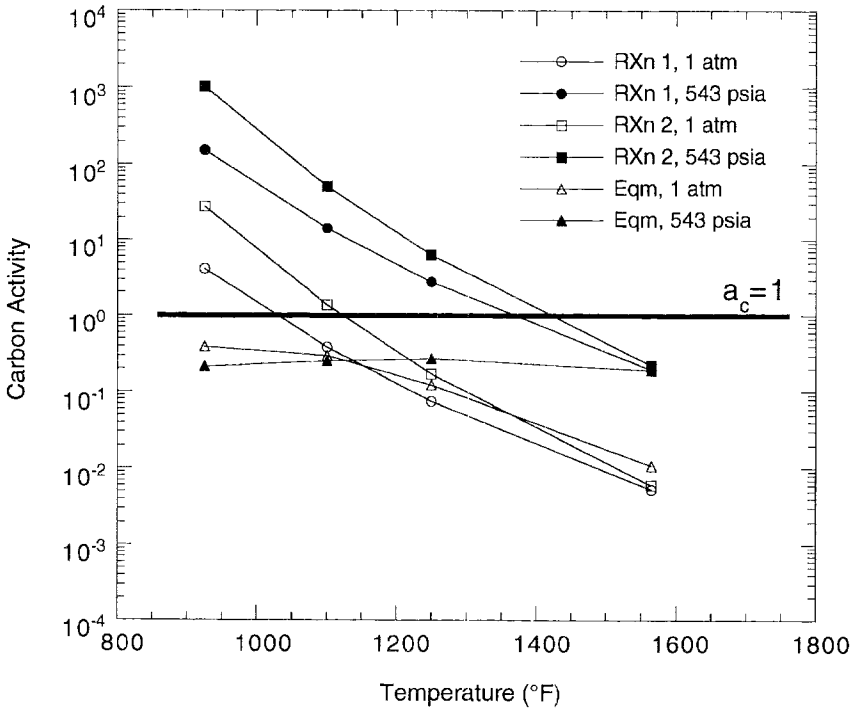

Fig. 1. Carbon activity curves calculated as a function of temperature for Gas Mixture 1.

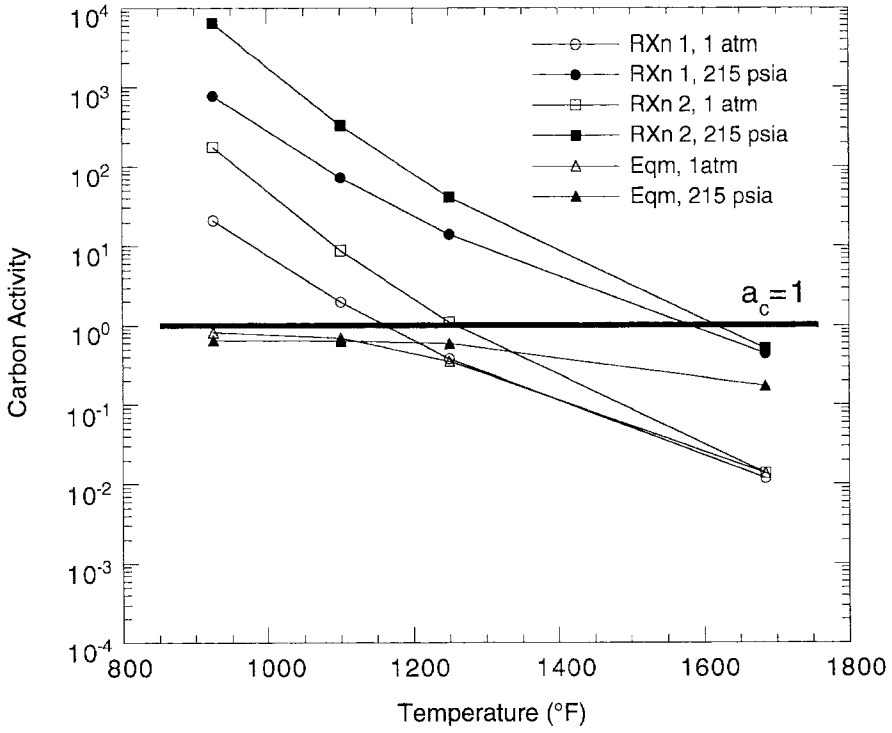

Fig. 2. Carbon activity curves calculated as a function of temperature for Gas Mixture 2.

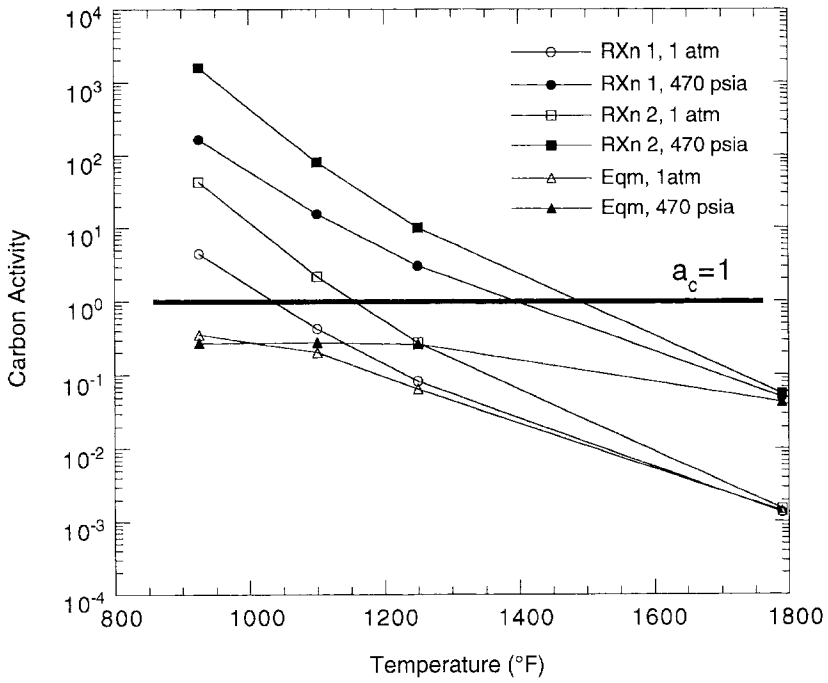

Fig. 3. Carbon activity curves calculated as a function of temperature for Gas Mixture 3.

Case 1:	Reaction 1 dominant, P = 1 atm (14.7 psia)
Case 2:	Reaction 1 dominant, P = 37 atm (543, psia)
Case 3:	Reaction 2 dominant, P = 1 atm (14.7 psia)
Case 4:	Reaction 2 dominant, P = 37 atm (543 psia)
Case 5:	Equilibrium condition, 1 atm (14.7 psia)
Case 6:	Equilibrium condition, P = 37 atm (543 psia)

Similar curves are shown in Fig. 2 for Gas Mixture 2, and in Fig. 3 for Gas Mixture 3. The maximum pressure values for Gas Mixtures 2 and 3 are 15 atm (215 psia) and 32 atm (470 psia), respectively.

The implications of the carbon activity calculations are as follows:

1. Under nonequilibrium conditions, Reaction 1 at 1 atm pressure results in the lowest carbon activity for all three reformer gas mixtures. Even under these conditions, the carbon activity is 1 or higher at temperatures below ≈565°C (≈1050°F) for Gas Mixtures 1 and 3 and below ≈621°C (≈1150°F) for Gas Mixture 2. At 496°C (925°F), the carbon activity values are ≈4 for Gas Mixtures 1 and 3 and ≈20 for Gas Mixture 2. These carbon activities can result in carbon deposition at 496°C (925°F) and may lead to metal dusting of several alloys, depending on the incubation time and alloy composition.

2. Reaction 2 always results in higher carbon activity. This trend is evident at all temperatures and pressures for the present calculations. Furthermore, this trend is independent of the gas mixture. The differences in the absolute value of the carbon activity established under Reaction 1 versus Reaction 2 control can be used to assess the role of these reactions in carbon deposition and associated metal dusting. For example, if an experiment is run in Gas Mixture 1 at 579°C (1075°F) and 1 atm, Reaction 1 control (with a_C of ≈0.6) would result in no carbon deposition, whereas Reaction 2 control (with a_C of ≈3) would result in carbon deposition. If a metal-dusting-susceptible alloy is used in this experiment, the results will clarify the role of Reaction 1 versus 2 in the carbon deposition/metal dusting process..

3. Increased system pressure increases a_C calculated for both reactions, irrespective of the gas composition. The carbon activities increase in direct proportion to the total pressure, and the values could be extremely large at lower temperatures. Furthermore, the effect of increased pressure is to widen the temperature window in which $a_C >> 1$. For example, in Gas Mixture 1 with

Reaction 1 control, an increase in pressure from 1 atm (14.7 psia) to 37 atm (543 psia) increases the temperature window with a_C>1 from 427-565°C (800-1050°F) to 427-732°C (800-1350°F). This assumes that temperatures <427°C (800°F) are too low to initiate metal dusting degradation, even though a_C values are high.

4. Calculations also indicate that under equilibrium conditions, all reformer gas mixtures exhibit a_C less than 1 (even at high pressures); therefore, no deposit of carbon and associated metal dusting should occur. Since carbon deposition and metal dusting of structural alloys are widely observed in reformer systems, the gas mixtures in these systems are not really in equilibrium, and a_C is established by individual reactions and is dictated by the reformer effluent gas composition.

5. Calculations further show that experiments need to be conducted under nonequilibrium gas chemistry to deposit carbon (coke) and also allow sufficient incubation time for metal dusting to begin.

6. For Gas Mixtures 4 and 5, a_C will be >1 if Reaction 1 is dominant. If Reaction 2 is dominant, a_C will be >1 at 593°C (1100°F) and <1 at 704°C (1300°F).

Results from these analyses were used to select gas compositions and temperatures for the experimental effort on metal dusting of structural alloys.

EXPERIMENTAL PROGRAM

Equipment Description

In all, five experimental systems were used in the metal dusting experiments. Two existing systems at ANL were modified to accommodate the requirements of the program. Each of the modified systems consisted of a horizontal, tubular, high-temperature furnace capable of operation up to 900°C. The reaction chamber, with gas inlet/outlet fittings, fabricated from quartz was positioned within the furnace chamber. The ends of the reaction chamber had specially designed flanges with O-ring seals. A chromel-alumel thermocouple, inserted from one end of the reaction chamber, was used to monitor the specimen temperature. Specimens were suspended from quartz rods held on the top of a high-purity alumina boat. The specimens and the boat were positioned in the constant-temperature section of the reaction chamber. High-purity gases such as CO, CO_2, CH_4, and H_2 were procured and piped into the reaction chamber through flow meters to obtain the desired composition. In some experiments, H_2 gas was bubbled through a water bath to saturate the H_2 with water prior to entering the reaction chamber. Upon completion of the experiments, the specimens and the carbon accumulated on the specimens and in the boat were removed for detailed microstructural, X-ray, and Raman analysis.

While the two systems described above enabled study of the key variables in metal dusting research, additional facilities were needed for long-term testing of metallic alloys, surface-engineered materials, and coatings. For this purpose, three new systems were designed and assembled in a metal dusting research laboratory. Figure 4 shows a schematic diagram for the three test facilities set up for metal dusting experiments. The three environmental exposure test fixtures are positioned horizontally on a laboratory bench top in a staggered linear arrangement with a common gas supply. Each test fixture consists of a quartz retort chamber (74-cm length, 5-cm OD, 0.32-cm thick), which was centered in a 30-cm-diameter resistive heating furnace. A Barber-Coleman Model 560 three-mode controller is used to control the furnace temperature. The ends of the quartz retort tube are closed by Type 316 stainless steel (SS) flange caps with an O-ring seal. The flange caps provide port fittings for the gas flow, steam/vapor preheater, and ceramic thermowells used for measurements of specimen temperature. Figure 5 shows a schematic diagram for the furnace assembly and gas flow arrangement used for the metal experiments.

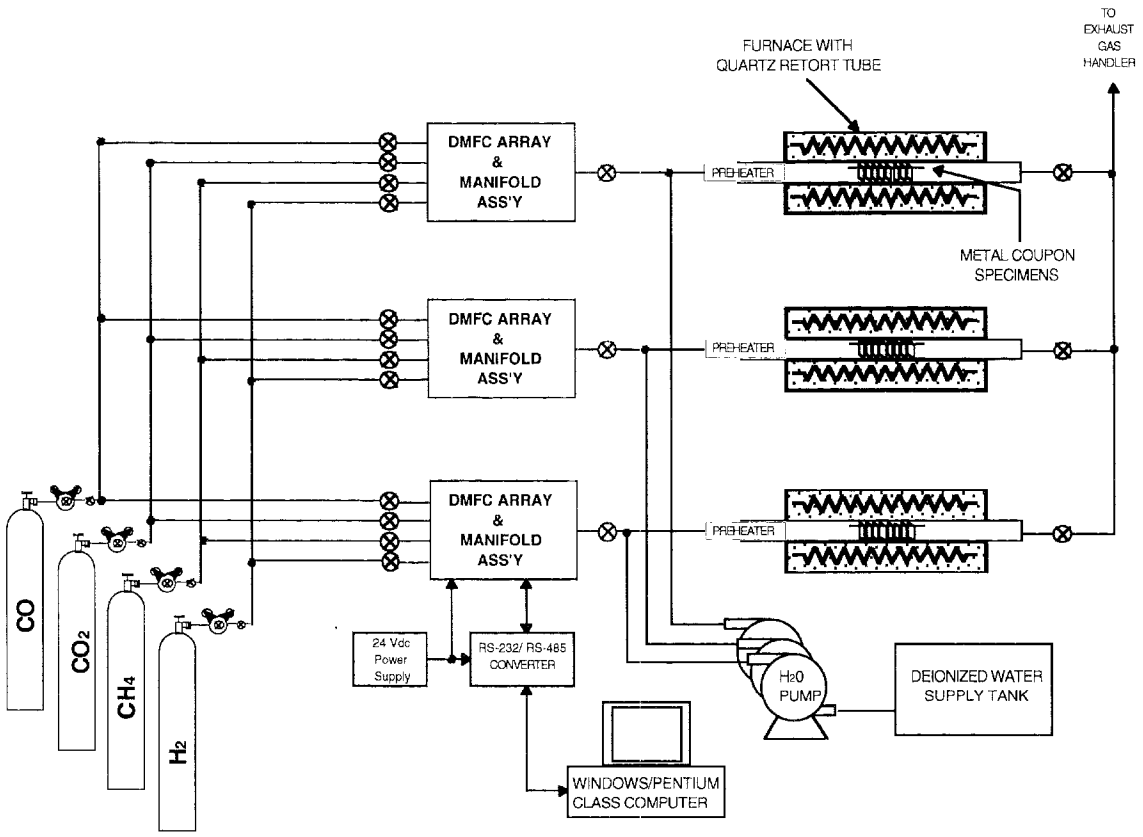

Fig. 4. Schematic diagram for three test facilities set up for metal dusting experiments.

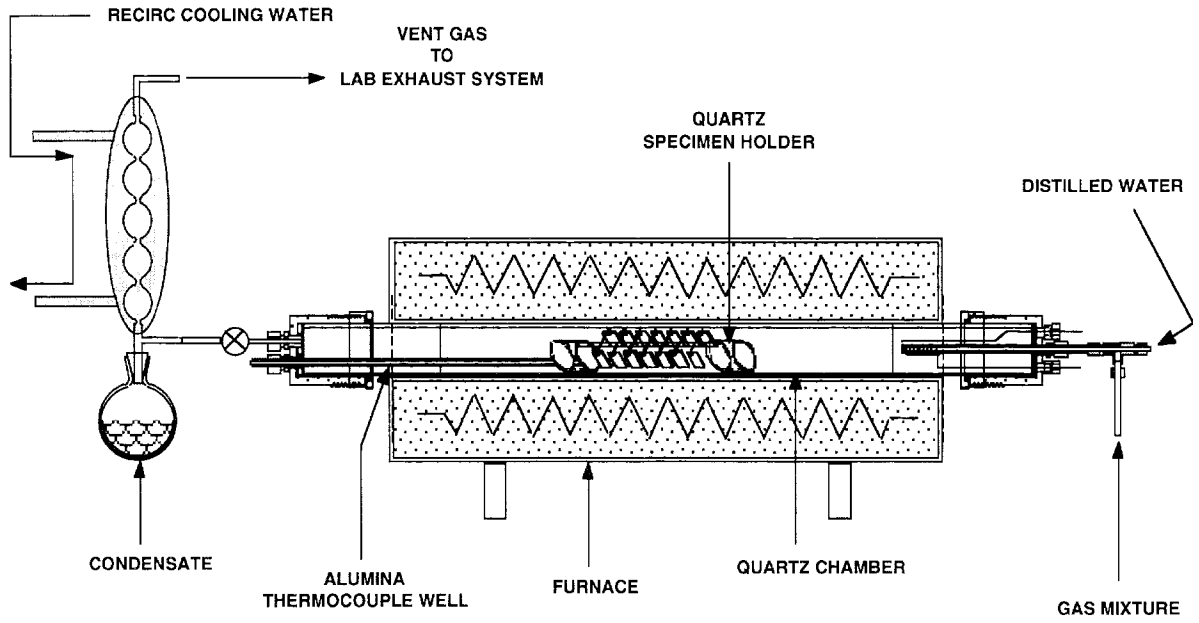

Fig. 5. Schematic diagram of furnace assembly and gas flow arrangement used for metal dusting experiments.

The gas that flows through the retort chamber has various ratios of H_2, CH_4, CO, CO_2, and steam/water vapor. Laboratory-grade compressed gases are supplied from AGA Gas Co. in industry standard 1A size (136 atm and 4.3 m^3 internal volume) cylinders. Each gas is piped to the reaction chamber through a low-pressure manifold line that is fed from a two-stage gas pressure-reducing regulator with a flash arrestor and a solenoid shut-off valve. The solenoid valves are controlled by a gas-leak detection system manufactured by International Sensor Technology Co. Overhead sensors that are selective to H_2, CH_4, CO gases are used to detect gas leaks. In the event of a leak detected above a user-selected threshold by any of the sensed gases, the detection system closes the solenoid valves for all gases.

Gases from the low-pressure manifold lines are supplied to respective individual Brooks model 5850S digital computer-controlled mass flow control (DMFC) valves. Figure 6 shows a schematic diagram of the steam and gas flow scheme used for the metal dusting experiments. The output from each mass flow controller combines into a central manifold tube that connects to the steam/vapor preheater assembly at the input cover flange for the retort tube. The steam/vapor preheater has a coaxial-design mixing chamber enabling the water vapor to be entrained by the flowing gas mixture prior to passing the preheat element. The gas mixture flow rate is typically 200-400 cm^3/min (STP), and the water flow rate is 1-5 cm^3/h. The preheat temperature is maintained with a Love Controls Model 16A three-mode process controller. Distilled water is supplied to the preheat mixing chamber by a Watson-Marlow Model MPL micro-metering pump that is fed from a 20 L poly carbonate carboy.

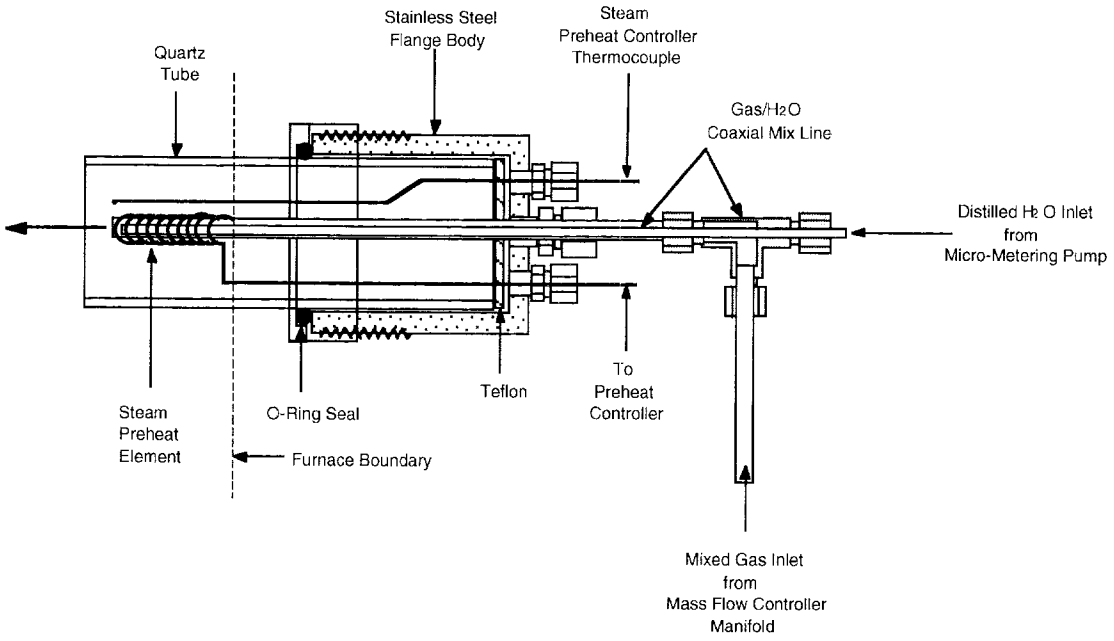

Fig. 6. Schematic diagram of steam and gas flow scheme used for metal dusting experiments.

The micro-metering pump is based on peristaltic action, and the flow rate is adjusted by varying the rotational speed of the roller cam and/or the diameter of the flexible tubing. The gas-steam mixture flows past the alloy test specimens to the exit port at the rear flange cap. After the gas-steam mixture exits the retort, it is passed through a chilled water pyrex condenser to collect water vapor for future measurement, while the remaining gas mixture is vented to a room exhaust vent handler. Gas composition analysis is available during an exposure test by a Stanford Research Systems Model QMS100 gas analyzer. Each environmental exposure test system has sampling ports at the inlet of the preheat mixing chamber and at the outlet of the chilled water condenser.

Alloy test specimens are mounted on a quartz specimen tree (see Fig. 7) that is centered in the heat zone of the retort chamber. Metal-dusting experiments are conducted under isothermal conditions at temperatures between 800 and 1300°F (427 and 704°C). A chromel-alumel thermocouple controls the furnace temperature. The test temperature and the precision of its control are important to the reproducibility and usefulness of the results. An indicating controller calibrated for the control thermocouple is maintains the furnace temperature. Specimen temperature is monitored with a second, sheathed chromel-alumel thermocouple inserted into the reaction chamber in the vicinity of the specimens. The outputs of the monitoring and control thermocouples are calibrated over the temperature range of interest, so that if the monitoring thermocouple becomes inoperative due to corrosion, the control

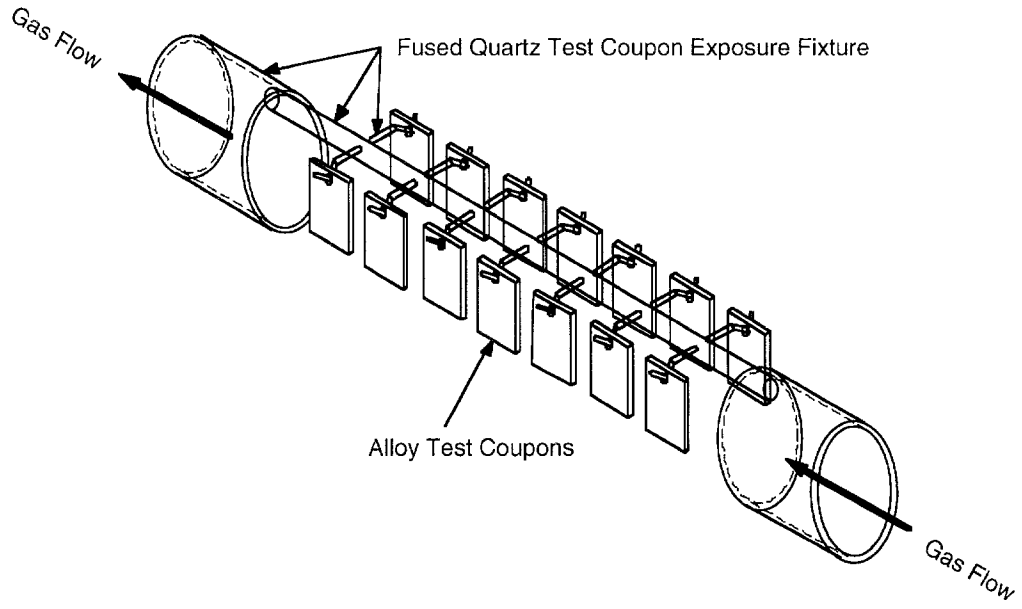

Fig. 7. Schematic diagram of quartz specimen holder and test coupon arrangement used for metal dusting experiments.

thermocouple can be used during continuation of the test. The multicomponent gas environment for the metal dusting program consists of CO, CO_2, H_2, CH_4, and H_2O. The actual composition of the gas mixture has a wide enough range to establish carbon activity of ≈0.5 to ≈100 at the temperatures and pressures of interest. The exposure time periods in different experiments ranged between 5 and 1000 h, depending on the objective of the test.

Materials

The test program includes a number of Fe- and Ni-base alloys, predominantly those commercially available, selected on the basis of Steering Committee discussions. Heat analysis of all the alloys, supplied by the alloy supplier, is maintained at Argonne National Laboratory. In addition, several surface-engineered alloy specimens (including surface coatings) are being evaluated in the program. Only wrought alloys are currently planned for the test program. Table 3 lists the nominal chemical compositions of the alloys selected for evaluation in the program.

The Fe-base alloys included a low-Cr ferritic steel (T22), an intermediate-Cr ferritic steel (T91), and several high-Cr ferritic and austenitic steels and other alloys. The Cr content of the latter alloys ranged between 17.3 and 26.7 wt.%. The Ni content of the high-Cr alloys ranged between 9.3 and 36.6 wt.%, except for alloys MA 956 and APMT, which contained no nickel. Several of the Fe-base alloys contained a third element such as Al

Table 3. Nominal chemical compositions (in wt.%) of alloys selected for the experimental program

Material	C	Cr	Ni	Mn	Si	Mo	Al	Fe	Other
T22	0.20	2.3	-	0.6	0.5	1.0	-	Bal	-
T91	0.08	8.6	0.1	0.5	0.4	1.0	-	Bal	N 0.05, Nb 0.07, V
153MA	0.05	18.4	9.5	0.6	1.4	0.2	-	Bal	N 0.15, Ce 0.04
253MA	0.09	20.9	10.9	0.6	1.6	0.3	-	Bal	N 0.19, Ce 0.04
353MA	0.05	24.4	34.7	1.4	1.3	0.1	-	Bal	N 0.18, V 0.06
321L	0.02	17.4	9.3	1.8	0.5	-	-	Bal	N 0.02, Ti 0.3
310	0.03	25.5	19.5	1.7	0.7	-	-	Bal	-
800	0.08	20.1	31.7	1.0	0.2	0.3	0.4	Bal	Ti 0.31
803	0.08	25.6	36.6	0.9	0.7	0.2	0.5	34.6	Ti 0.6
38815	0.01	13.9	15.3	0.6	5.8	1.0	0.13	Bal	-
MA956	-	20.0	-	-	-	-	4.5	Bal	Ti 0.5, Y_2O_3 0.6
321	0.04	17.3	10.3	1.2	0.4	-	-	Bal	Ti 0.4, N 0.01
APMT	0.04	21.7	-	0.1	0.6	2.8	4.9	Bal	-
4C54	0.17	26.7	0.3	0.7	0.5	-	-	Bal	N 0.19
600	0.04	15.4	Bal	0.2	0.1	-	-	9.7	-
601	0.03	21.9	61.8	0.2	0.2	0.1	1.4	14.5	Ti 0.3, Nb 0.1
690	0.01	27.2	61.4	0.2	0.1	0.1	0.2	10.2	Ti 0.3
617	0.08	21.6	53.6	0.1	0.1	9.5	1.2	0.9	Co 12.5, Ti 0.3
625	0.05	21.5	Bal	0.3	0.3	9.0	0.2	2.5	Nb 3.7, Ti 0.2
602CA	0.19	25.1	62.6	0.1	0.1	-	2.3	9.3	Ti 0.13, Zr 0.19, Y 0.09
214	0.04	15.9	Bal	0.2	0.1	0.5	3.7	2.5	Zr 0.01, Y 0.006
230	0.11	21.7	60.4	0.5	0.4	1.4	0.3	1.2	W 14, La 0.015
45TM	0.08	27.4	46.4	0.4	2.7	-	-	26.7	RE 0.07
HR 160	0.05	28.0	Bal	0.5	2.8	0.1	0.2	4.0	Co 30.0

or Si, which has a high affinity for O. For example, MA956 and APMT contained 4.5 and 4.9 wt.% Al, respectively. Alloys 153MA, 253MA, and 353MA contained Si in a range of 1.3-1.6 wt.%, whereas Alloy 38815 contained 5.8 wt.% Si.

Generally, the Ni-base alloys had a much more complex chemical composition since they contained Cr (in a range of 15.4-28 wt.%) and several other elements, such as Mo (alloys 617 and 625), Al (601, 617, 602CA, and 214), and Si (45TM and HR 160). Further, several alloys contained Nb, W, and Co, which can also influence the oxidation behavior of the alloys and their resistance to metal dusting attack.

Surface engineering of select alloys was conducted to examine the influence of that treatment on their resistance to metal dusting. The pretreatment involved oxidation of the alloys in an air or low-pO_2 environment at elevated temperatures. In addition, metallic coatings (primarily enrichment of Al or Cr in the surface regions of the alloys) were applied by a pack diffusion process on several Fe- and Ni-base alloys. Prior to evaluation under metal dusting conditions, the coatings were oxidized in air at elevated temperatures to develop adherent chromia or alumina scales.

Specimen Preparation

The samples are flat coupons with approximate dimensions of 12 x 20 x 1 to 2 mm. They are sheared slightly oversize, and their edges are milled to remove cut edges and reduce the coupons to final size. A standard surface finish is used for all alloy specimens. The finish involves a final wet grinding with 400-grit SiC paper. The surface-engineered specimens are used in the as-fabricated condition. In the tests to evaluate the effect of surface preparation on metal dusting, specimen surfaces are prepared by electropolishing, mill annealing, shot peening, etc. Stenciling or electric engraving at the corner of the coupons identified all of the specimens.

Prior to testing, specimens are thoroughly degreased in clean acetone, rinsed in water, and dried. The specimen dimensions are measured to ±0.02 mm, and the total exposed surface area, including edges, is calculated. The specimens are weighed to an accuracy of 0.1 mg.

The specimens are hung from a quartz specimen holder and oriented to expose the large surfaces parallel to the gas flow. The specimen holder is loaded into the reaction chamber at room temperature, and the chamber is closed. The specimens are heated to the desired test temperature in a hydrogen environment. Upon the system attaining the desired temperature, hydrogen gas flow is shut off, and the selected gas mixture is flowed past the specimens. After completion of the test, the furnace is shut off, the gas flow switched from the multicomponent gas to H_2 (at a flow rate of 10 cm^3/min), and the specimens are cooled to room temperature. The specimen holder is retrieved from the reaction chamber, and each specimen is stored separately in a plastic box.

Several analytical approaches and techniques are used to evaluate the tested specimens. These include metal weight gain/loss in as-exposed and cleaned conditions, pitting size and density (pits per unit area of surface), pit depth (average depth over significant number of pits), and substrate penetration as determined by metallographic examination. After the specimens are weighed in the as-exposed condition, deposits on the specimens are mechanically removed with a soft brush, and the deposit material is analyzed for metal content, if warranted. The brushed specimens are cleaned ultrasonically to remove residual deposits and then washed in water and dried. Subsequently, the specimens are weighed, and the weight gain/loss is noted.

The cleaned specimens are examined for surface pits by optical microscopy. This allows determination of the number of pits present in different regions of the specimen and the pit density. In addition, the sizes of several pits are measured and averaged to establish an average pit size.

At the end of a given run, several of the cleaned specimens (after weighing and pit measurement) are cut and mounted on the cut faces for metallographic polishing and

examination in the as-polished condition (with chemical etching, if needed) by optical and/or scanning electron microscopy. Pit depth and substrate penetration thickness are measured in several exposed specimens. The remaining good metal is calculated as the difference between the original thickness and the thickness unaffected by substrate penetration after exposure.

TEST RESULTS AND DISCUSSION

Key Variables for Carbon Deposition and Metal Dusting

Ten short-term runs were conducted in the two existing test facilities to evaluate the role of several variables in the carbon deposition process and in the initiation of metal dusting reactions. Table 4 lists the ten runs conducted along with specifics on the experimental conditions and objectives. The first nine runs were conducted to evaluate the effect of key variables such as exposure time, temperature, water content in the exposure gas, and presence/absence of catatytic material during exposure on the metal dusting initiation. The range of parameters in the scoping tests included exposure times of 5-100 h, temperatures of 593°C (1100°F) and 704°C (1300°F), gas mixtures with and without H_2O, and presence/absence of catalyzing agent. The specimens included pure Fe, pure Ni, Type 304 stainless steel (ss), Alloys 800 and 601, and Fe aluminide intermetallic. Runs 2 and 3 were conducted for 100 h at 593°C (1100°F) in Gas 4 and 5, respectively. Gases 4 and 5 had similar composition (see Table 1 for gas compositions), except that Gas 5 had 2 vol.% H_2O in addition to other gases.

The carbon activity values established by the Gases 4 and 5 are listed in Table 2. Since Gas 4 contained no H_2O, the carbon activities of this gas mixture at 593°C (1100°F) are infinity and 4.98, based on Reactions 1 and 2, respectively. The carbon activity values for Gas 5 at 1100°F are 32.3 and 5.04, based on Reactions 1 and 2, respectively.

Figure 8 shows macrophotographs of specimens that were exposed in Runs 2 and 3 for 100 h at 593°C (1100°F) in Gas Mixtures 4 and 5. Copious amounts of carbon was deposited on the specimens and on the alumina sample holder. This finding indicates that the gas composition selected for the initial experiments is susceptible to carbon deposition, and addition of 2 vol.% H_2O has very little effect on carbon deposition. In Runs 4 and 5, the specimens were exposed for 100 h in the same gas mixtures but at 704°C (1300°F) instead of 593°C (1100°F). The carbon activities established by Gases 4 and 5 at 704°C (1300°F) are infinity and 3.80 based on Reaction 1, whereas the values are 0.34 based on Reaction 2. The calculations indicate that, if Reaction 1 determined carbon deposition, carbon deposit is expected because $a_C > 1$; on the other hand, if Reaction 2 determined the deposition, no deposit of carbon is anticipated

Table 4. Experimental conditions for laboratory runs

Run Number	Experimental conditions	Gas mixture	Objective
1	593°C (1100°F), 48 h	Gas 6	Program start
2	593°C (1100°F), 100 h	Gas 4	No water
3	593°C (1100°F), 100 h	Gas 5	2 vol.% H_2O
4	704°C (1300°F), 100 h	Gas 4	Effect of temperature, H_2O
5	704°C (1300°F), 100 h	Gas 5	"
6	593°C (1100°F), 5 h	Gas 5	Effect of time, H_2O
7	593°C (1100°F), 5 h	Gas 4	"
8	593°C (1100°F), 72 h	Gas 4	Ceramics only (no catalysis)
9	593°C (1100°F), 72 h	Gas 5	"
10	593°C (1100°F), 90 h	Gas 4	New system validation
11	593°C (1100°F), 115 h	Gas 4	Fe specimen only
12	593°C (1100°F), 115 h	Gas 4+H_2O	Fe specimen only
13	593°C (1100°F), 100 h	Gas 4+H_2O	Ni specimen only
14	593°C (1100°F), 100 h	Gas 4	Ni specimen only
15	593°C (1100°F), 1000 h	Gas 2	Fe-base alloys
16	593°C (1100°F), 1000 h	Gas 2	Ni-base alloys
17	482°C (900°F), 100 h	Gas 2	Fe specimen only
18	482°C (900°F), 100 h	Gas 2	Ni specimen only
19	593°C (1100°F), 1000 h	Gas 2, low H_2O	Fe-base alloys
20	482°C (900°F), 1000 h	Gas 2	Fe-base alloys
21	482°C (900°F), 1000 h	Gas 2	Ni-base alloys
22	704°C (1300°F), 98 h	High CO Gas	Fe, T91, 304
23	704°C (1300°F), 98 h	"	Ni, Ni-base alloys
24	704°C (1300°F), 102 h	No water	Ni, Ni-base alloys
25*	593°C (1100°F), 1000 h	Gas 2	Fe-base alloys, preox. at 750°C in air
26*	593°C (1100°F), 1000 h	Gas 2	Ni-base alloys, preox. at 750°C in air
27	593°C (1100°F), 142 h	Gas 2	Pack diffusion coatings/Fe-base alloys

*In progress.

because a_C <1. Figure 9 shows the macrophotographs of specimens that were exposed in Runs 4 and 5 for 100 h at 704°C (1300°F) in Gas Mixtures 4 and 5. The occurrence of a significant carbon deposit in these runs indicates that Reaction 1 determines the carbon activity in the exposure environment.

Run 2 Run 3

$CO\text{-}CO_2\text{-}H_2$ $CO\text{-}CO_2\text{-}H_2\text{-}H_2O$

100 h at 1100°F

Fig. 8 Macrophotograph of specimens after 100-h exposure in Runs 2 and 3 conducted at 593°C (1100°F)

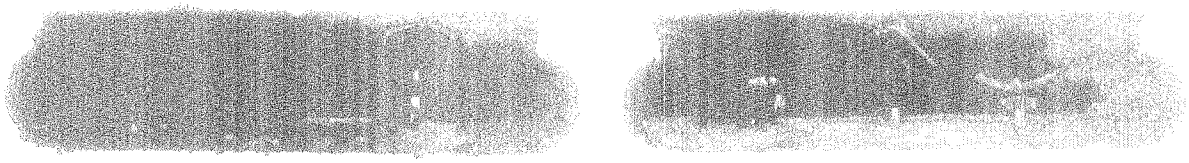

Run 4 Run 5

$CO\text{-}CO_2\text{-}H_2$ $CO\text{-}CO_2\text{-}H_2\text{-}H_2O$

Fig. 9 Macrophotograph of specimens after 100-h exposure in Runs 4 and 5 conducted at 704°C (1300°F).

Runs 6 and 7 were conducted to examine the effect of exposure time on initiation of carbon deposition. Runs were conducted for 5 h at 593°C (1100°F) in Gas Mixtures 4 and 5. Figure 10 shows the macrophotographs of specimens after the 5-h exposure. It is evident that the gas phase reactions, accentuated by the catalytic effect of the

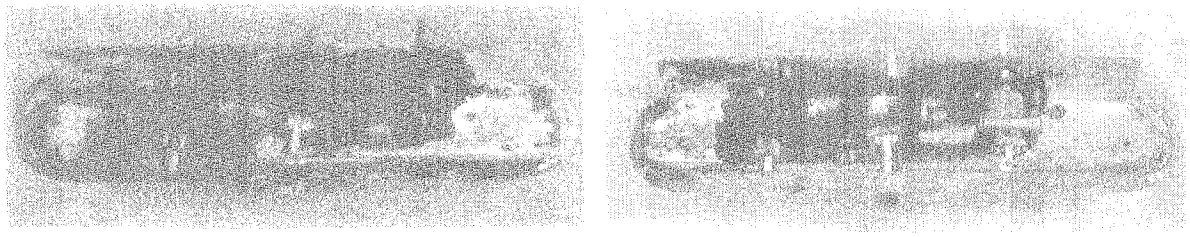

Run 7 Run 6

CO-CO_2-H_2 CO-CO_2-H_2-H_2O

Fig. 16. Macrophotograph of specimens after 5-h exposure in Runs 6 and 7 conducted at 593°C (1100°F).

metallic specimens consisting of Fe- and Ni-base alloys, lead to $a_c >> 1$, i.e., copious amounts of carbon deposit even after only 5 h. The results from exposures in Runs 1 through 7 also indicated that pure Fe and Fe-base alloys were more susceptible to carbon deposition and metal dusting than pure Ni and Ni-base alloys. Further, the exposure of Fe- and Ni-base alloys in the same experiment led to deposit of carbon not only on Fe-base alloys but also on Ni-base alloys, indicating a cross contamination of Ni-base alloys. Therefore, additional experiments were performed in which the Fe- and Ni-base alloys were exposed separately to avoid cross contamination and to assess their inherent behavior in the metal dusting environment.

To examine the role of catalytic effect on gas phase reactions, Runs 8 and 9 were conducted in the same gas environment with high purity alumina specimens and without any metallic specimens. After 25 h exposure at 593°C (1100°F) in Gas 4 and 5, virtually no carbon was detected on the alumina specimens (see Fig. 14). These results indicate that a viable catalytic material is essential to establishing high carbon activity and associated deposition of carbon. This experiment also indicates that coatings, such as alumina, may offer protection against carbon deposition and subsequent metal dusting of coated metallic structural materials.

Run 10 was conducted for 90 h in one of these new systems under the same conditions as in Run 2 to validate the adequacy of the new equipment and reproducibility of the results.

Characteristics of Carbon Deposits

Scanning electron microscopy (SEM), Raman spectroscopy, and X-ray diffraction (XRD) analyses have been used to study the microstructure, electron binding, and phase chemistry of the metal dusting products. Thus far, the investigations have focused on deposits on the metals. Deposits on the carbon dust have hardly been studied, even though carbon is an integral part of the metal dusting process. Graphite has a layered

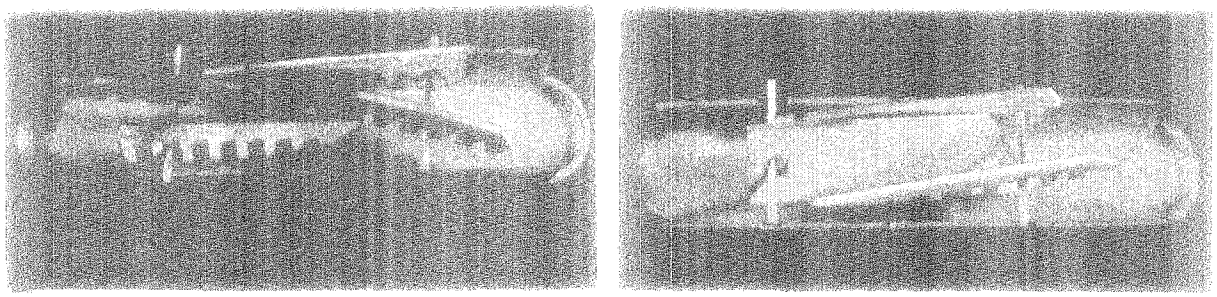

Run 8 Run 9

CO-CO_2-H_2 CO-CO_2-H_2-H_2O

Fig. 11. Macrophotograph of specimens after 72-h exposure in Runs 8 and 9 conducted at 593°C (1100°F).

structure with the space group $P6_3/mmc$ (see Fig. 12). Carbon atoms within the layers bond strongly through sp^2 hybridization and arrange in a two-dimensional honeycomb network. The layers are stacked in a hexagonal crystal structure and are bound together by van der Waals force. Because the van der Waals force is weak, the C-C distance between layers is large (335.4 pm).[11] For this reason, graphite crystals readily disorder along the c-axis.[12]

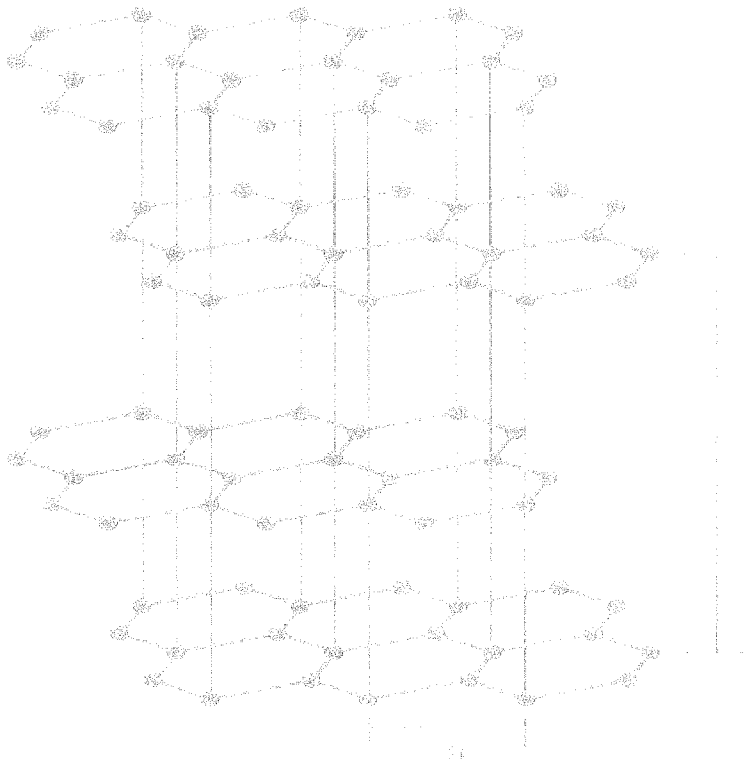

Fig. 12. Structure of graphite. Carbon atoms within layers arrange in two-dimensional honeycomb network; layers are stacked in a hexagonal crystal structure.

The Raman scattering from various forms of carbon is sensitive to the structural disorder of the material.[13-16] As a result, Raman spectroscopy provides a useful nondestructive technique for structural characterization of carbon materials. Lattice defects in graphite break down the hexagonal symmetry of the graphite lattice and modify the optical selection rules for the lattice vibrational modes that are observable in Raman scattering. A single Raman line, the E_{2g2} vibration mode, is theoretically expected for the hexagonal lattice of graphite and has been observed at 1575 cm^{-1} in natural graphite. In glassy carbon, the layers are parallel, but their mutual orientation is random in the direction of the planes (due to the weak link between the layers). A band at 1355 cm^{-1} observed for glassy carbon has been assigned to a defect-activated vibrational mode originating from the distorted hexagonal lattice of graphite near the crystal boundary. The two bands at 1355 and 1575 cm^{-1} are designated as D (distorted) and G (graphite), respectively. The relative intensity ratio I_D/I_G and the relative bandwidths increase in progression from single-crystal graphite through polycrystalline graphite up to glassy carbon; hence, these values can be used as a measure of imperfection of the graphite layer planes.[13-16] These parameters are more defect sensitive than are the XRD parameters that define crystalline size. Therefore, Raman spectroscopy represents a useful tool for investigating the defects in carbon structures and their relationship to the metal dusting phenomenon.

Raman spectroscopy measurements were made for carbon deposited on pure Fe specimens during exposure in different experiments. The Spectra were obtained with a Renishaw System 2000 imaging Raman microscope equipped with a He-Ne laser that delivered ≈5 mW to the specimen. The spectra were recorded at wavelengths between 190 and 4000 cm^{-1}, with the laser partially defocused to a diameter of ≈5 μm to avoid burning or otherwise transforming the carbon deposits. Spectra were taken at three to six locations on a given specimen to verify that the observed surface deposits were uniform in composition. Magnetization of samples was measured by a vibrational-sample magnetometer under 1 Tesla in an argon atmosphere.

Figure 13 shows the Raman spectra (frequency range 190-1000 cm^{-1}, 1000-2000 cm^{-1}, and 2000-4000 cm^{-1}) of carbon "soot" from Runs 4, 5, and 7 along with Raman spectra of polycrystalline graphite and pencil "lead." It is evident that the two bands at 1355 and 1575 cm^{-1} are similar, but the carbon from the metal dusting runs exhibits broader peaks than the graphite block and pencil lead. Figure 14 shows the XRD pattern for the coke and carbon layer on the iron sample.

The major phases in the metal dusting product are graphite and Fe_3C. There may be a small amount of Fe_3O_4, which presents a weak diffraction peak at $2\theta = 35.4°$. According to the mechanism proposed by Hochman,[4] Fe_3C decomposes to Fe and C at

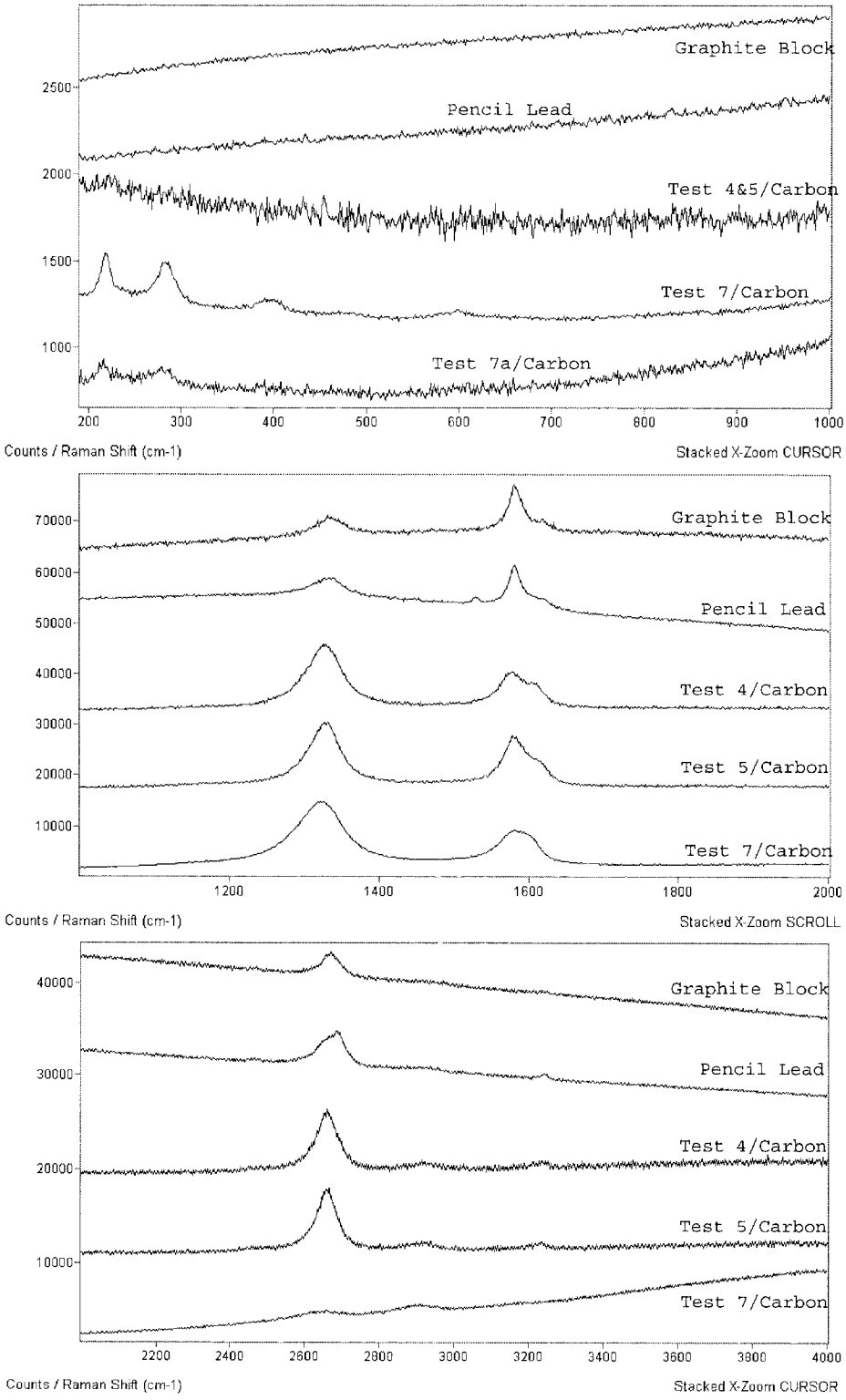

Fig. 13. Raman spectra (frequency range 190-1000 cm^{-1}, 1000-2000 cm^{-1}, and 2000-4000 cm^{-1}) of carbon "soot" from Runs 4, 5, and 7 along with Raman spectra of polycrystalline graphite and pencil "lead." Tests 4 and 5 were run for 100 h at 1300°F and Test 7 was run for 5 h at 593°C (1100°F).

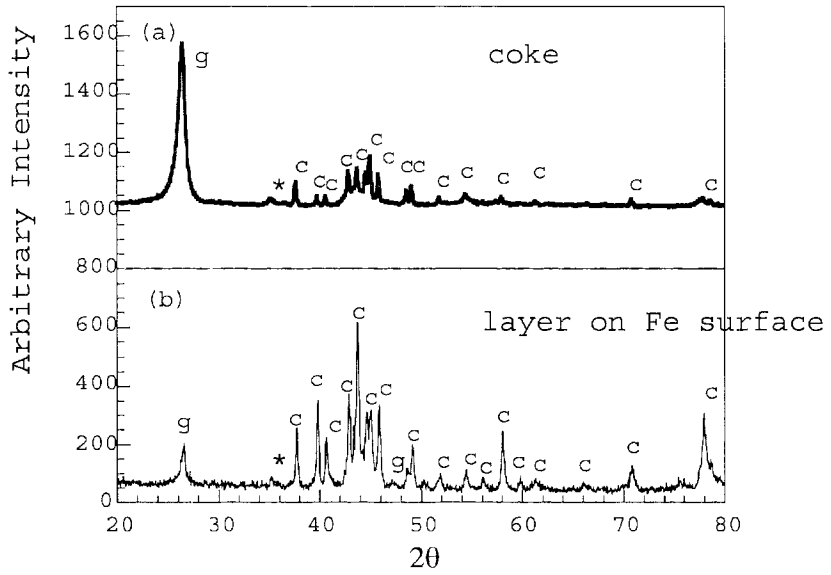

Fig. 14. XRD pattern of coke and surface layer on iron sample after exposure to Gas 4 at 593°C (1100°F) for 100 h. Major phases are graphite (g) and cementite (c); there may be a small amount of Fe_3O_4, whose strongest peak is indicated by *.

the final step, in which case the final products should be Fe and C. However, no iron diffraction peak appears in the metal dusting product. XRD may not be able to detect the phase if the concentration is <5%. Therefore, a magnetic measurement method was used to determine if iron was present. Iron is a strong ferromagnetic material with Curie temperature (Tc) at 770°C.[17] A huge magnetization increase would be observed at 770°C, if there was evidence of iron in the metal dusting product. Figure 15 shows the magnetization of the metal dusting product as a function of temperature. The large transition of magnetization at 210°C is due to Fe_3C.[17] The small magnetization increase at 582°C may be due to small amount of ferromagnetic Fe_3O_4 with Tc at 585°C. However, there is no obvious transition of magnetization around 770°C. The very small magnetic moment around 700°C indicates that the concentration of regular α-iron in the product of metal dusting is below 0.1%. It is possible that XRD and magnetic measurement cannot detect some iron particles with very small size. However, both XRD and magnetic measurement show that the major phase in coke is Fe_3C, not Fe phase. Fe_3C is the final product of metal dusting instead of only the intermediate compound surmised by Hochman's mechanism.[4] Therefore, further investigation is needed to establish the causes of metal dusting and methods to mitigate it under our experimental conditions.

The XRD [002] peak widths of the carbon dust are broader than those of the well-crystallized graphite (Fig. 16). We interpret this observation as indicating that the crystallinity of carbon dust is poorer than that of graphite. However, the [002] peak

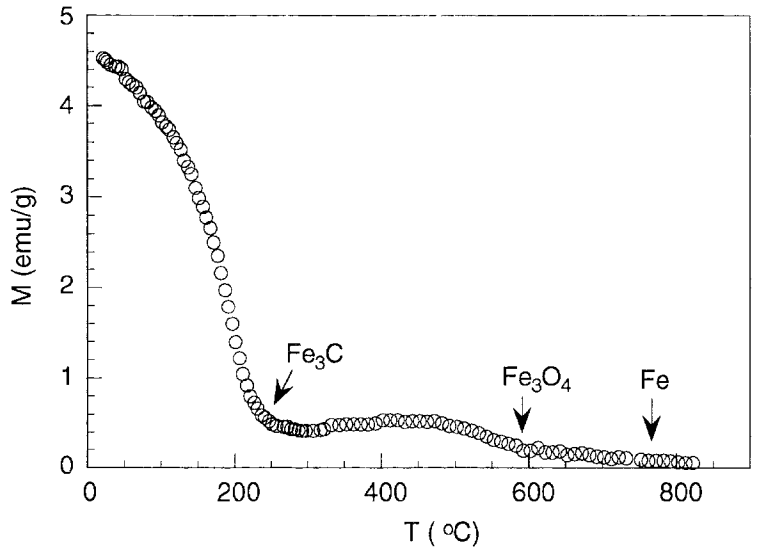

Fig. 15. Temperature dependence of magnetization (M) of metal dusting product obtained in Run 4 at 593°C (1100°F).

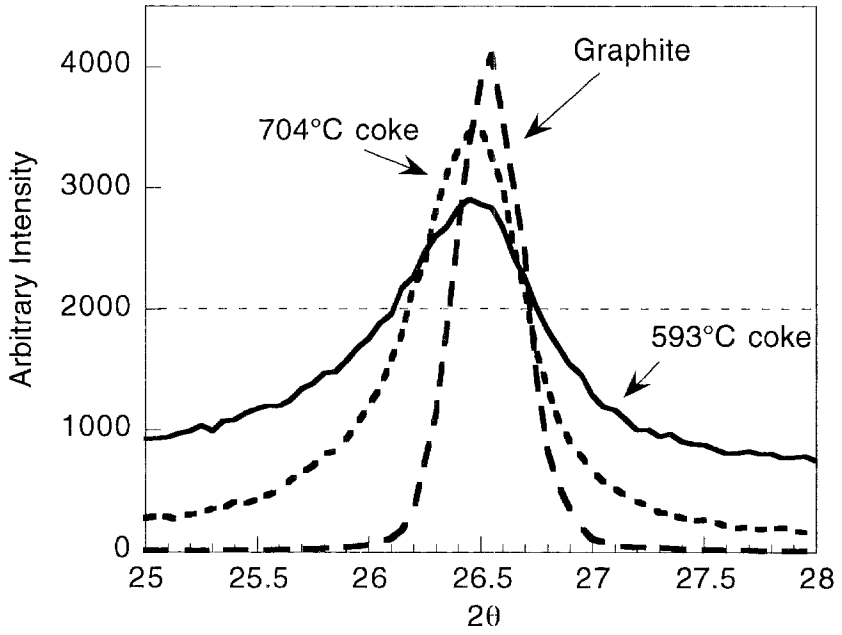

Fig. 16. Peak widths of [002] diffraction from graphite and coke (at 593 and 704°C). Narrower peak width indicates better crystallinity.

widths of the coke are much narrower than that of glassy carbon (see Fig. 17). Table 5 shows that the coke crystallite sizes are much larger than those of glassy carbon. The coke crystallite sizes are also considerably larger than those reported for other carbonaceous materials made at a similar temperature.[18-20] The interlayer distances of the carbon plane are related to the degree of disorder. The layers are not parallel in the disoriented graphite structure. Average interlayer plane distance increases when the layers are disoriented. The interlayer plane distance is 3.354 Å for single-crystal

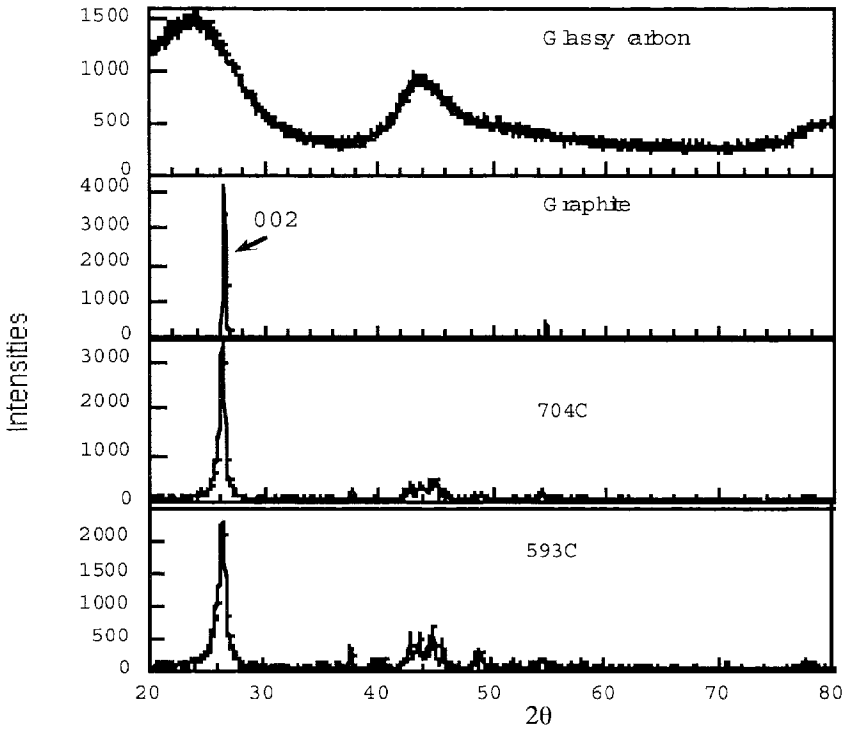

Fig. 17. Peak widths of [002] diffraction from glassy carbon, graphite, and coke (593 and 704°C). Narrower peak width indicates better crystallinity.

Table 5. Crystallite dimension and interlayer plane distance of graphite, coke (593 and 704°C), and glassy carbon. Δ is difference of interlayer plane distance of carbon from single-crystal graphite (with interlayer plane distance 3.354 Å).

	Interlayer plane distance (Å)	Δ (Å)	Crystallite size (Å)		Mean number of layers per particle
			c-axis	a-axis	
Graphite	3.356	0.002	220	299	65.7
Coke developed at 704°C	3.362	0.006	145	151	43.3
Coke developed at 593°C	3.365	0.011	110	127	32.8
Glassy carbon	3.736	0.382	12	15	3.4

graphite.[11] The interlayer plane distance of coke is very close to that of the well-crystallized graphite. Franklin[11] proposed the following relationship for the proportion of disoriented layer (p) as a function of interlayer plane distance (d):

$$d = 3.44 - 0.086(1 - p^2).$$

According to this relationship, the interlayer plane distances of coke made at 704°C, 3.362 Å (Table 5), indicates carbon having ≈70% three-dimensional ordering. For the carbons produced by conventional treatment of carbon-containing raw materials, >2000°C is required for thermal recrystallization to occur and to obtain this high degree of three-dimensional ordering.[18,19]

Raman spectra of coke, glassy carbon, and graphite are presented in Fig. 18. The well-crystallized graphite shows two peaks: the sharp band at 1580 cm^{-1} (G band) can be assigned to the E_{2g} C-C stretching mode.[21-23] The other peak, at 2685 cm^{-1}, is a two-phonon band taken to be 2 x 1330 cm^{-1}. The first-order phonon band at 1330 cm^{-1} (D band) is not observed for well-crystallized graphite because of the k = 0 selection rule.[21] However, disorder in the lattice can cause a breakdown of this selection rule, which is why the 1330 cm^{-1} band is observed in the Raman spectra of glassy carbon. Symmetry

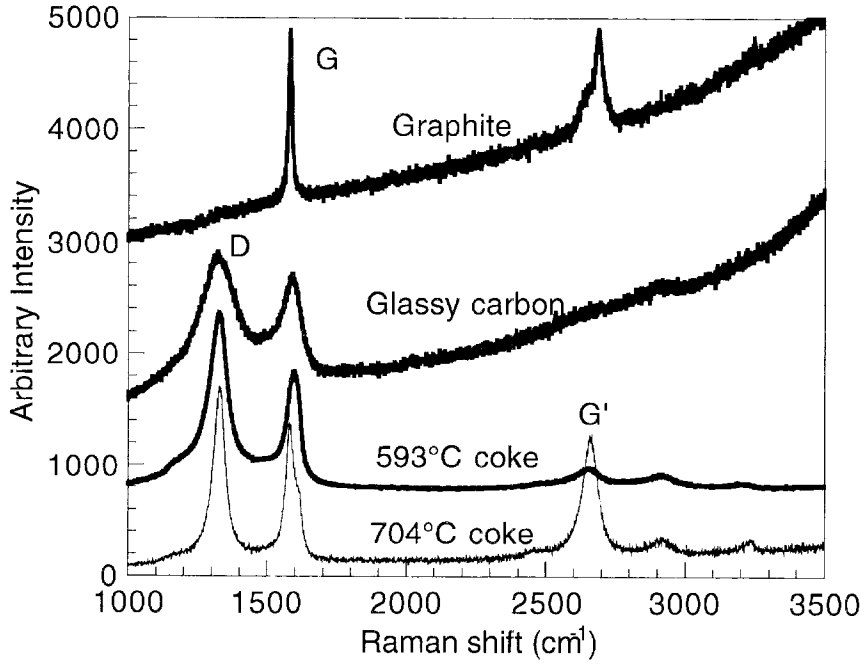

Fig. 18. Raman spectra of graphite, glassy carbon, and coke made at 593°C and 704°C. The 1330 cm^{-1} band is designated as D because its character is related to disorder of the graphite phase, whereas the 1580 and 2680 cm^{-1} bands are assigned to G and G', respectively.

may also be affected by a high degree of disorder that could, for example, cause the second-order phonon at 2685 cm^{-1} to disappear in the Raman spectra of glassy carbon. The 2685 cm^{-1} band is designated as G' because its character is similar to that of the G band. The highly disordered carbons have very broad Raman bands, and the intensity of the 1330 cm^{-1} band increases when carbon becomes more disordered. The intensities of the D band are considered to depend on the in-plane displacements, which lead to a loss of hexagonal symmetry in the two-dimensional lattice within the graphite planes.[22] A shoulder at 1617 cm^{-1} in the cokes formed at 704°C is also

dependent on structural disorder and is, therefore, designated as the D' band (Fig. 19). Its behavior is qualitatively similar to that of the D band.[24,25] The 2920 cm^{-1} peak for the 704°C coke arises from a combination of the strong density of states at ~1330 and 1617 cm^{-1}.[26] The 3235 cm^{-1} band is the first overtone of the G band.[22]

The widths of the Raman bands for the coke from the dusting process are between those of well-crystallized graphite and glassy carbon. The D/G intensity ratio of coke made at 704°C is lower than that of coke made at 593°C, and the D band for coke made at 704°C is obviously narrower (see Fig. 19). The G band at 1583 cm^{-1} and the D' band at 1617 cm^{-1} separate in the coke made at 704°C, whereas the G and D' bands of the coke made at 593°C remain merged in one broad band. The bandwidths and the D/G intensity ratio are related to the crystallinity of the carbon dust.[13-16] Therefore, the coke made at 704°C is better crystallized than the coke made at 593°C. The intensity of the G' band at 2685 cm^{-1} is reported to be highly sensitive to the structure.[27] For the coke made at 704°C, the G' band is much stronger than for coke made at 593°C, and the G' bandwidth (71 cm^{-1} at half height) of the coke made at 704°C is narrower than the G' bandwidth (112 cm^{-1} at half height) of coke made at 593°C. This finding also indicates that the coke made at 704°C is better crystallized than that made at 593°C.

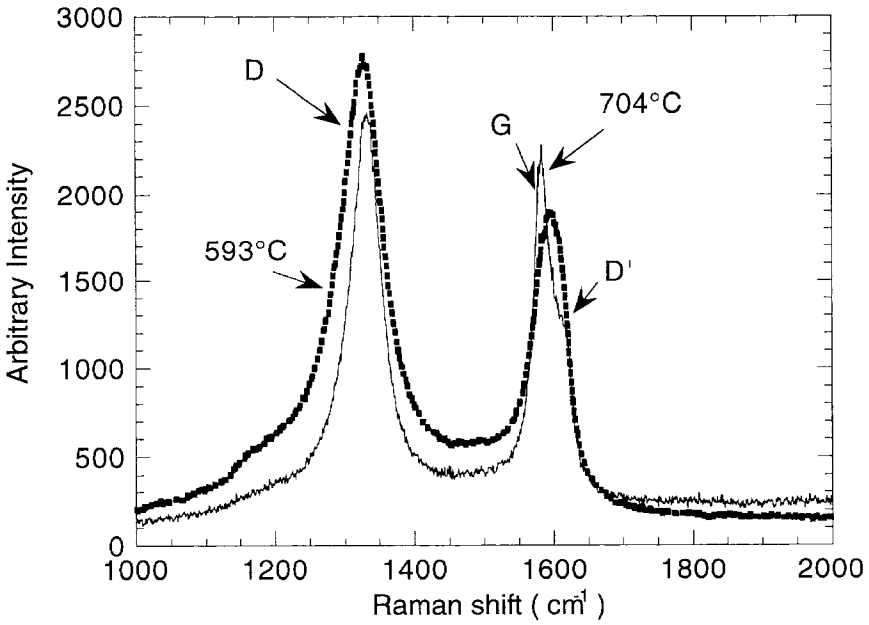

Fig. 19. Raman spectra of coke made at 593°C and 704°C. Raman bandwidth for coke made at 704°C is narrower than that for coke made at 593°C. D/G intensity ratio for coke made at 593°C is 1.5, whereas that for coke made at 704°C is only 1.1.

As mentioned earlier, a layer of carbon closely adheres to the surface of the tested alloys. The Raman spectra in Fig. 20 show that the Raman band for the carbon on the surface of the iron has a narrower width than that for coke at some distance from the surface. This finding may indicate that carbon in the tightly adhering layer of the iron

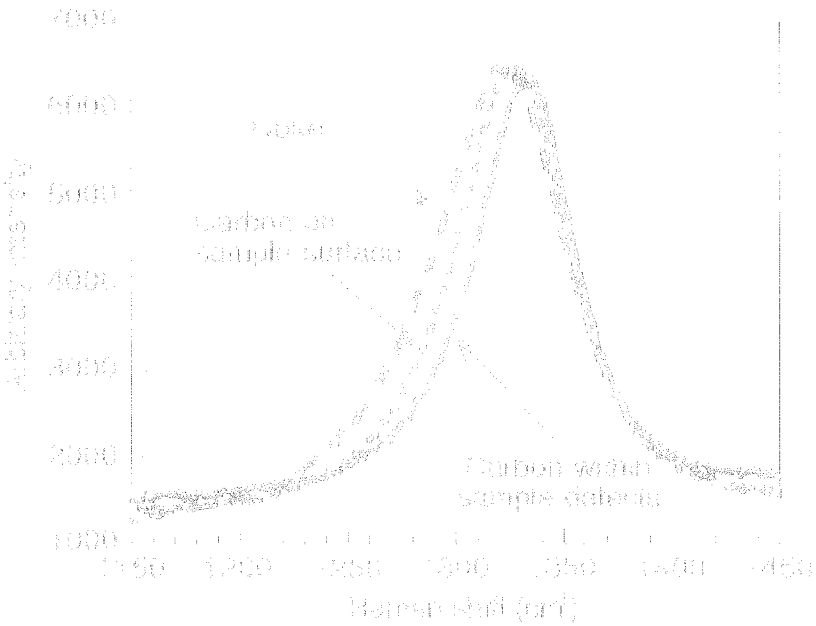

Fig. 20. Raman spectra of coke, carbon on alloy sample surface, and carbon in sample debris.

surface but better crystallinity. The SEM cross section of the Fe-Al alloy (Fig. 21) indicates the effect of porosity in the material on carbon deposition and metal dusting. Carbonaceous gases diffused and precipitated inside the alloy. EDX analysis revealed that the dark areas are filled with carbon. Raman spectra were obtained by scanning the laser on the carbon deposits in the Fe-Al coating layer.

Fig. 21. SEM cross section of Fe-Al alloy after metal cutting experiment at 900°F (1100°F). Carbon has diffused into and precipitated within the alloy. Energy-dispersive x-ray spectroscopy (EDX) indicated that the dark areas are filled with carbon.

Figure 20 shows that the line width of the Raman band for the carbon in the alloy defects is narrower than that for the coke and the surface carbon. The band position is shifted slightly to a higher frequency (10 cm^{-1}) for the carbon in iron. Therefore, the crystallinity of carbon increases progressively from coke through surface carbon to the carbon within the metal after metal dusting.

Proposed Metal Dusting Mechanism

The experimental results from Raman, XRD, and SEM measurements shed some light on the mechanism of metal dusting. There appears to be a relationship between metal dusting and degree of crystallization of the carbon dust. Our interpretation of the crystallizing process for carbon during dusting is shown in Fig. 22. In the initial stage, single carbon atoms are deposited on the surface of the iron; they then either dissolve in the iron or accumulate to form small carbon particles. There are dangling bonds on the surface and many defects, such as vacancies and distorted bonds in the small particles. All of these surface and internal defects increase the free energy of these particles compared to that of well-crystallized graphite. At higher temperature, where the carbon atoms have enough energy to migrate, the carbon recrystallizes from small-distorted particles to large well-crystallized graphite. However, because the C-C bond is very strong (the melting temperature of carbon is 4492°C), the recrystallization process requires a higher temperature. Achieving good crystallinity with carbon below 1000°C is problematic for the following reasons. First, the carbon layers in graphite structure are easily disoriented because the van der Waals forces between the layers are very weak. Second, recrystallization below 1000°C is hindered because the bond in the layers is too strong.

The catalysts such as iron or cementite could dramatically increase the rate of carbon recrystallization (right column in Fig. 22). The cementite structure has been described as a framework of almost close-packed iron atoms held together by metallic bonding to the small carbon atoms in the largest interstices. Carbon occupies only one-sixth of the interstices, allowing carbon to dissolve in and move though those interstices. When carbon dissolves in the iron or cementite, the Fe-C bond is much weaker than the C-C bond, and transportation of carbon atoms is greatly facilitated. Therefore, the poorly crystallized coke can transfer though iron and eventually achieve improved crystallinity. Reducing the number of dangling bonds on the surface and the number of internal defects in the carbon particles reduces the free energy.

Figure 23 shows the catalytic recrystallization process. Carbon atoms are deposited on the surface of Fe_3C. As mentioned above, the carbon layers in the graphite structure are easily disoriented because the van der Waals forces between the layers are weak. Carbon can not grow with good crystallinity if the lattice planes of Fe_3C do not match the graphite lattice planes to help the crystallization of carbon (upper part in Fig. 23). When

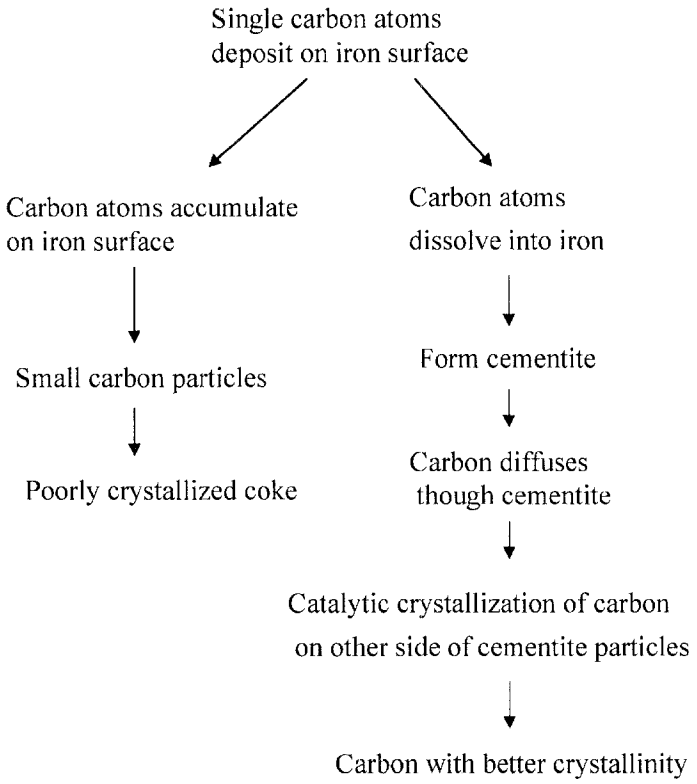

Fg. 22. Proposed process for carbon crystallization after deposition in metal-dusting environment.

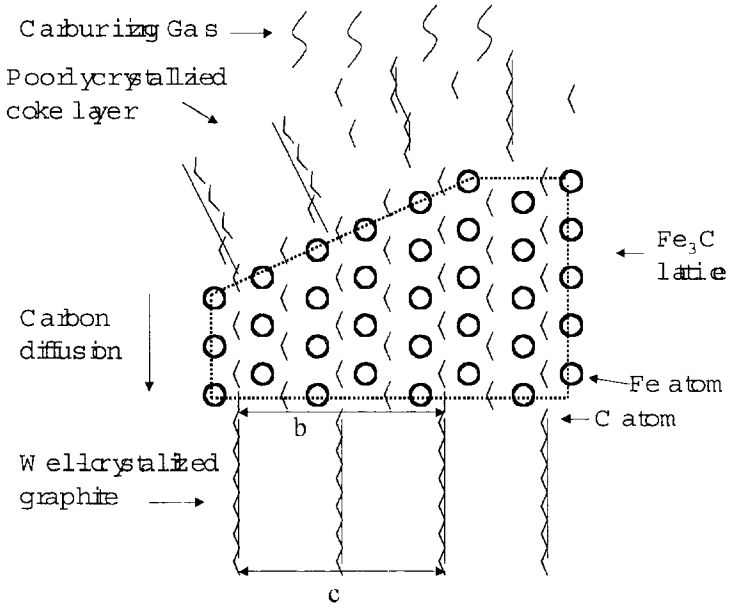

Fig. 23. Proposed process for catalytic crystallization. Poorly crystallized carbon dissolves in and diffuses though cementite, whose lattice provides excellent orientation for crystallization of graphite; b dimension of cementite (6.743 Å) is very close to c dimension of graphite (6.724 Å).

carbon atoms diffuse though the cementite and precipitate from a preferred lattice plane, the lattice of cementite provides an excellent orientation for the epitaxial growth of graphite. Graphite was reported to grow perpendicular to the lattice plane of Fe_3C with its layer plane.[28] Cementite has an orthorhombic lattice with cell parameters a = 5.091 Å, b = 6.743 Å, c = 4.526 Å. Its b-axis is almost the same as the c axis of graphite (6.724 Å). This is helpful for the crystallization of graphite. Catalytic crystallization in the metal dusting environment leads to coke with a much larger crystallite size and smaller interlayer planar distance than the carbons produced by other methods at similar temperature.[11,18-20]

The catalytic crystallization effect of iron was proven by Nakamizo et al.[29] and Kammereck et al.[30] They investigated the effect of iron on the crystallization of glassy carbon made from furfuryl alcohol. Only 3% addition of iron led to a dramatic decrease in the widths of the D and G bands and the D/G intensity ratio. The line widths of carbon with iron present annealed at 600°C were narrower than those of the carbon without iron annealed at 2000°C.[29] X-ray diffraction showed that addition of iron narrows the graphite [002] XRD peak dramatically.[29,30] These experiments showed that the crystallization rate of carbon is dramatically increased by the presence of iron or cementite catalyst.

Metal Dusting of Pure Metals

Pure Fe and Ni specimens were examined over a range of temperatures and gas chemistry conditions to evaluate their susceptibility to metal dusting reactions and also to establish a baseline for comparison with the performance of Fe-base and Ni-base alloys, which are of interest for application in reformer environments.

Much of the earlier discussion has already treated carbon deposition in experiments conducted on pure Fe specimens exposed under various conditions. In addition to the analysis of the carbon deposit obtained from different runs, we also completed weight change measurements and detailed microstructural evaluation by electron-optical techniques, X-ray diffraction, and Raman spectroscopy on the Fe specimens. Following each exposure period, specimen weight change was determined after removal of adhering coke in an ultrasonic bath with acetone. Figure 24 shows the weight change data for pure Fe specimens in Runs 1 through 7, the experimental details for which are listed in Table 4. The data show that Fe is very susceptible to metal dusting attack and exhibits significant loss of metal in all the runs. The presence of 2 vol.% H_2O in the gas mixture (e.g., Gas 5 vs. Gas 4) may cause some delay in initiating metal dusting, especially based on data from 5-h exposures in Runs 7 and 6. However, H_2O at the 2% level has almost no effect at 593°C (1100°F) over the longer time period of 100 h (Runs 2 and 3). The wastage seems to be less at the higher temperature of 704°C (1300°F) compared with 593°C (1100°F), irrespective of the H_2O content of the gas.

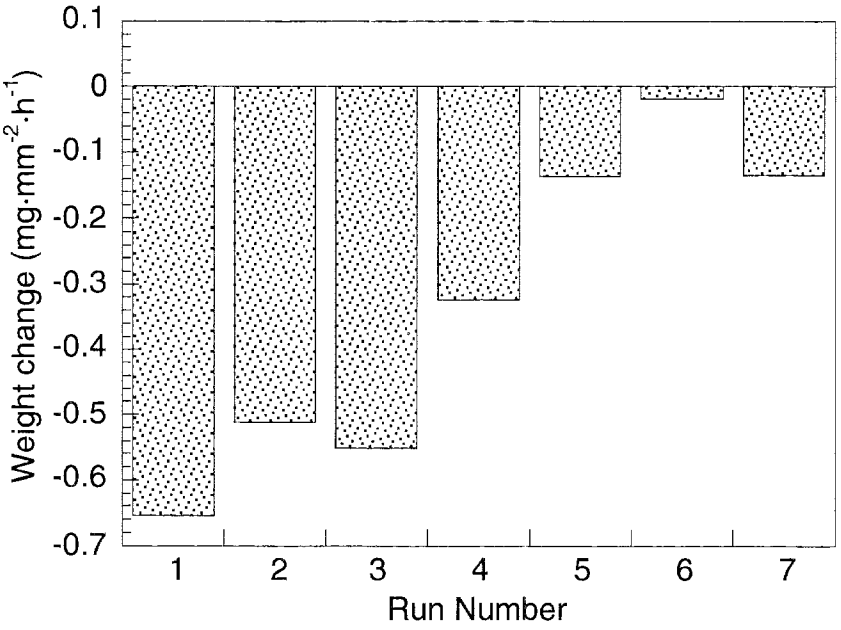

Fig. 24. Weight change data for pure Fe specimens exposed in Runs 1 through 7. Experimental details are listed in Tables 1, 2, and 4.

In our proposed catalytic crystallization process, carbon dissolves on the surface of the iron and crystallizes out in the bulk iron. Because the free energy of coke is probably higher than that of well-crystallized graphite, the saturating concentrations for coke and graphite will be different. High-free-energy coke should have a slightly higher saturating concentration than that of graphite (a_C=1); if so, the saturating concentration of coke will be oversaturating for graphite. Therefore, poorly crystalline coke could dissolve in iron or cementite and move away as well-crystallized graphite. In this process, carbon transfers from the cementite surface and grows inward via the defects or grain boundary of cementite or iron. The accumulation of carbon in alloy causes the metal particles to disintegrate, as seen in Fig. 25.

Figure 26 shows a schematic of a process in which cementite particles separate into small particles as carbon particles accumulate at the defects. Such a transport process will continue until the cementite particles become too small to provide a template for carbon growth to 10-nm-size crystals (Table 5). The metal finally becomes nanometer-size dust in this process. X-ray diffraction shows that the average size of the cementite particles in the coke is ≈27 nm.

The metal dusting process for iron can be described as follows:

1. Carbon deposits on the iron surface, supersaturating Fe.
2. Cementite forms at the Fe surface; the volume expansion creates defects.
3. Carbon diffuses through cementite and precipitates at defects of cementite.

Fig. 25. Post test SEM photomicrograph of metallographic cross section of iron. Tightly bound carbon layer found on iron surface after ultrasonic cleaning. Iron particles are separated into small particles and move away from the metal surface.

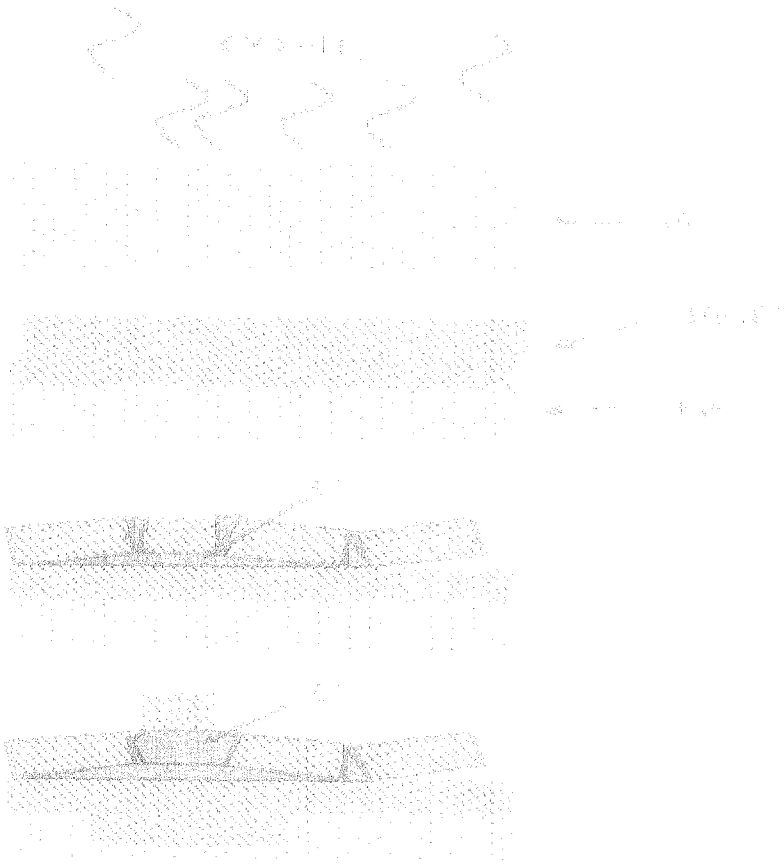

Fig. 26. Schematic of metal dusting process in the degradation of Fe.

4. Accumulation of carbon at the defects of cementite causes the cementite particles to separate into small particles and move away from metal.
5. Gas penetrates into the cracked area and continues further carbon deposition and the metal dusting process.

At high temperature, Fe may work directly as a catalyst in the crystallization of C since the iron lattice can also provide a good orientation for the growth of graphite. Carbon diffuses through Fe and precipitates at the defects. This precipitation also causes Fe particles to separate. Cementite forms when carbon diffuses into Fe. However, in the proposed mechanism, decomposition of Fe_3C is not a necessary condition to initiate metal dusting. Cementite acts as a medium for the diffusion and as a catalyst for crystallization of carbon. XRD shows that Fe_3C and carbon are the major phases in the products of metal dusting.

Pure Ni specimens were also exposed under different metal dusting environments in Runs 1 through 7. Figure 27 shows a comparison of Raman spectra (frequency range 1000-2000 cm^{-1} and 2000-4000 cm^{-1}) for carbon adhered onto Ni surfaces after exposure in Runs 3-7. Specimens exposed at 593°C (1100°F) exhibited greater amounts of sp3-type C-H bonds. Generally, the Ni surface was smooth before exposure, and polished surfaces can be seen in Fig. 28(a). The surface roughened after exposure, as can be seen in Fig. 28(b). A tightly adhering carbon layer was observed on the specimens, and neither ultrasonic cleaning nor acetone washing could remove the layer. To examine the specimen cross section, the carbon on the surface was separated from the carbon-containing mounting material by applying a silver paste to the sample surface before mounting. The thickness of the carbon layer was ≈40 μm, but it was not uniform. Metallographic cross section showed that Ni separated and moved into the carbon layer (see Fig. 29), and a chemical analysis of the carbon/Ni mixture showed ≈1% Ni in the mixture.

The major phases in the metal dusting product are graphite and Ni metal (Fig. 30). The XRD [002] peak width of this carbon is broader than that of the well-crystallized graphite (Fig. 31), indicating that the crystallinity of carbon is poorer than that of graphite. The XRD [002] peak width of coke is even broader than the carbon present on the surface of Ni. However, it is much narrower than that of carbon black, which is made by thermal decomposition of gasoline vapor at 704°C (see Fig. 32). The peak position of carbon black moves to a small diffraction angle, which can be attributed to the degree of disorder, as discussed in an earlier section of the report.

The catalytic effect of Ni in the carbon recrystallization was studied by the following experiment. A mixture of glassy carbon and 10% nickel(II) bis(2,2,6,6-tetramethyl-3,5-heptanedionato) [$Ni(C_{11}H_{19}O_2)_2$] was sealed in an evacuated quartz tube and slowly heated to 1000°C. The metalorganic precursor melted at 225°C and uniformly dispersed in the glassy carbon. At high temperature, the metalorganic compound

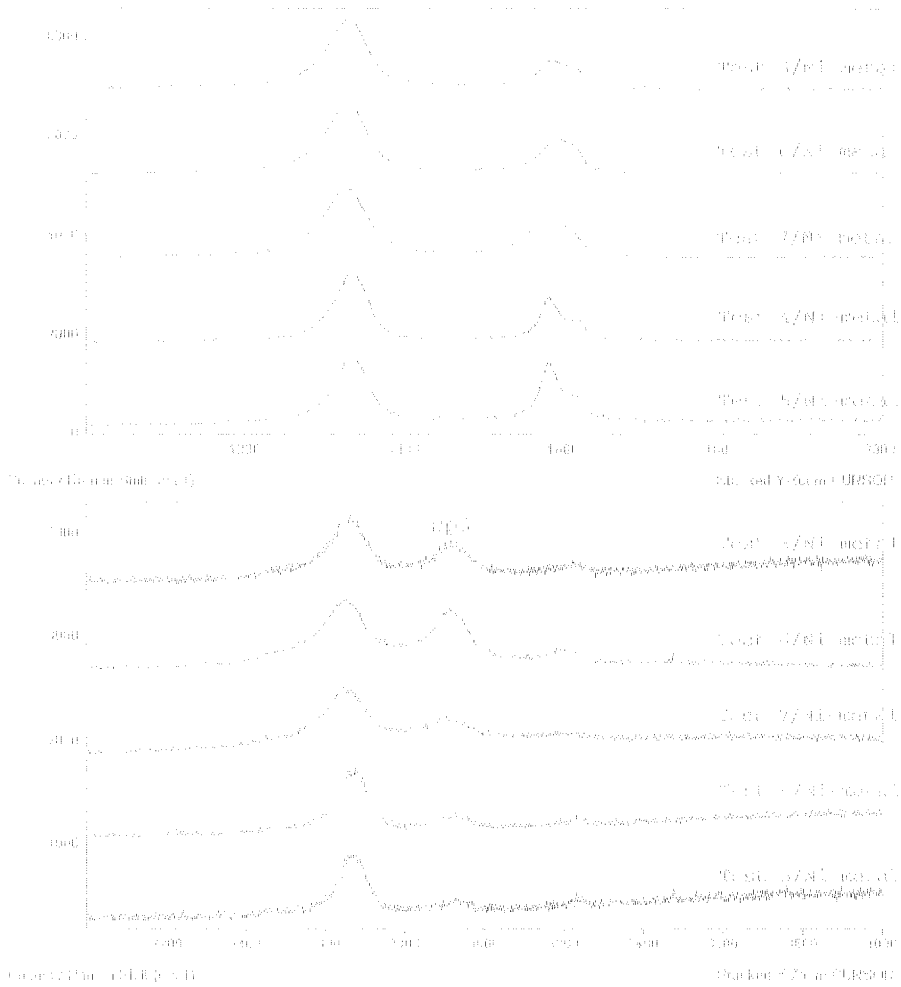

Fig. 22. Raman spectra for carbon adhered to Ni specimens from Runs 3-7. Runs 3, 6, and 7 were conducted at 593°C (1100°F) whereas Runs 4 and 5 were conducted at 704°C (1300°F).

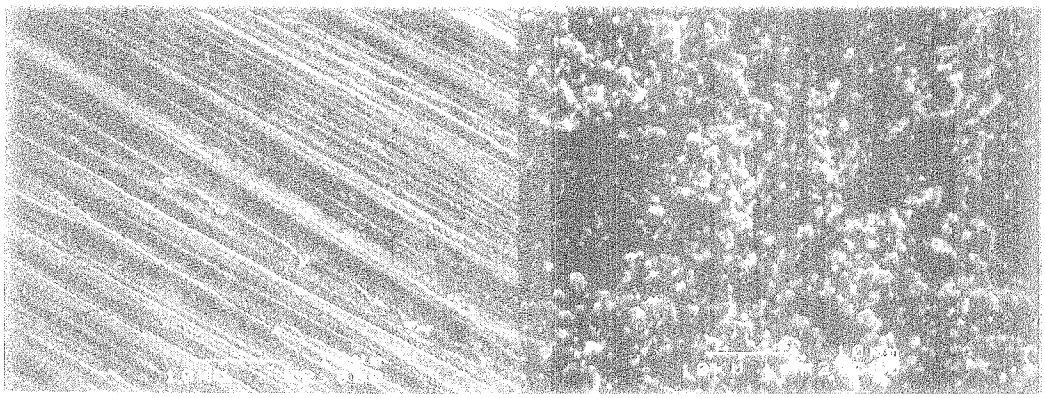

Fig. 23. SEM photomicrographs of Ni surfaces before and after exposure in a metal dusting experiment.

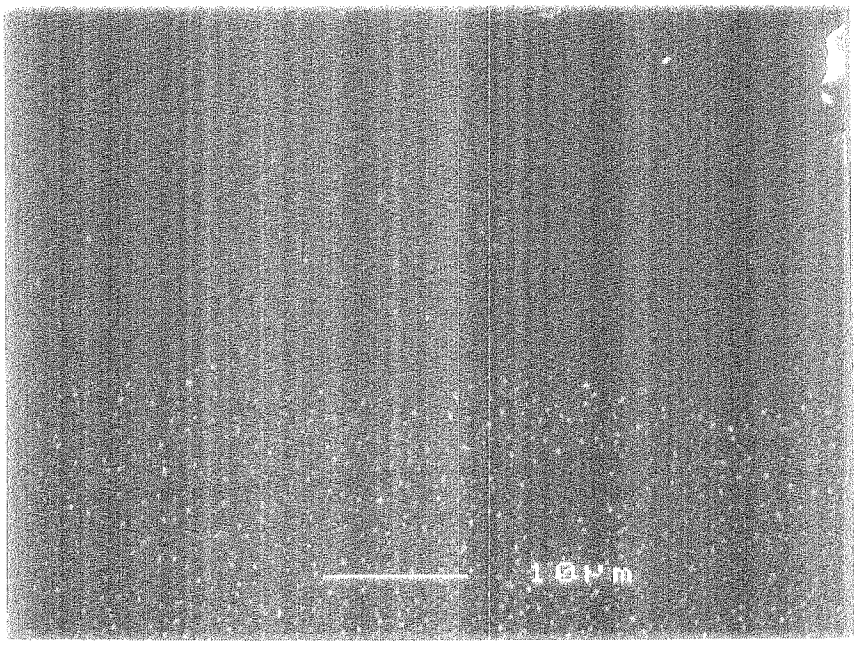

Fig. 29 SEM photomicrograph of cross section of Ni after testing. Tightly bound carbon layer found on the Ni surface, even after ultrasonic cleaning. Small particles of Ni separated and moved away from the surface.

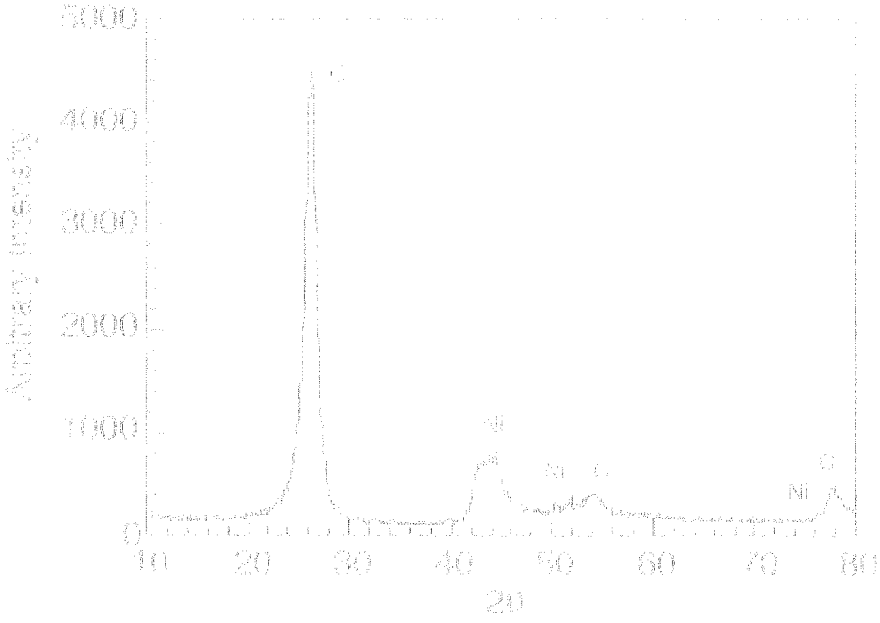

Fig. 30 Typical XRD pattern of the product of metal dusting experiment involving Ni

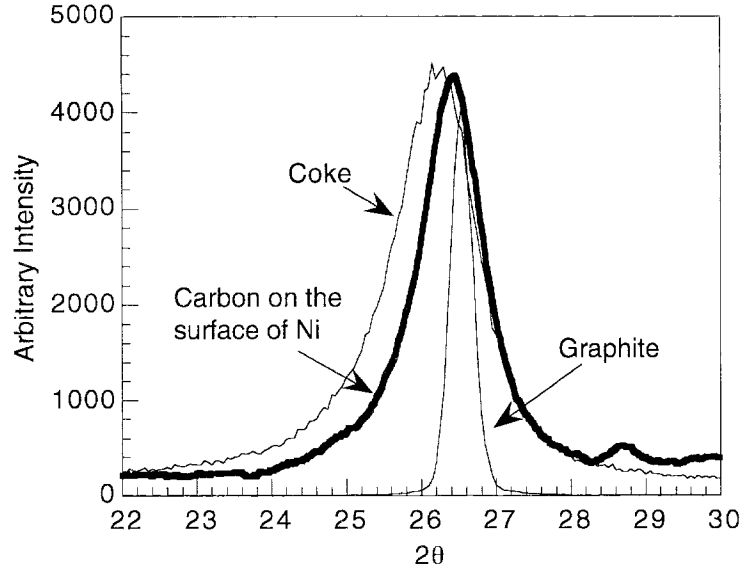

Fig. 31. XRD [002] diffraction peaks for graphite, coke, and carbon on the surface of Ni.

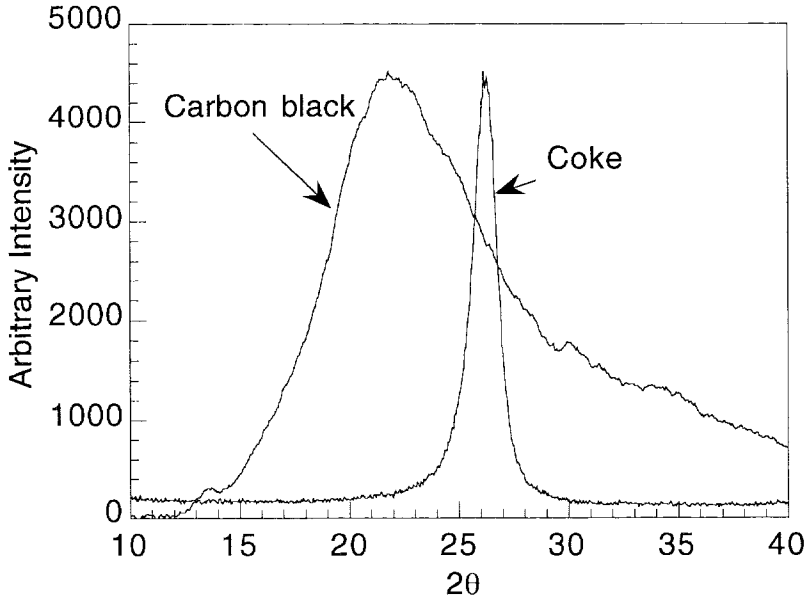

Fig. 32. XRD [002] diffraction peaks for carbon black and coke.

decomposed to nano-size nickel metal particles. These particles served as catalyst in the recrystallization of glassy carbon. Figure 33 shows that the carbon sample with 10% Ni has a much sharper peak than that of the carbon sample without Ni, even though they both were annealed at 1000°C for 100 h. These results clearly indicate that Ni can act as a catalyst to dramatically improve the crystallinity of carbon. Without the catalyst, carbon has less crystallinity at T <1000°C for the following reasons. First, the carbon layers in the graphite structure are easily disoriented because of the weak van der Waals forces between the layers. Second, recrystallization below 1000°C is hindered because the bond in the layers is too strong. The mechanism for metal

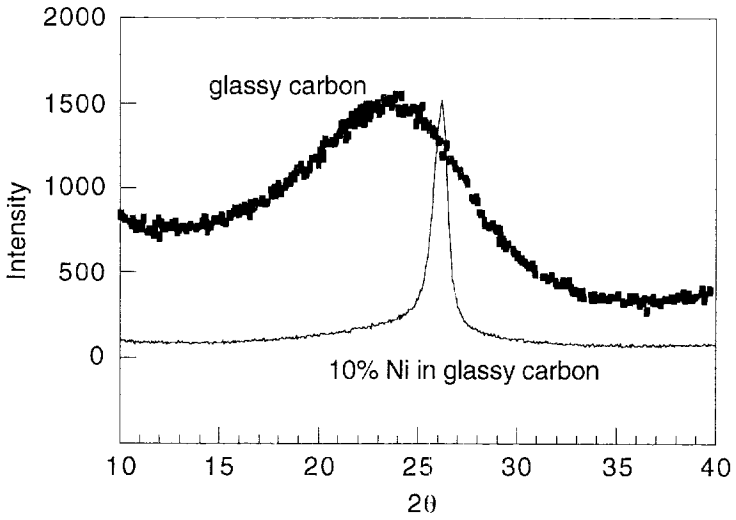

Fig. 33. XRD [002] diffraction peaks of glassy carbon with and without 10% Ni. Samples annealed at 1000°C for 100 h.

dusting of Ni is similar to that for Fe, except that no precipitation of Ni carbide is observed, and carbon diffusion and crystallization of coke on the underside of the metal surface, which enable separation of Ni particles, govern the process.

Behavior of Fe- and Ni-Base Alloys

Table 3 lists the chemical compositions of Fe- and Ni-base alloys that were selected for study. Several of the screening tests (Runs 1 through 9 listed in Table 4) were used to establish the testing conditions for long-term experiments with Fe- and Ni-base alloys (Runs 11-27 in Table 4). One of the important results was that the Fe- and Ni-base alloys should not be exposed in the same run simultaneously, since the Fe-base alloys exhibited a carbon deposit much earlier than the Ni-base alloys, and significant cross contamination between these classes of alloys occurred. Furthermore, the Fe-base alloys with lower Cr contents (e.g., T22) were much more susceptible to carbon deposition and metal dusting attack when exposed under the same temperature, time, and gas composition.

Runs 11 through 14 were conducted to isolate the Fe and Ni specimens during exposure and also to evaluate the influence of H_2O in the exposure environment on the carbon deposition and dusting processes. Runs 15 and 16 were of 1000-h duration and were conducted with Fe- and Ni-base alloys in Gas 2, which simulated the reformer effluent. This gas contained 23 vol.% H_2O, which was achieved by pumping water into the reaction chamber through a specially designed heater. Runs 17 and 18 were conducted to evaluate the carbon deposition/dusting behavior at 482°C (900°F).

Detailed analysis of the specimens from Runs 15 and 16 showed little, if any, deposit of carbon on the specimen surfaces. Carbon was noted primarily on the T22 specimen, and virtually no carbon was detected in Run 16 coincident with Ni-base alloys. The major difference between these runs and the others (Runs 1 through 9) was the amount of H_2O in the exposure environment. Note that the carbon activity established by Gas 2 at 593°C (1100°F) is >2 (see Table 3), yet no deposit of carbon was noted.

Run 19 was conducted to examine the competing effects of oxidation and carbon deposition/metal dusting on alloy behavior. In this run, Fe-base alloys were exposed in Gas 2, but in contrast to Run 15, with only 2 vol.% H_2O. The calculated values for carbon activity in runs 15 and 19 were 2 and 30, respectively, at 593°C (1100°F). In Run 19, a copious amount of carbon was observed on specimen surfaces. Figure 34 shows a macroscopic photograph of the specimens exposed in Runs 15 and 19.

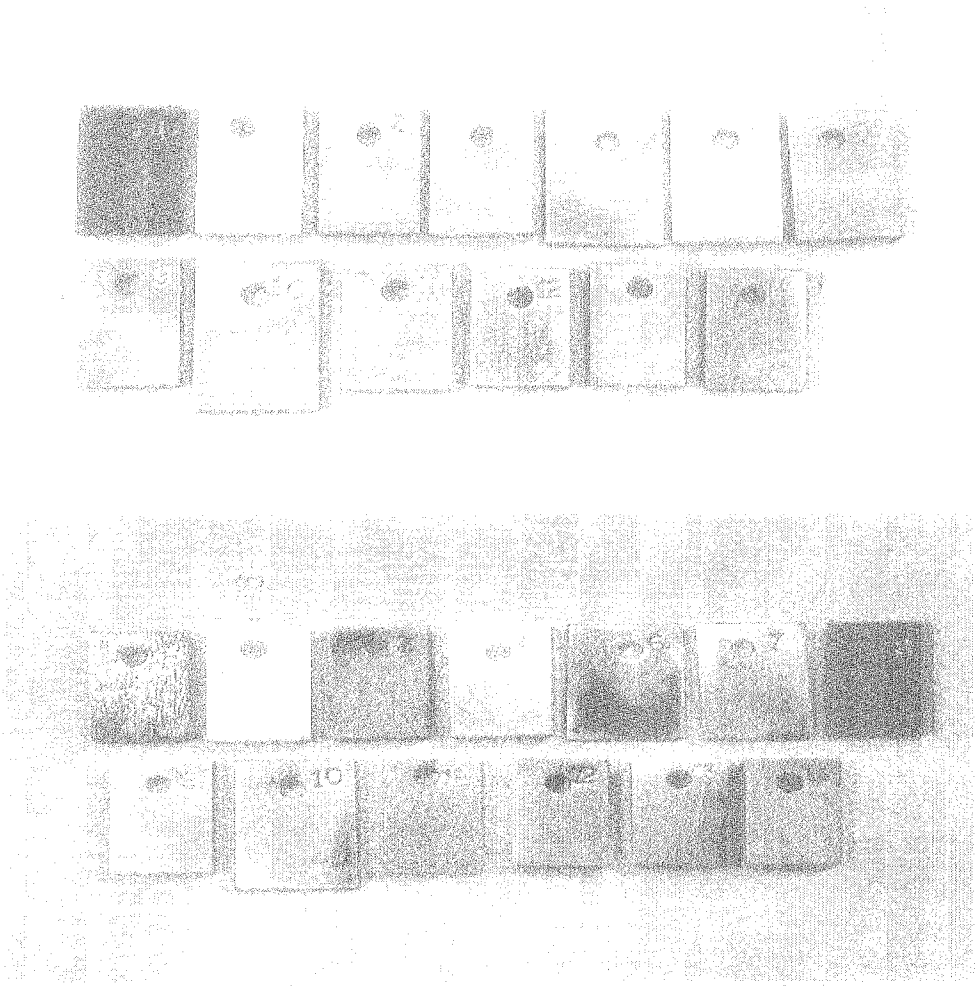

Fig. 34. Macrophotographs of Fe-base alloy specimens after 1000-h exposure at 593°C (1100°F) in Run 15 in Gas 2 with 23.1 vol.% H_2O (top) and Run 19 in Gas 2 with 2 vol.% H_2O (bottom).

Detailed analysis of the surfaces of specimens exposed in Runs 15 and 16 indicated development of oxide layers on most of the specimens. Figures 35–37 show SEM photomicrographs of surfaces of several Fe-base alloys after 1000-h exposure in Gas 2 at 593°C (1100°F). In general, most of the alloys exhibited oxide scales on the surface; however, at isolated locations some carbon deposit adhered to the surface. No significant pitting-type attack was noted in any of the high-T specimens. The only alloy that exhibited a copious amount of carbon deposit and metal dusting was T91 steel, which contained 0.25 wt.% C. Figure 38 shows SEM photomicrographs of several alloys in higher magnification; alloys MA956 and APMT (which contained 6.5 and 4.9 wt.% Al, respectively) developed thin alumina scales, whereas alloys 253MA and 353MA only developed chromia or (Fe,Cr) oxide scales, even though they contained 1.6 and 2.0 wt.% Si, respectively.

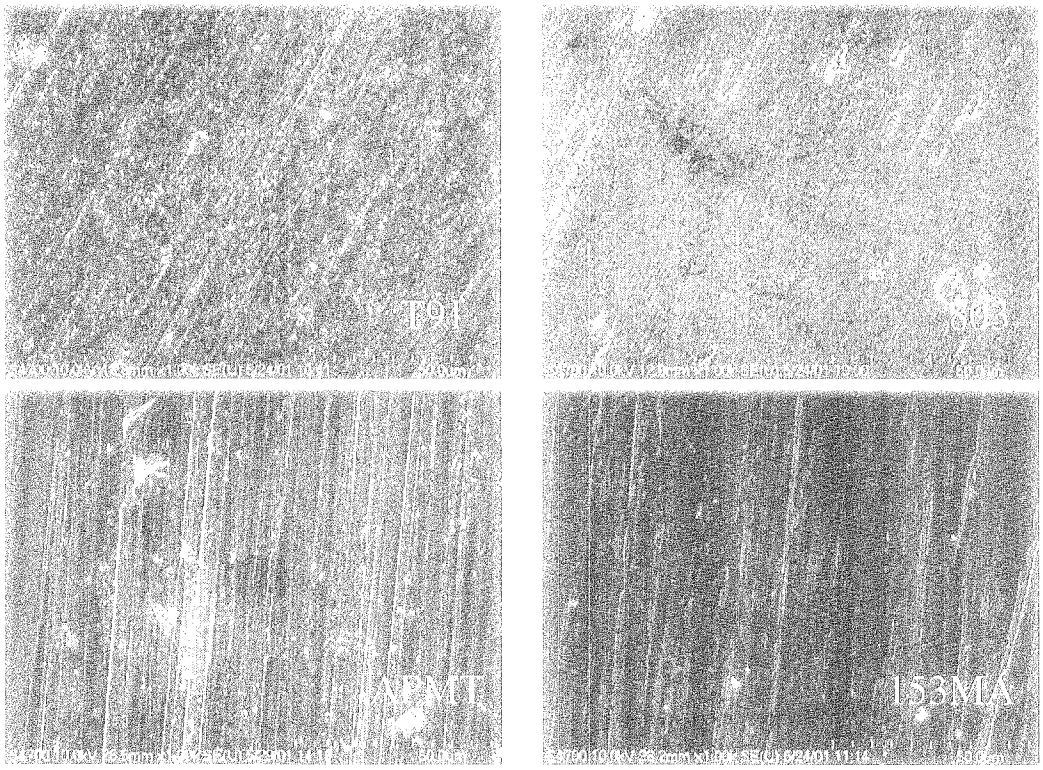

Fig. 38. SEM photomicrographs of surfaces of (top left) T91, (top right) 310S, (bottom left) APMT, and (bottom right) 153MA after 1000-h exposure in Run 16.

Figures 39 and 40 show SEM photomicrographs of surfaces of several Ni-base alloys after 1000-h exposure in Gas 2 at 593°C (1100°F). In general, Ni-base alloys develop much thinner oxide scales than the Fe-base alloys. However, carbon adherence onto the surface of Ni-base alloy is much stronger, as evidenced by the presence of it even after prolonged ultrasonic cleaning. Furthermore, the carbon deposit can be seen as striations, forming preferentially along the polishing lines on the surface. Also, a nonuniform distribution of carbon is evident.

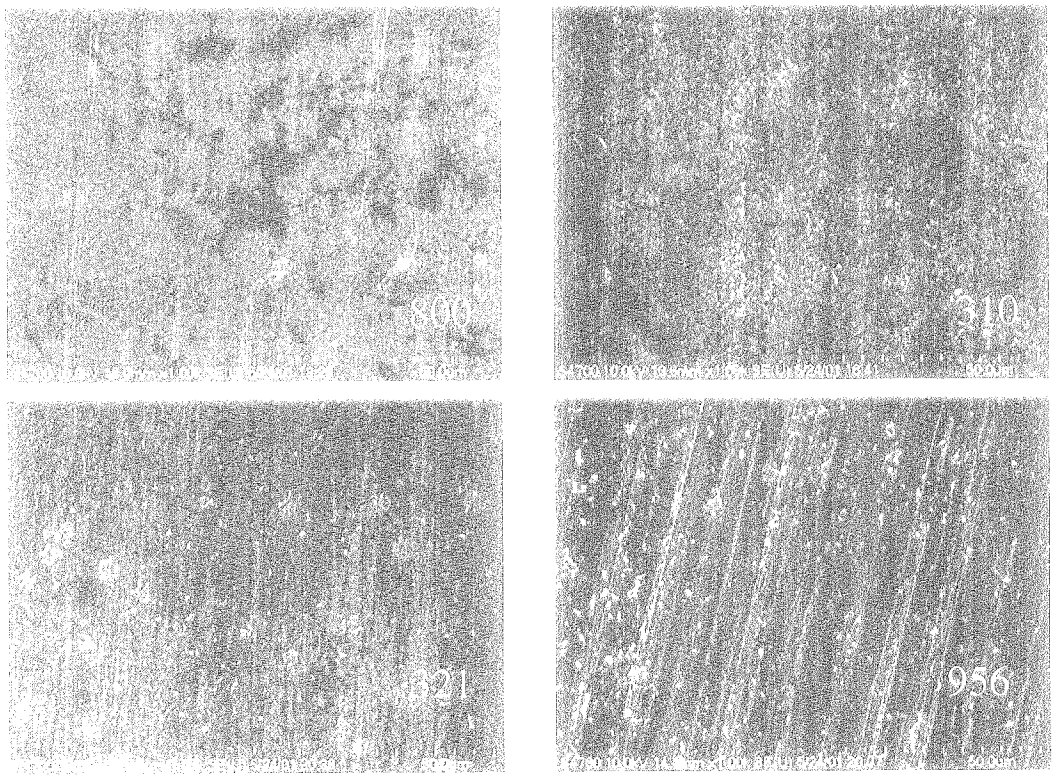

Fig. 36. SEM photomicrographs of surfaces of (top left) Alloy 800, (top right) 310 SS, (bottom left) 321 SS, and (bottom right) MA956 after 1000-h exposure in Run 15.

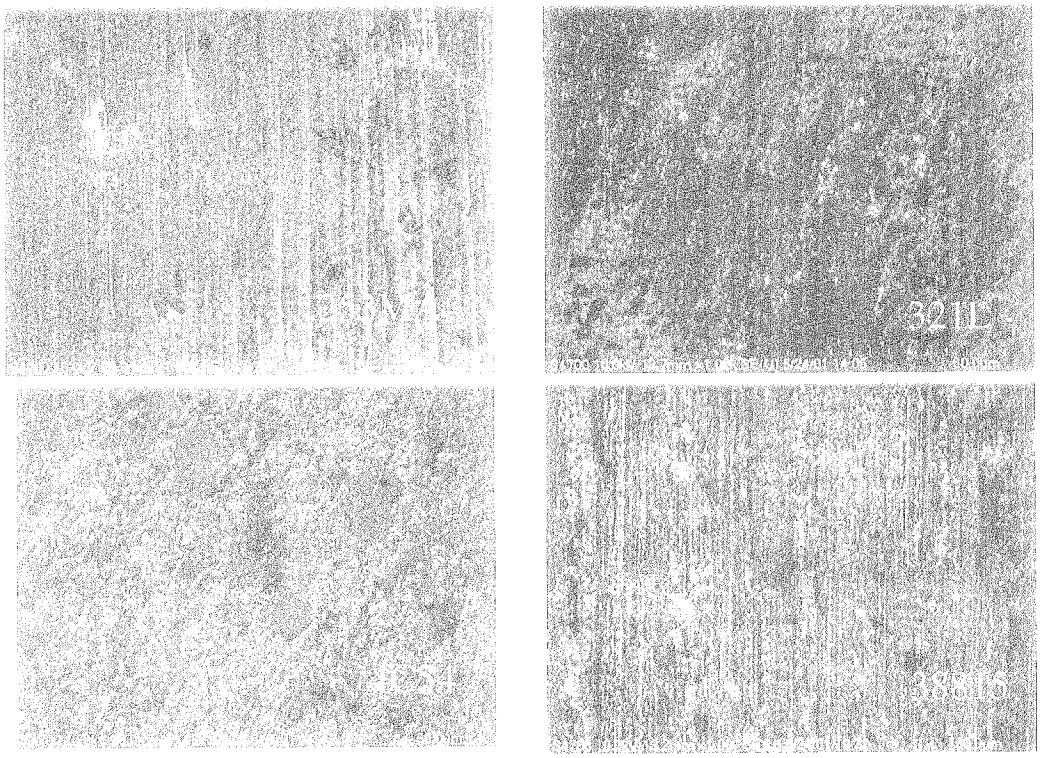

Fig. 37. SEM photomicrographs of surfaces of (top left) 253MA, (top right) 321L, (bottom left) 4C54, and (bottom right) 38815 after 1000-h exposure in Run 15.

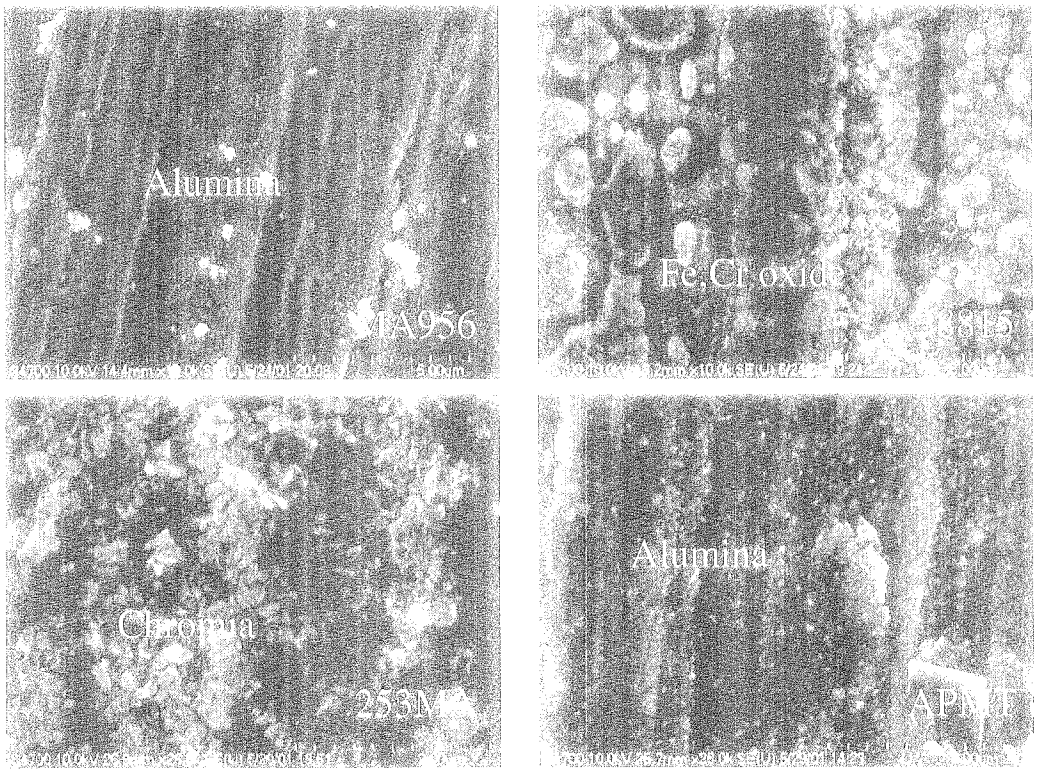

Fig. 38. Higher magnification SEM photomicrographs of surfaces of (top left) MA956, (top right) 316H, (bottom left) 253MA, and (bottom right) APMT after 1000-h exposure in Run 15.

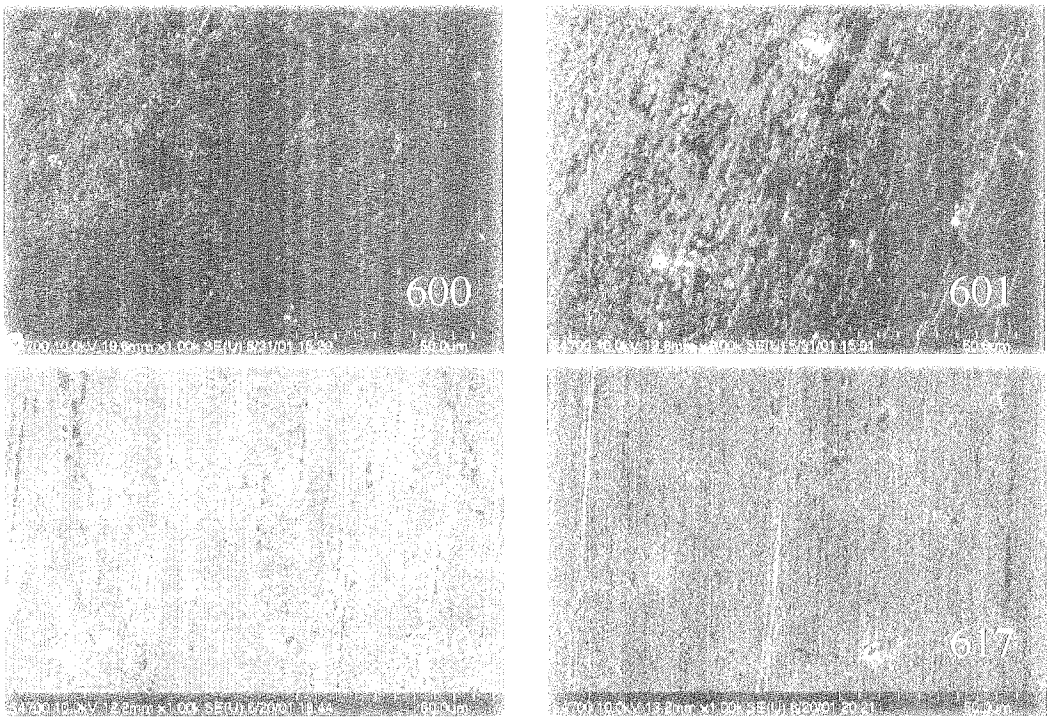

Fig. 39. SEM photomonographs of surfaces of (top left) 600, (top right) 601, (bottom left) 690, and (bottom right) 617 after 1000-h exposure in Run 16.

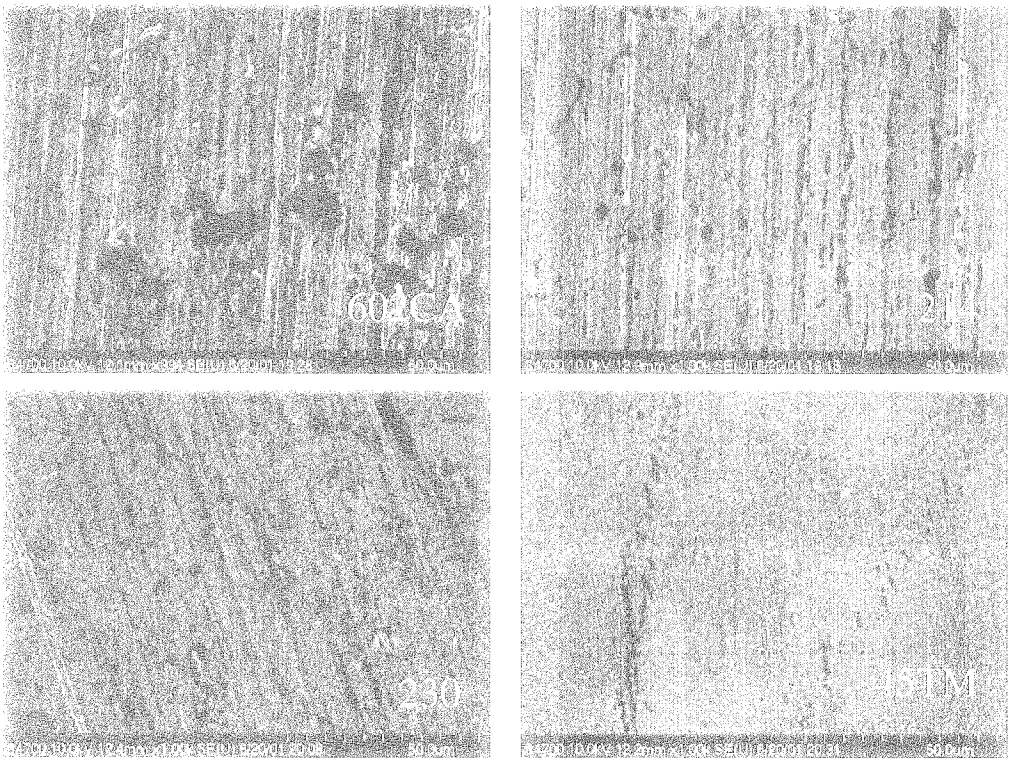

Fig. 40. SEM photomicrographs of surfaces of (top left) 602CA, (top right) 214, (bottom left) 230, and (bottom right) 45TM after 1008-h exposure in Run 16.

To examine the carbon penetration, if any, into the alloys, several of the exposed specimens were cut, mounted, polished, and cross sectioned for SEM and EDX analyses. Figures 41 and 42 show the SEM photomicrographs of cross sections of several Fe- and Ni-base alloys, respectively, after 1008-h exposure in the metal dusting environment. 214 alloy developed a thin oxide scale and virtually no carbon penetration, even after 1008-h exposure. The oxide scale developed on Alloy 800 was porous and discontinuous, and several pits have initiated from the surface (see Fig. 41). Alloy 602 developed a thin oxide scale with almost no carbon penetration into the alloy, indicating that the soot of carbon observed on the surface (see Fig. 36) are primarily adherent to the thin oxide layer.

Among the Ni base alloys that were exposed in Run 16, Alloys 600, 690, 602CA, and 45TM were examined in cross section. Figure 42 shows the SEM photomicrographs of these specimens. The scales were continuous and adherent to the substrate and the thickness was 0.1–0.5 μm after 1008-h exposure in Gas 2 at 593°C (1100°F). None of the alloys exhibited internal penetration of carbon or pitting attack.

Raman spectroscopy was used to analyze the carbon that adhered to the surface of Fe- and Ni-base alloys exposed in Runs 15 and 16. Figure 43 shows Raman spectra (frequency range 1000–1700 cm^{-1}) for carbon that adhered to the surface of alloys 602,

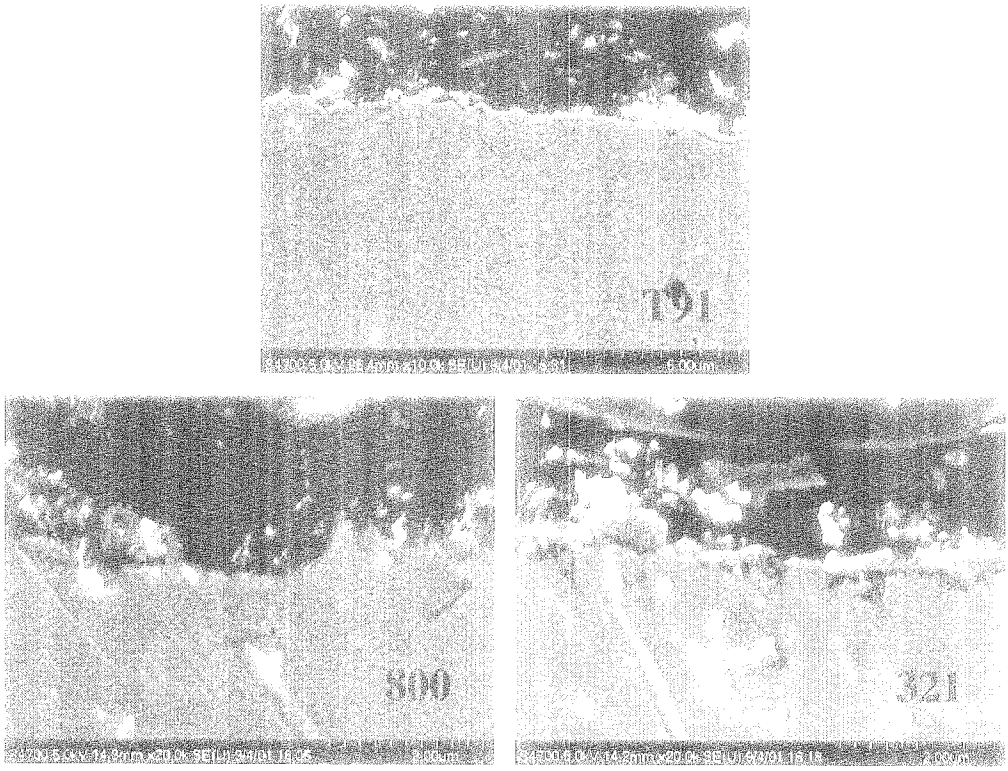

Fig. 41. SEM photomicrographs of cross sections of (top) T91, (bottom left) 800, and (bottom right) 321 after 1000-h exposure in Run 15.

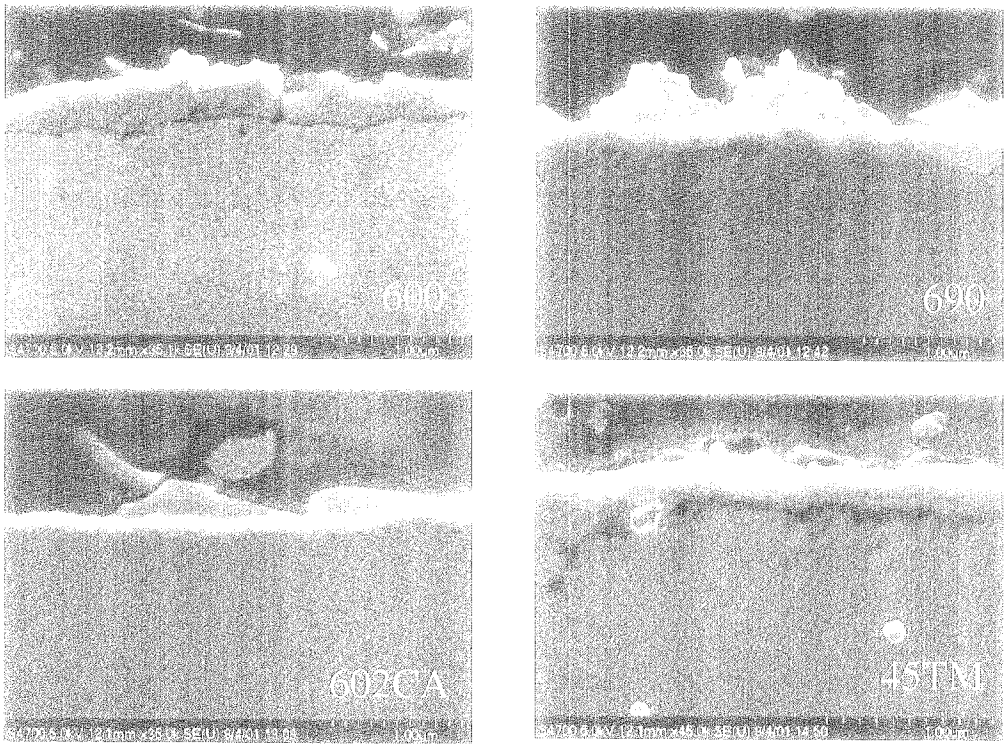

Fig. 42. SEM photomicrographs of cross sections of (top left) 600, (top right) 690, (bottom left) 602CA, and (bottom right) 45TM after 1000-h exposure in Run 15.

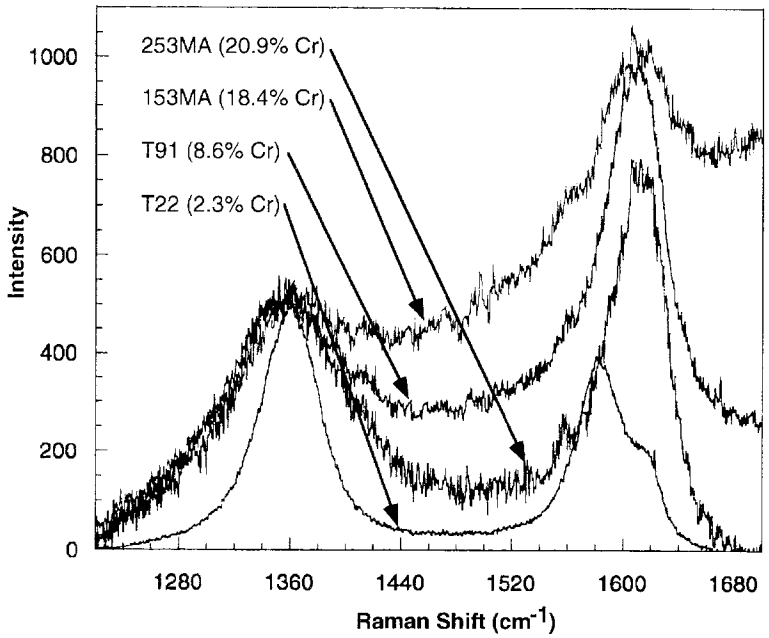

Fig. 43. Raman spectra for carbon adhered to several alloys with different Cr contents after 1000-h exposure in a metal dusting environment in Run 15 at 593°C (1100°F).

T91, 153MA, and 253MA (which had Cr contents of 2.25, 8.6, 18.4, and 20.9, respectively). The alloy T22, which exhibited severe metal dusting attack, had much sharper peaks of carbon when compared with those for the other alloys. Figure 44 shows the Raman spectra (frequency range 200-800 cm^{-1}) for the same Fe-base alloys with different Cr contents, after 1000-h exposure in the metal dusting environment in Run 15 at 593°C (1100°F). The Raman spectra in the frequency range 200-800 cm^{-1} clearly show that alloys with Cr >8.6 wt.% develop oxide scales, as evidenced by the SEM photomicrographs presented earlier. The peaks at ≈550 and ≈680 cm^{-1} correspond to Cr_2O_3 and (Fe,Cr) oxide spinel, respectively. Lack of oxide scale on alloy T22 (which contained 2.3 wt.% Cr) led to metal dusting attack during the 1000-h exposure in Run 15.

Figure 45 shows the Raman spectra (frequency range 200-800 cm^{-1}) for the three Ni-base alloys with different Cr contents after 1000-h exposure in the metal dusting environment in Run 16 at 593°C (1100°F). The Ni-base alloys predominantly developed Cr_2O_3, as indicated by the peak at ≈550 cm^{-1}. The peak height seems to be strongly dependent on the Cr content of the alloy; for example, among the three alloys the peak height is smallest for Alloy 600 (15.4 wt.% Cr) and largest for Alloy 690 (27.2 wt.% Cr). The broad feature in these spectra at ≈660 cm^{-1} is not currently identified but seems to disappear as the Cr level in the alloy increases.

Figures 46 and 47 show the Raman spectra in the frequency ranges of 200-800 cm^{-1} and 1200-1800 cm^{-1}, respectively, for Fe-base alloys with variation in Cr content. All

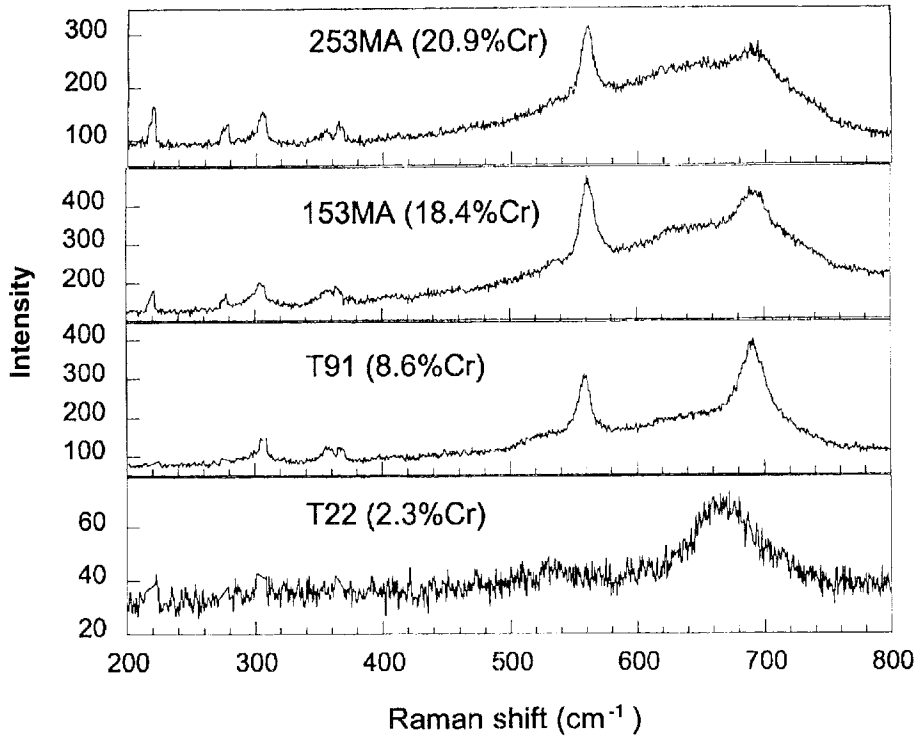

Fig. 44. Raman spectra for surfaces of several Fe-base alloys with different Cr contents after 1000-h exposure in a metal dusting environment in Run 15 at 593°C (1100°F).

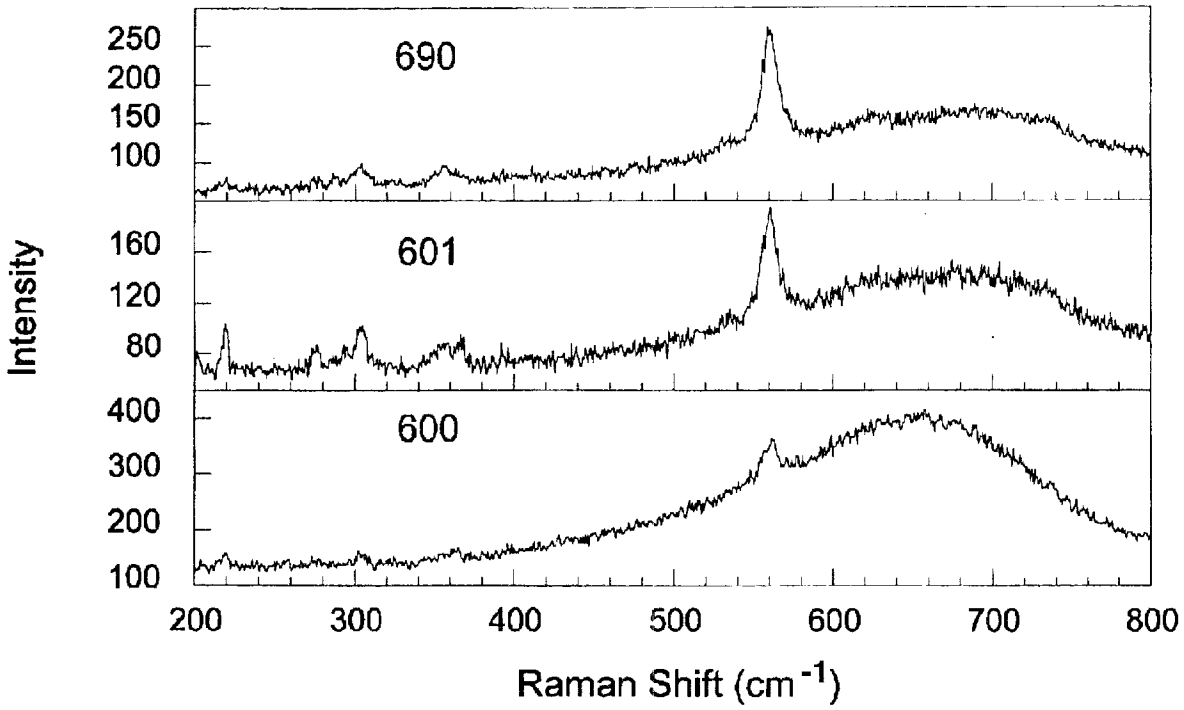

Fig. 45. Raman spectra for surfaces of several Ni-base alloys with different Cr contents after 1000-h exposure in a metal dusting environment in Run 16 at 593°C (1100°F).

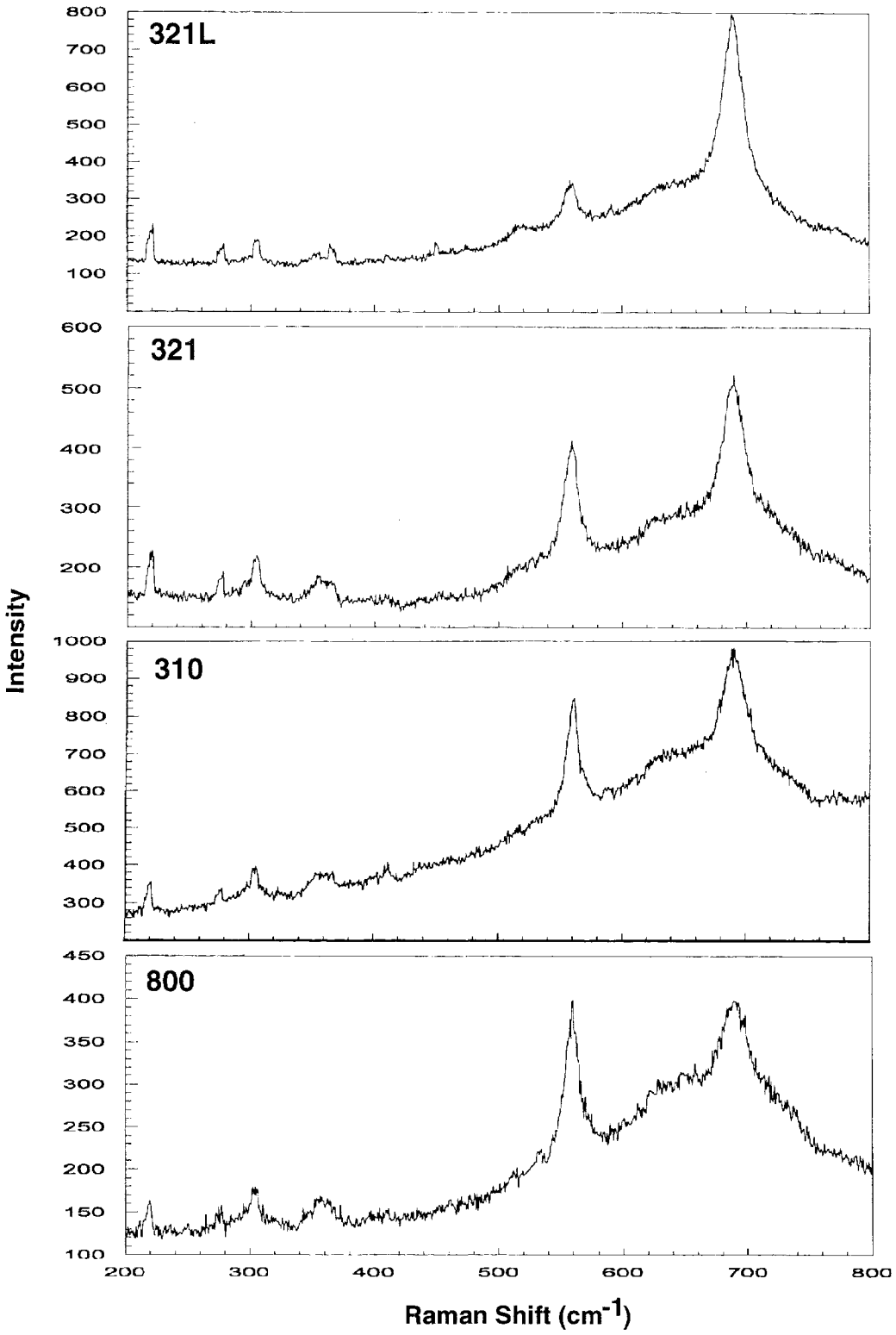

Fig. 46. Raman spectra (frequency range 200-800 cm^{-1}) for surfaces of 300-series stainless steel alloys and Alloy 800 after 1000-h exposure in a metal dusting environment at 593°C (1100°F).

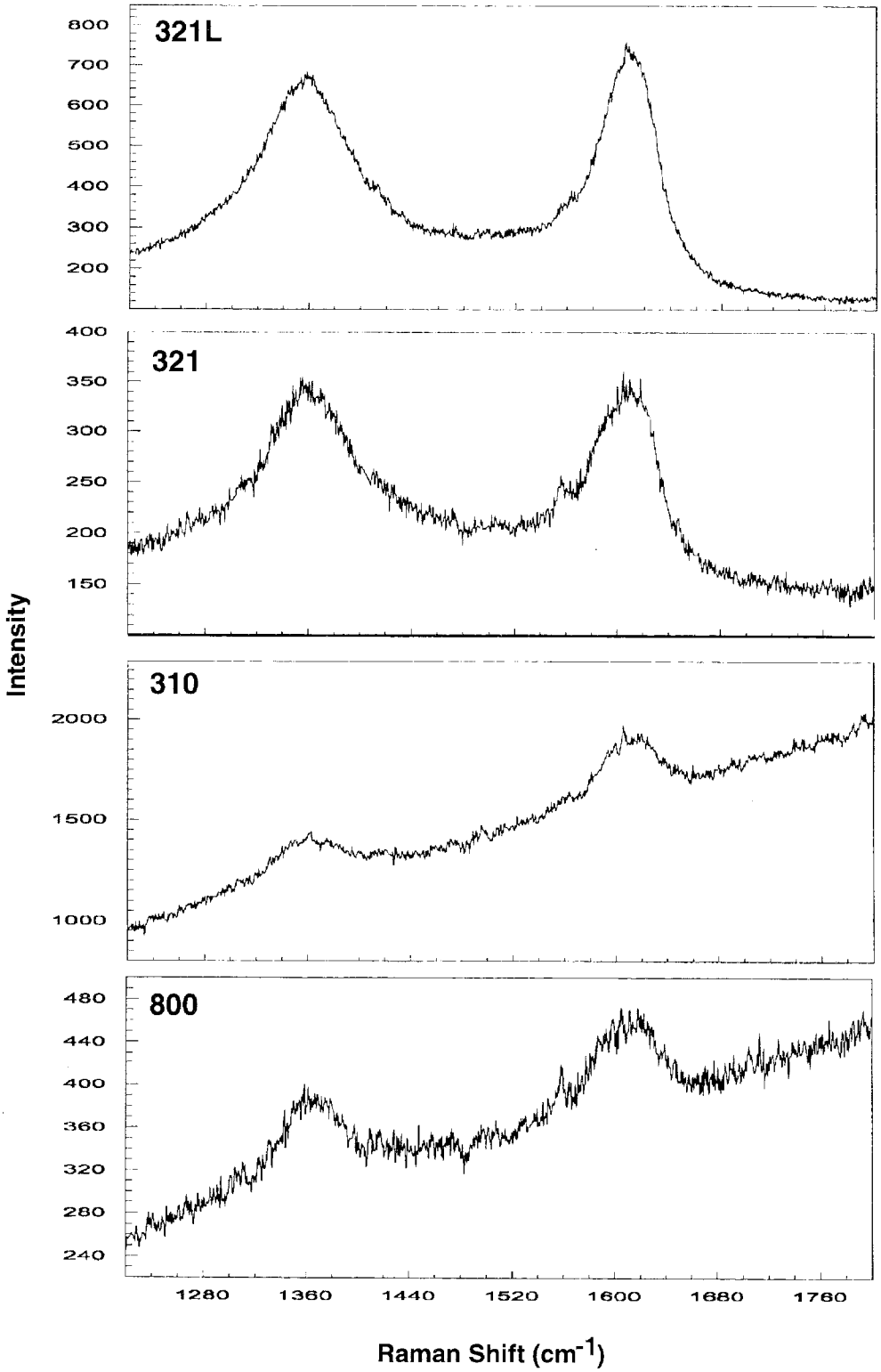

Fig. 47. Raman spectra (frequency range 1200-1800 cm^{-1}) for surfaces of 300-series stainless steel alloys and Alloy 800 after 1000-h exposure in a metal dusting environment at 593°C (1100°F).

the alloys with Cr contents in the range 17.3 to 25.5 wt.% developed Cr_2O_3 and (Fe,Cr) oxide spinel. The Raman spectra for surface carbon in these alloys are also similar but vary in the relative peak height for the D and G bands. Figures 48 and 49 show the Raman spectra in the frequency ranges of 200-800 cm^{-1} and 1200-1800 cm^{-1}, respectively, for several alloys with varying Al content. Even though the Al content of alloys MA956 and APMT is similar, their scaling behavior is somewhat different. Alloy APMT predominantly developed Cr_2O_3 scale, as evidenced by the sharp peak at ≈550 cm^{-1}, whereas the alloy MA956 (which exhibited a much thinner scale) showed a less developed peak at a frequency >550 cm^{-1}. The peak at ≈700 cm^{-1} in the APMT alloy is not presently identified, except that it does not correspond to any Al_2O_3 phase. Even in the higher frequency range (that corresponding to carbon, see Fig. 49), the relative intensities for the D-to-G band for the two alloys are different, but the cause for it is not known. The Raman spectra for the alloys 602CA and 214 (with a lower Al content) are similar in the entire frequency range.

Figures 50 and 51 show the Raman spectra in the frequency ranges of 200-800 cm^{-1} and 1200-1800 cm^{-1}, respectively, for several alloys with varying Si content. The alloys selected for these figures (253MA, 38815, 45TM, and HR160) contain 13.9-28.0 wt.% Cr and 1.6-5.8 wt.% Si. The results showed that all four alloys developed predominantly Cr_2O_3 scale, which is expected based on oxidation studies of Si-containing alloys. In general, Si can form a silica scale at the Cr_2O_3/alloy interface since the diffusion coefficient for Si is much smaller than that for either Cr or Fe, and these alloys can rarely form an external scale of silica at the Si concentration levels present in these alloys. The Raman spectra in the frequency range of 1200-1800 cm^{-1} show similar peaks on all four alloys, indicating that the variation in Si content in these alloys has virtually no effect on the deposition of carbon.

DISCUSSION OF METAL DUSTING INITIATION

The results presented thus far clearly indicate that the gas chemistry used in Runs 15 and 16 can deposit carbon by the reactions that were discussed earlier. Furthermore, decreasing the H_2O content of the gas, thereby increasing the carbon activity (e.g., Run 19), can accelerate carbon deposition. However, whether the deposited carbon can initiate metal dusting in Fe- and Ni-base alloys is strongly influenced by the oxidation characteristics of the alloys. The competition between the oxidation process to form a continuous oxide scale on a given alloy surface and deposition and penetration of carbon will determine the incubation time for metal dusting attack to occur. If an alloy can develop a protective oxide scale fast enough and early during exposure, then subsequent deposition of carbon on top of the oxide layer can delay initiation of metal dusting.

In most earlier studies on metal dusting, the researchers selected gas compositions that yielded carbon activities >>1, which led to deposition of carbon on the specimens from

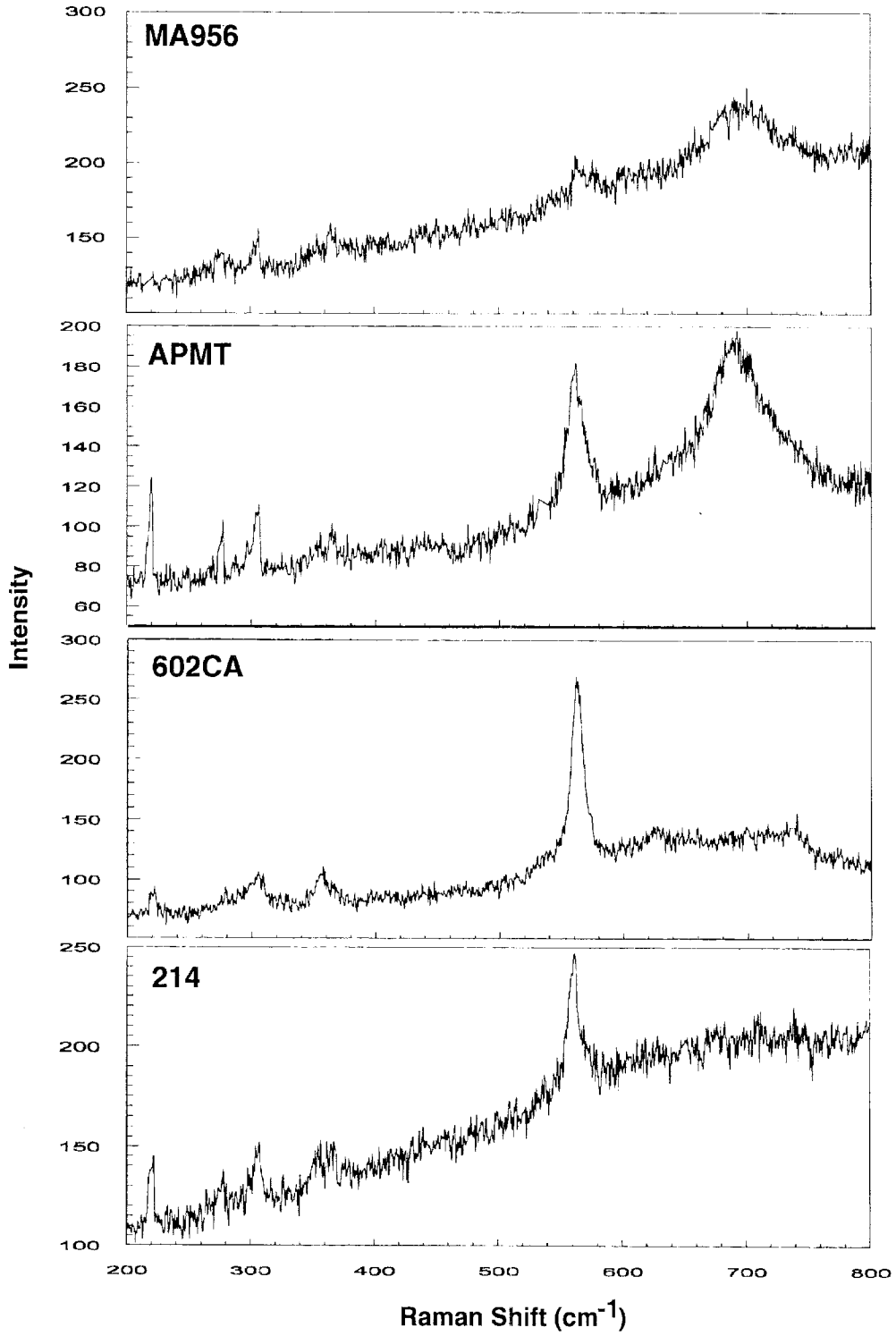

Fig. 48. Raman spectra (frequency range 200-800 cm^{-1}) for surfaces of several Al-containing alloys (MA956, 4.5 wt.%; APMT, 4.9 wt.%; 602CA, 2.3 wt.%; and 214, 3.7 wt.%) after 1000-h exposure in a metal dusting environment at 593°C (1100°F).

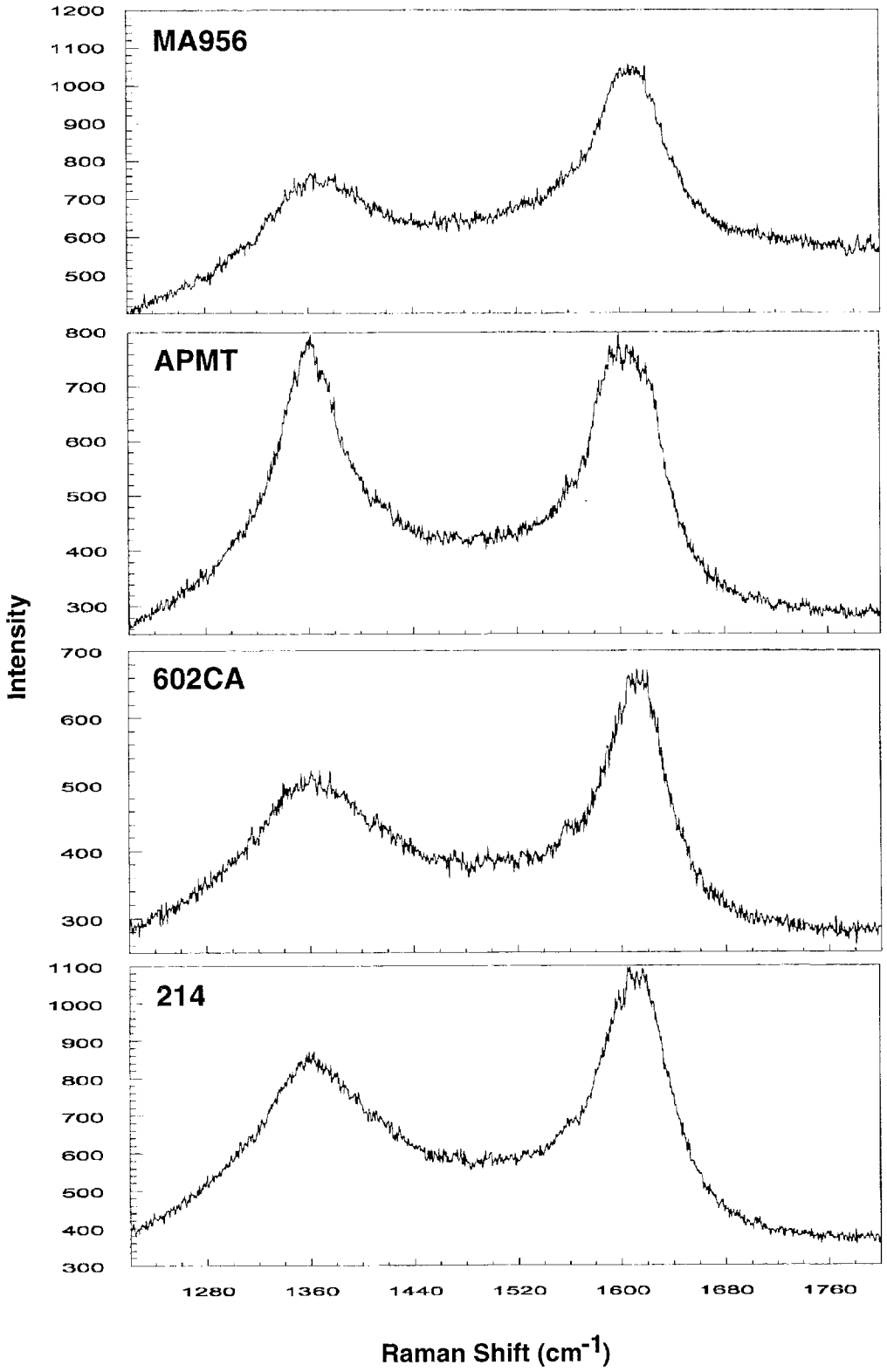

Fig. 49. Raman spectra (frequency range 1200-1800 cm^{-1}) for surfaces of several Al-containing alloys (MA956, 4.5 wt.%; APMT, 4.9 wt.%; 602CA, 2.3 wt.%; and 214, 3.7 wt.%) after 1000-h exposure in a metal dusting environment at 593°C (1100°F).

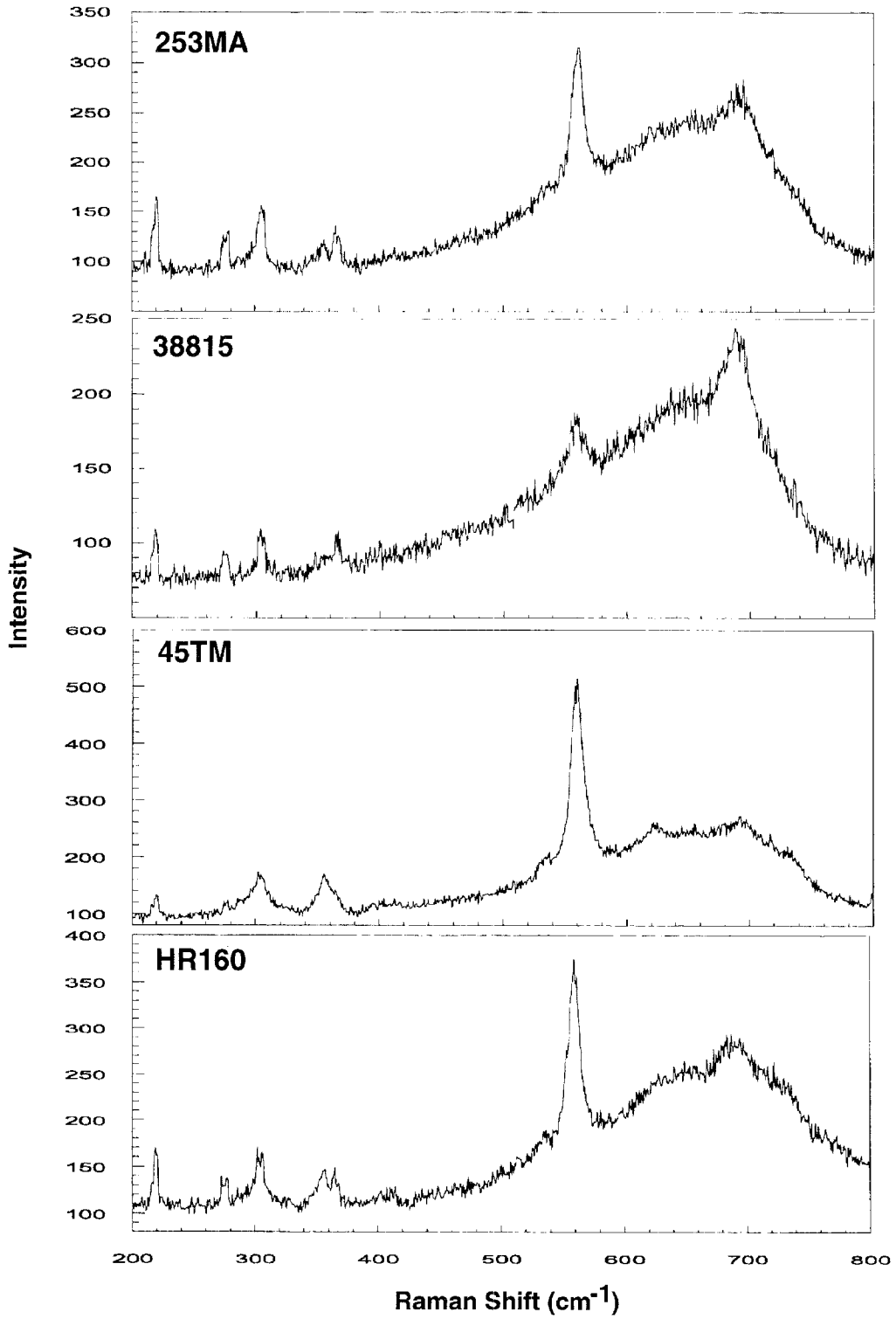

Fig. 50. Raman spectra (frequency range 200-800 cm^{-1}) for surfaces of several Si-containing alloys (253MA, 1.6 wt.%; 38815, 5.8 wt.%; 45TM, 2.7 wt.%; and HR160, 2.8 wt.%) after 1000-h exposure in a metal dusting environment at 593°C (1100°F).

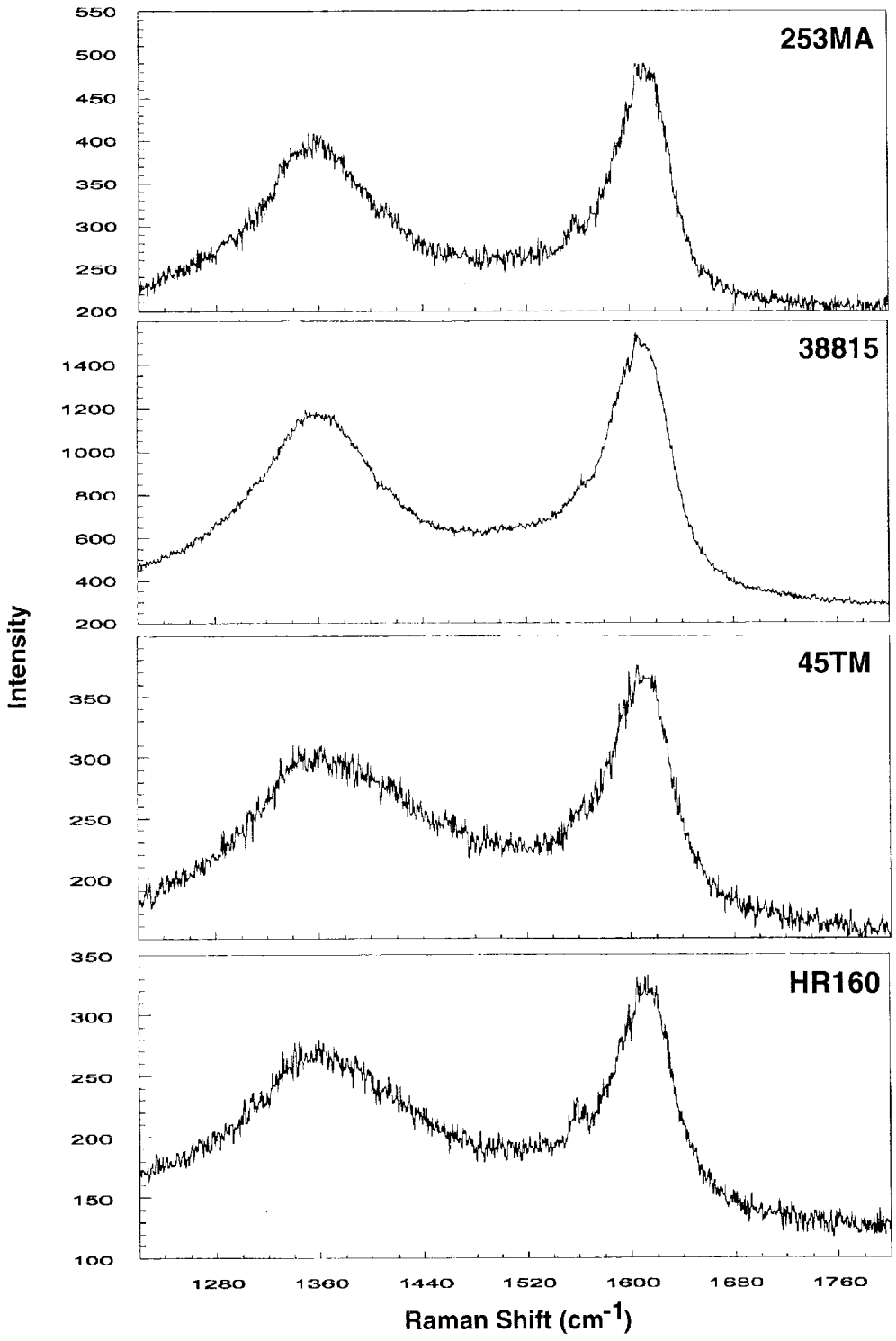

Fig. 51. Raman spectra (frequency range 1200-1800 cm^{-1}) for surfaces of several Si-containing alloys (253MA, 1.6 wt.%; 38815, 5.8 wt.%; 45TM, 2.7 wt.%; and HR160, 2.8 wt.%) after 1000-h exposure in a metal dusting environment at 593°C (1100°F).

the beginning of the exposure.[9,30-32] Besides exposure to high carbon activity, the alloys did not have much time (before carbon deposition) to develop a protective oxide scale. Therefore, the earlier studies emphasized interaction of the deposited carbon with the constituents of the structural alloys and examined the role of alloy-related variables (such as alloy composition; Fe, Cr, and Ni contents; surface preparation; and surface roughness) on alloy degradation. A comparative analysis was conducted on the carbon activities and oxygen partial pressures established in several studies to better understand the role of gas chemistry in the metal dusting behavior of structural alloys.

Table 6 lists the chemical compositions of gases used in several of the studies. The H_2O content in the past studies was in the range 0-2.4 vol.%, whereas we used H_2O contents of 0, 2, and 23 vol.% (the last one is typical of the effluent from a H_2 reformer). Similar to results presented in an earlier section in this report, we calculated the carbon activity of various gas mixtures at several temperatures in the range of 425-760°C (800-1400°F).

Table 6. Gas chemistries used in metal dusting research

	Composition in vol. %				
Researcher	CO	CO_2	CH_4	H_2	H_2O
Grabke (Ref. 9)	24.7	-	-	73.4	1.9
Maier et al. (Ref. 31)	24.4	-	-	73.2	2.4
Baker/Smith (Ref. 32)	70.0	4.0	-	25.3	0.75
Levi et al. (Ref. 33)	25.0	-	-	75.0	-
Natesan et al. (gas 4)	17.5	8.3	-	74.2	-
Natesan et al. (gas 5)	17.6	8.3	-	72.2	2.0
Natesan et al. (gas 2)	18.0	5.6	1.1	52.0	23.0

Table 7 lists the carbon activity values at 593°C (1100°F) calculated for gas mixtures used in past studies and the current program. The calculations are based on whether Reaction 1 or 2 was dominant or equilibrium between different gas species prevailed at the elevated temperature. The carbon activities in past studies have been >>1, irrespective of whether Reaction 1 or 2 dominated the process. If the gases were in thermodynamic equilibrium, the carbon activity in most cases is around 1. A carbon activity value of infinity under the Reaction 1 column (in Table 7) arises because the inlet gas mixture in the study did not contain H_2O, whereas infinity under Reaction 2 arises because the mixture did not contain CO_2. The calculated carbon activity values are based on initial gas compositions. Once Reaction 1 starts, H_2O will be generated, and the local carbon activity will be less than the calculated values in Table 7. However, carbon deposition would have occurred, and it would be almost impossible to develop a protective oxide scale on the alloy surface.

Table 7. Carbon activity and oxygen partial pressure values at 593°C (1100°F), for gas mixtures used by various researchers

Researcher	Carbon activity			Oxygen pressure (in atm), based on		
	Rxn 1	Rxn 2	Eqm	CO/CO_2	H_2/H_2O	Eqm
Grabke (Ref. 9)	47.5	∞	1.2	-	6.7×10^{-28}	7.6×10^{-26}
Maier et al. (Ref. 31)	37.1	∞	1.2	-	1.1×10^{-27}	7.7×10^{-26}
Baker/Smith (Ref. 32)	118.0	165.0	0.8	3.1×10^{-28}	1.0×10^{-28}	3.9×10^{-25}
Levi et al. (Ref. 33)	∞	∞	1.2	-	-	6.9×10^{-26}
Natesan et al. (gas 4)	∞	5.0	1.3	2.2×10^{-26}	-	1.1×10^{-25}
Natesan et al. (gas 5)	32.5	5.0	1.2	2.2×10^{-26}	7.6×10^{-28}	1.2×10^{-25}
Natesan et al. (gas 2)	2.0	7.9	0.7	9.5×10^{-27}	1.2×10^{-25}	2.4×10^{-25}

Table 7 also lists the oxygen partial pressure (pO_2) values at 593°C (1100°F), calculated for three possible assumptions: CO/CO_2 or H_2/H_2O ratio determines the pO_2, or a thermodynamic equilibrium exists between all the gaseous species at the elevated temperature. The calculations indicate that for a given gas composition, the equilibrium pO_2 values are always higher than those established by either CO/CO_2 or H_2/H_2O ratios. If one assumes that the gas composition does not change significantly during flow from the exit of the reformer to low temperature sections of the waste-heat boiler (i.e., the carbon deposition reactions are slow enough that the generation of carbon by catalysis of gas phase constituents causes little change in bulk gas chemistry), then the pO_2 in the environment will be dictated by the higher of the two values calculated from CO/CO_2 and H_2/H_2O ratios.

From the materials standpoint one can analyze the type of interactions between the constituents of the alloy and the environment by means of thermochemical diagrams. Since carbon deposition and formation of the oxide layer on the metal surface are of interest for materials exposed to metal dusting environments, oxygen/carbon diagrams were generated for several temperatures in the range of 400-700°C. Figure 52 shows the oxygen/carbon thermochemical diagrams for Fe, Cr, and Ni calculated for 593°C. The diagrams depict the stability fields for the metals, oxides, and carbides of Fe, Cr, and Ni in terms of carbon and oxygen partial pressures. Superimposed on these diagrams (indicated by boxes) are the oxygen and carbon partial pressure ranges for gas mixtures used by various researchers in metal dusting studies. The calculations show that Fe_3C, Cr_2O_3, Ni, and Ni_3C are the phases that will be stable in the environments used in the laboratory research and in gas mixtures corresponding to the effluent of the H_2 reformer (Gas 2).

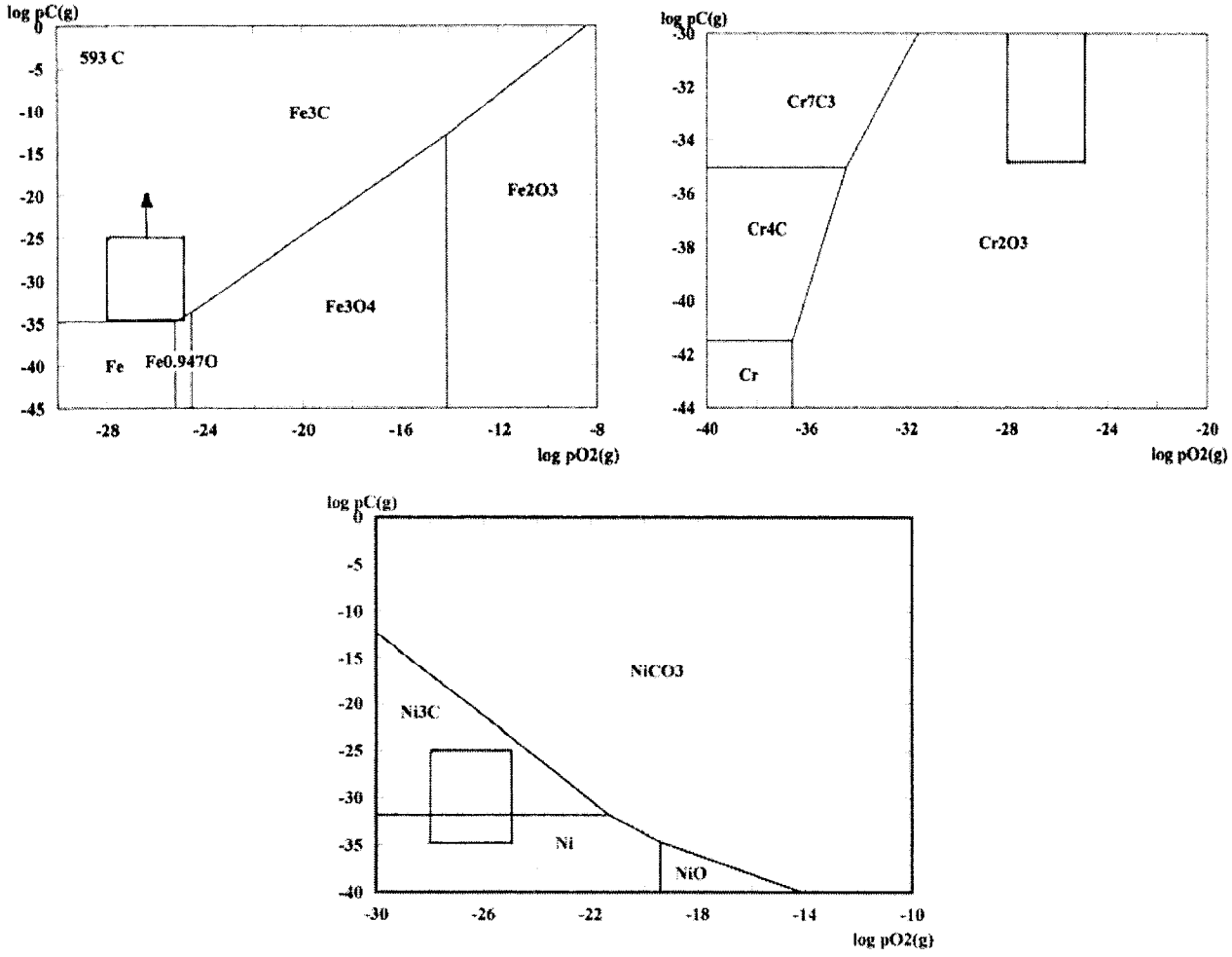

Fig. 52. Oxygen/carbon thermochemical diagrams for Fe, Cr, and Ni calculated for 593°C (1100°F).

For pure Fe and for Fe-base alloys containing low concentrations of Cr (e.g, T22), the calculations indicate that Fe_3C would be the primary phase that forms upon exposure to the metal dusting environment. This observation has been validated by experimental results reported earlier in this report (see Fig. 14 for example). In the case of high-Cr alloys of both Fe- and Ni-base types, pure Cr oxide or Cr-rich oxide will be the stable phase that form upon exposure of the alloy to metal dusting environments, unless precipitous deposition of carbon occurs from the beginning of exposure such that the alloy surface is completely covered with carbon and no time is available to develop an oxide scale. We believe such was the case in most of the earlier studies, which had a_C >>1 and extremely low H_2O content. In Runs 15 and 16 conducted at ANL, the H_2O content of Gas Mixture 2 was 23 vol.%, and a_C was somewhat greater than 1. For this condition, the alloys exhibited oxide scales with subsequent deposition of carbon on top of the oxide.

In reformers, the metal dusting attack generally occurs over a period of years of service, while in laboratory studies the attack occurs over a period of a few hours to few days. Thus, in the reformer, the degradation process is dictated by the breakdown of the oxide scale, while in the laboratory studies, the attack begins right from the start. The ANL program will simulate the environments that are prevalent in reformer systems and examine the competition between the oxide scale development and its breakdown leading to metal dusting attack. Therefore, an understanding of the incubation period and initiation time for metal dusting morphology (such as surface pits) will be emphasized.

PERFORMANCE OF PACK-DIFFUSION COATINGS

Coatings can minimize gas phase reactions by lack of availability of metal surfaces for catalysis. This, in turn, can minimize or eliminate coking and carbon deposition. Furthermore, coatings can act as barriers to carbon ingress into the substrate alloy since carbon diffusion through oxide scales is generally orders of magnitude lower than through the alloys. Among the oxides, the potential candidates as coatings are chromia, alumina, and silica. Iron oxide may not be a viable candidate unless the oxide-to-carbide reaction is slow enough that oxide can be maintained for the desired service life.

Three approaches are being examined for the development of oxide surface layers for evaluation in metal dusting environments. The first approach is to develop the oxide layer on the structural alloys by a preoxidation treatment. In this case, the specimens are exposed to either air or a low-pO_2 (established by H_2/H_2O or CO/CO_2 gas mixtures) environment at temperatures between 750 and 900°C. Generally, depending on the Cr content of the alloy and pO_2 in the exposure environment, the alloys develop (Fe,Cr) or (Ni,Cr) spinels or "pure" Cr oxide on the surface. Regulating the exposure time and temperature can control the thickness of the oxide layer.

The second approach involves a pack-diffusion process in which the alloy surface is enriched in oxide-forming elements such as Al, Cr, and/or Si. Subsequently, the surface-enriched alloy is oxidized in air to develop the oxide scale of choice. Pack diffusion is widely used to confer oxidation resistance on ferrous alloys. Pack diffusion processes include aluminizing, chromizing, and siliconizing. Specimens/components are packed in metal powders in sealed heat-resistant retorts and heated inside a furnace to precisely controlled temperature-time profiles. In the aluminizing process, a source of Al reacts with a chemical activator on heating to form a gaseous compound (e.g., pure Al with NaF to form AlF). This gas is the transfer medium that carries aluminum to the component surface. The gas decomposes at the substrate surface, depositing Al and releasing the halogen activator. The halogen activator returns to the pack and reacts with the Al again. Thus, the transfer process continues until all of the aluminum in the pack is used or until the process is stopped. The coating forms at temperatures ranging from 700 to 1100°C over a period of several hours.

Specimens with Al (termed "alonizing") and Cr/Si (termed "ChromePlexing") enrichment were obtained from Alon Surfaces for evaluation in metal dusting environments. Substrates selected for Al enrichment included three Fe-base alloys (T22, 800, and 321 stainless steel) and three Ni-base alloys (601, 625, and HR160). Substrates selected for ChromePlexing included only the three Fe-base alloys since it was not feasible to enrich Cr/Si on Ni-base alloys.

The third approach is thermal spraying. This surface treatment involves injecting energy into the surface of the work piece so that adhesion can take place. Conventional surface finishing methods involve heating an entire component, but the thermal spray technique usually adds energy and material into the surface, keeping the bulk of the object relatively cool and unchanged. This allows surface properties to be modified with minimal effect on the structure and properties of the underlying material. Coatings can be sprayed from rod or wire stock or from powdered materials. The material (e.g., wire) is fed into a flame, where it is melted. The molten stock is then stripped from the end of the wire and atomized by a high velocity stream of compressed air or other gas, which propels the material onto a prepared substrate or workpiece. The basic steps involved in any thermal coating process are substrate preparation, masking and fixturing, coating, finishing, inspection, and stripping (if necessary). Roughening is necessary for most of the thermal spray processes to ensure adequate bonding of the coating to the substrate. Specimens with a thermal spray coating of FeAl are included for evaluation in metal dusting environments.

Figures 53-55 show SEM photomicrographs of cross sections of alonized Fe-base alloys (T22, 321 stainless steel, and Alloy 800) along with elemental profiles as a function of coating thickness obtained by EDX analysis. The aluminum concentration at the surface of all three alloys in the as-coated condition was in a range of 35-45 wt.%. The depth profile in T22 shows a gradual decrease in Al concentration to a depth of ≈300 μm. The aluminum concentration profile in 321 stainless steel (which contains ≈10.3 wt% Ni) is less gradual, but the depth of Al-enriched layer is ≈200 μm. In Alloy 800 (which contains 31.7 wt.% Ni) a layer of Ni_3Al intermetallic forms on the interface between the Al enriched layer and the alloy substrate. This layer seems to slow the diffusion of Al into the substrate, with the result that the Al concentration profile is much flatter (28-36 wt.% Al) over a distance of 140 μm, after which the Al concentration drops sharply.

Figures 56-58 show SEM photomicrographs of cross sections of ChromePlexed Fe-base alloys (T22, 321 stainless steel, and Alloy 800) along with elemental profiles as a function of coating thickness obtained by EDX analysis. Chromium and silicon concentrations at the surface of T22 steel were 12 and 2.5 wt.%, respectively. The elemental profiles show that these concentrations remain fairly constant up to a depth

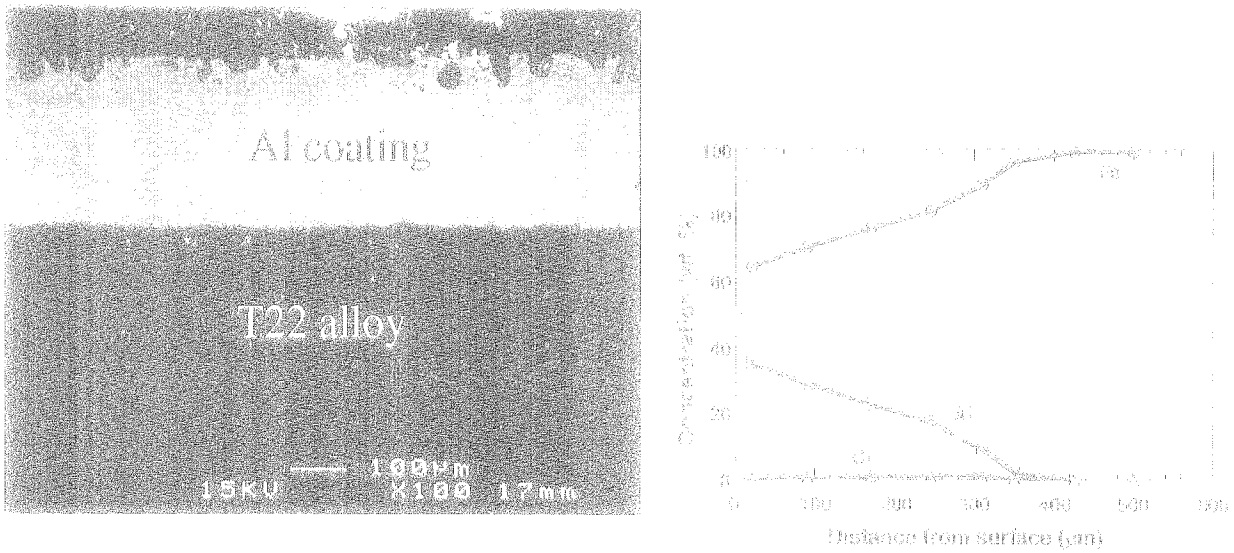

Fig. 53. SEM photomicrograph of cross section of aluminized T22 steel and EDX elemental depth profiles of Al and Fe for the specimen in the as-coated condition.

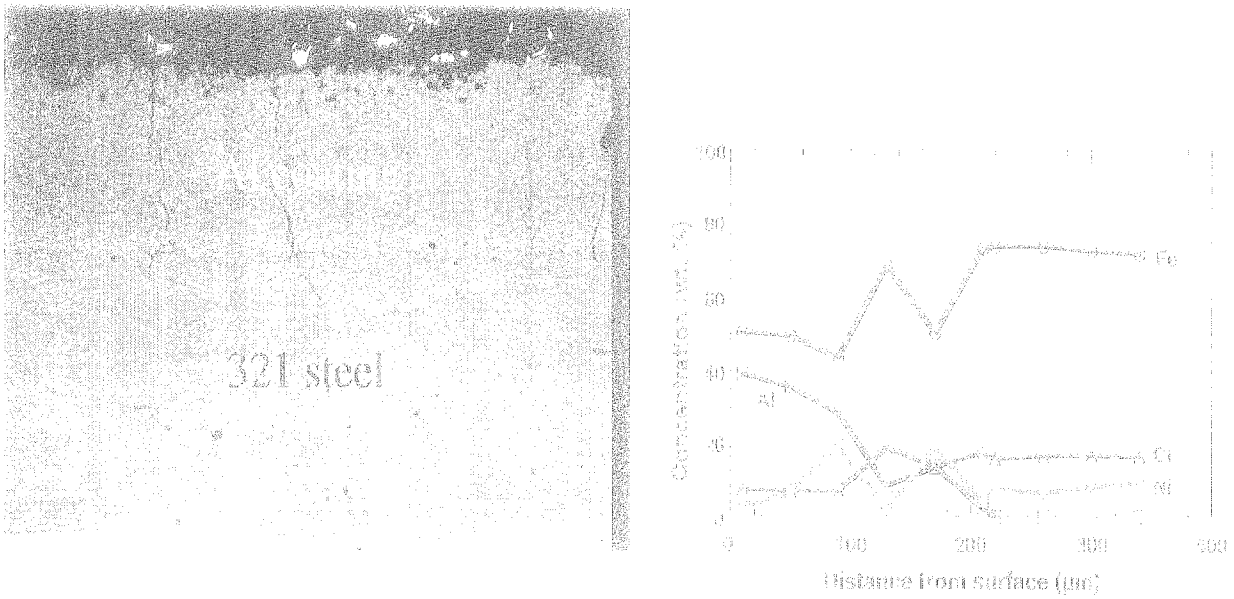

Fig. 54. SEM photomicrograph of cross section of aluminized 321 stainless steel and EDX elemental depth profiles of Al, Fe, Cr, and Ni for the specimen in the as-coated condition.

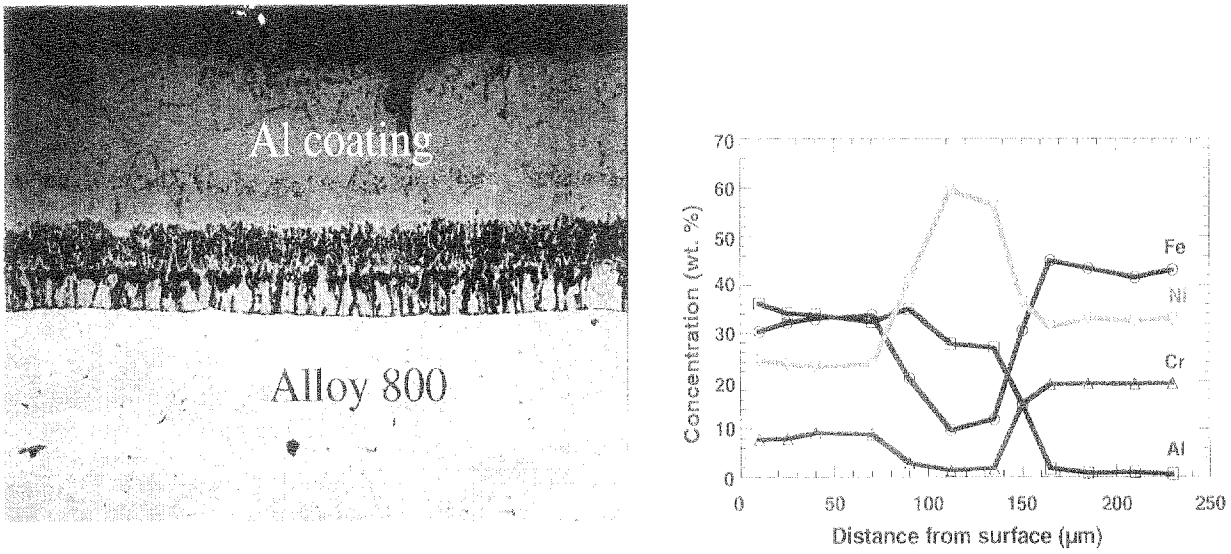

Fig. 55. SEM photomicrograph of cross section of alonized Alloy 800 and EDX elemental depth profiles of Al, Fe, Cr, and Ni for the specimen in the as-coated condition.

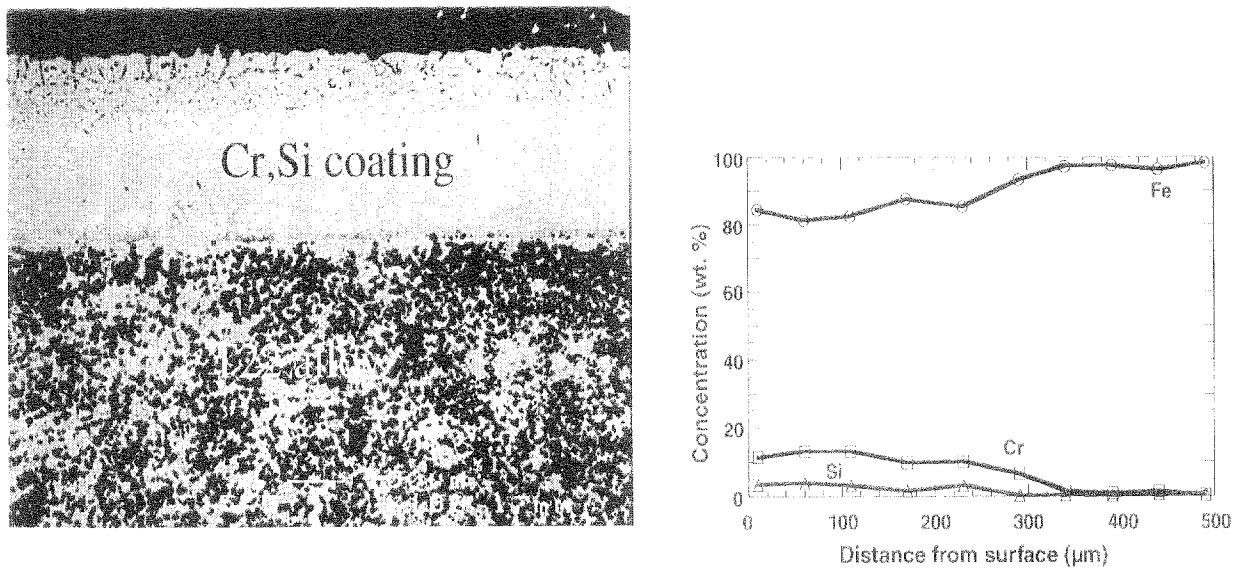

Fig. 56. SEM photomicrograph of cross section of ChromePlexed T22 steel and EDX elemental depth profiles of Si, Fe, and Cr for the specimen in the as-coated condition.

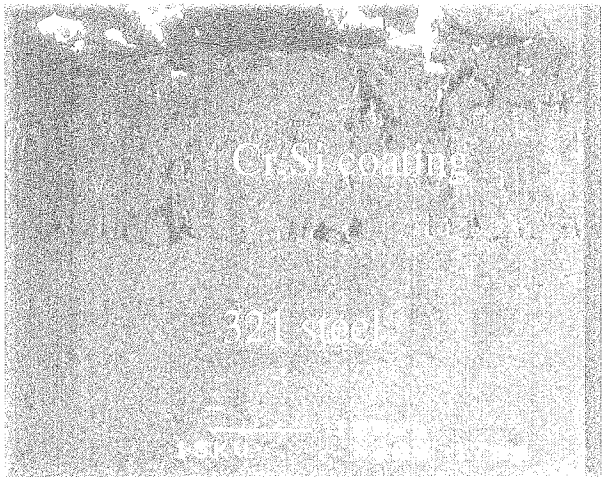

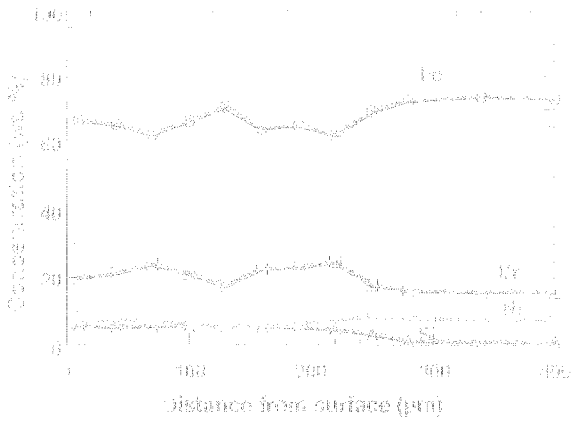

Fig. 57 – SEM photomicrograph of cross section of ChromePlexed 321 stainless steel and EDX elemental depth profiles of Si, Fe, Cr, and Ni for the specimen in the as-coated condition.

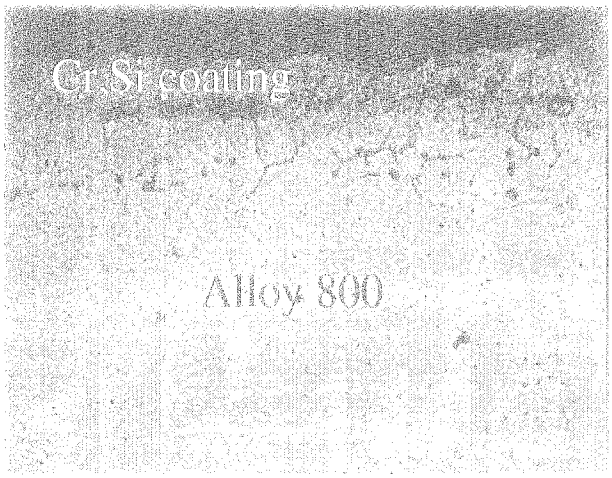

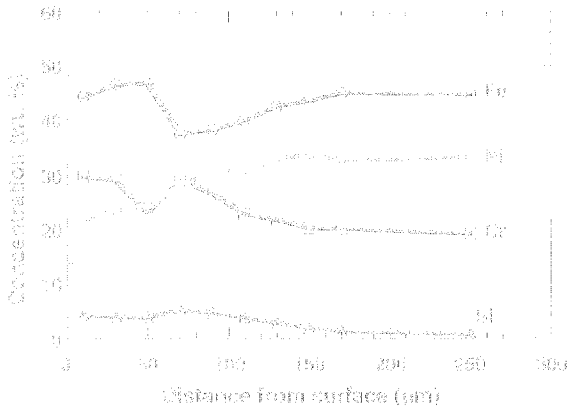

Fig. 58 – SEM photomicrograph of cross section of ChromePlexed Alloy 800 and EDX elemental depth profiles of Si, Fe, Cr, and Ni for the specimen in the as-coated condition.

of ~250 µm. In the case of 321 stainless steel, the Cr and Si concentrations were ~20-25 and ~0 wt.%, respectively, to a depth of 250 µm. The Cr concentration in Alloy 800 was in the range of 20-30 wt.%, while the Si content was similar to that of 321 stainless steel.

Specimens with pack-diffusion coatings were oxidized in air for 200 h at 900°C (1652°F) to develop the oxide scales and were exposed to Gas 2 at 593°C (1100°F) for 142 h in Run 27. Figures 60-63 show SEM photomicrographs of the surfaces of aluminized specimens after oxidation and oxidation/metal dusting treatments. Similar photomicrographs for the ChromeNexed specimens are shown in Figs. 62-64. In general, the oxidized surface layers were intact after exposure to the metal dusting environment. There was some discoloration of the pre-oxidized specimens after exposure to the carbonaceous atmosphere but detailed Raman analysis of the specimen surfaces showed almost no carbon. Additional long-term experiments are planned with several of the surface-modified alloys.

PROJECT SUMMARY

The deposition of carbon from carbonaceous gaseous environments is prevalent in many chemical and petrochemical processes, such as reforming systems, syngas production systems, iron reduction plants, and others. One of the major consequences of carbon deposition is the degradation of structural materials by a phenomenon known as "metal dusting." There are two major issues of importance in metal dusting. First is formation of carbon and subsequent deposition of carbon on metallic materials. Second is the initiation

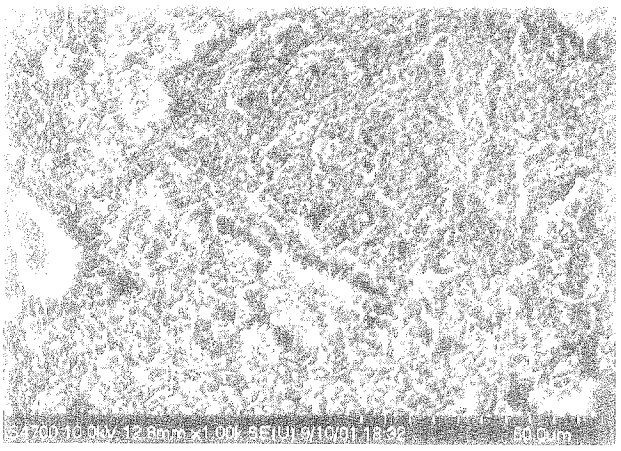

Oxidized at 900°C

Oxidized at 900°C and metal dusted at 593°C (1100°F)

Fig. 60. SEM photomicrograph of surface of aluminized 321 steel after (left) oxidation at 900°C in air and (right) oxidation at 900°C followed by metal dusting exposure for 142 h at 593°C.

Oxidized at 900°C

Oxidized at 900°C and metal dusted at 593°C (1100°F)

Fig. 6b – SEM photomicrograph of surface of aluminized 321 stainless steel after (left) oxidation at 900°C in air and (right) oxidation at 900°C followed by metal dusting exposure for 142 h at 593°C.

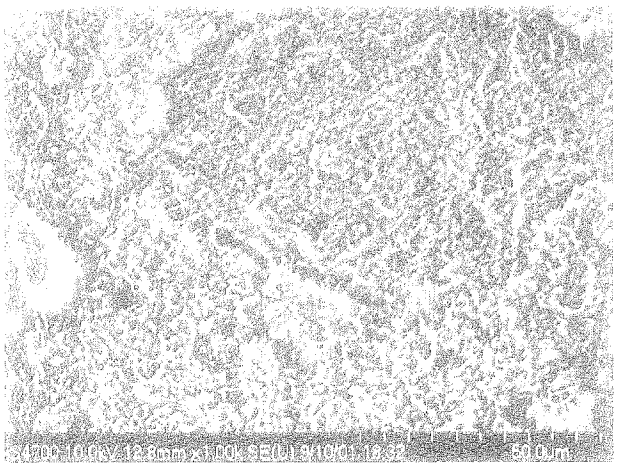

Oxidized at 900°C

Oxidized at 900°C and metal dusted at 593°C (1100°F)

Fig. 6c – SEM photomicrograph of surface of aluminized Alloy 800 after (left) oxidation at 900°C in air and (right) oxidation at 900°C followed by metal dusting exposure for 142 h at 593°C.

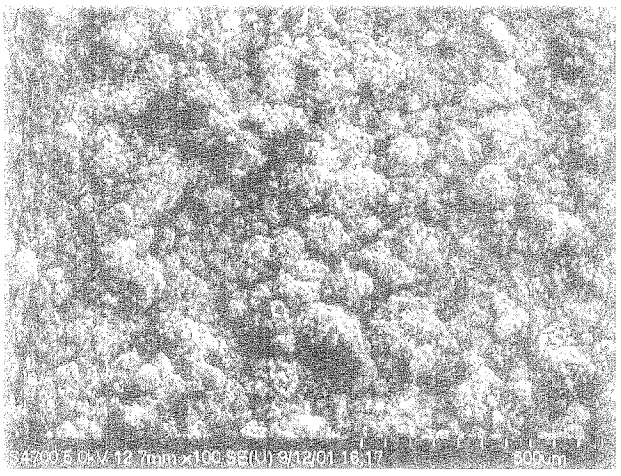

Oxidized at 900°C

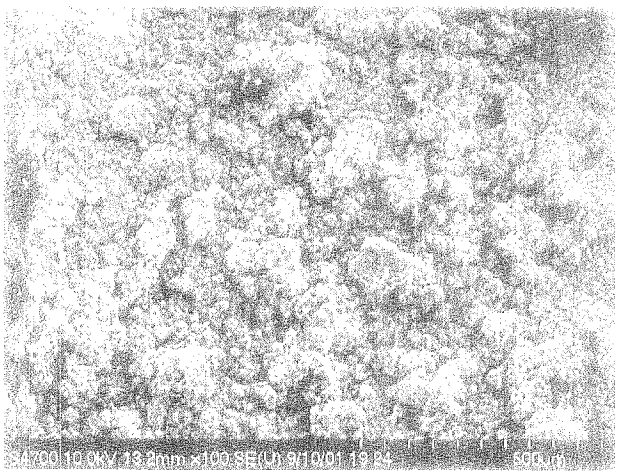

Oxidized at 900°C and
metal dusted at 593°C (1100°F)

Fig. 52. SEM photomicrograph of surface of ChromeFlexed 422 steel after (left) oxidation at 900°C in air and (right) oxidation at 900°C followed by metal dusting exposure for 142 h at 593°C.

Oxidized at 900°C

Oxidized at 900°C and
metal dusted at 593°C (1100°F)

Fig. 53. SEM photomicrograph of surface of ChromeFlexed 321 stainless steel after (left) oxidation at 900°C in air and (right) oxidation at 900°C followed by metal dusting exposure for 142 h at 593°C.

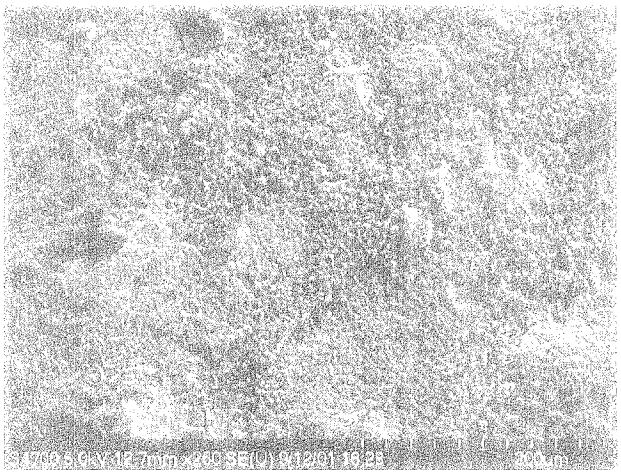

Oxidized at 900°C

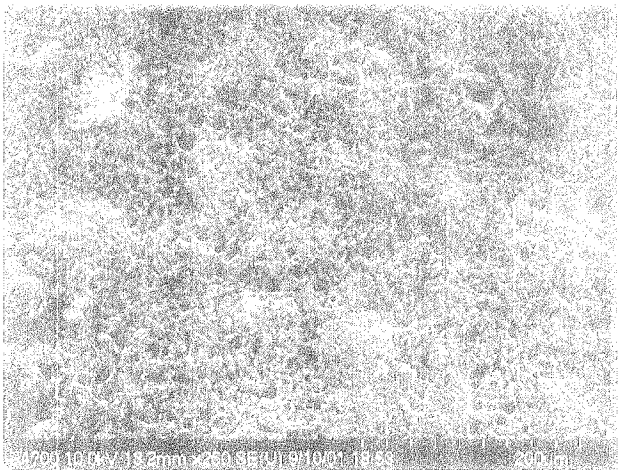

Oxidized at 900°C and metal dusted at 593°C (1100°F)

Fig. 64. SEM photomicrograph of surface of ChromeFlexed Alloy 800 after 6eff oxidation at 900°C in air and (right) oxidation at 900°C followed by metal dusting exposure for 142 h at 593°C.

of metal dusting degradation of the alloy. The first is influenced by a_{C} in the gas mixture and availability of the catalytic surface for carbon-producing reactions to proceed. There may be a threshold in a_{C} (≈ 1) for carbon deposition. Metal dusting of the alloy in the reformer environments is determined by a competition between the oxide scale development and access of the virgin metal surface to the carbon deposit. The presence of an oxide scale may not prevent metal dusting but can delay its initiation, thereby slowing the overall attack.

The local nature of dusting (initiated by pits on the alloy surface) on both Ni- and Fe-base alloys shows that defects in the oxide scales play a large role in initiation. Oxide scaling may not occur if a_{C} is low and/or if the H_2O content in the environment is very low. Laboratory experiments have clearly indicated the effect of gas chemistry (in particular H_2O content) in the scaling, carbon deposition, and dusting initiation. It is evident that the environment in reformers is high enough in pO_2 that a Cr-rich alloy can develop a chromia scale (given enough exposure time) before carbon deposition.

Surface modification by preoxidation and/or coatings and alternative materials are being examined at ANL to alleviate the metal dusting problem. Oxide coatings have the advantage in that they can minimize carbon-producing reactions (by reducing the availability of catalytic surface) and can also act as a barrier to minimize carbon ingress and pitting of the substrate alloy. We have selected in situ development of oxide scales, pack diffusion of Al or Cr/Si, and thermal spray of FeAl as avenues for further

study. Preliminary tests showed virtually no carbon in pre-oxidized layers of Al-, Cr-, and Si-enriched layers that were subjected to metal dusting environments.

The effort at ANL will emphasize the competitive nature of oxidation and carbon deposition and will assess the options for mitigating metal dusting in waste-heat boilers and eventually eliminating the boilers from the reformer systems, especially for H_2 production.

ACKNOWLEDGMENTS

This work was sponsored by the U.S. Department of Energy, Office of Industrial Technologies, and Dr. Charles Sorrell was the Program Manager for the project. Specimens of various alloys were supplied by Haynes International, AvestaPolarit, Sandvik Steel, Special Metals, Allegheny Ludlum, and Krupp VDM. Alon Surface Technologies supplied the specimens with pack-diffusion layers.

REFERENCES

1. P. A. Lefracois and W. B. Hoyt, Corrosion **19** (10), 360, 1963.

2. R. F. Hochman, Proc. 4th Intl. Congress on Metal Corrosion, N. E. Hammer, ed., NACE, p. 258, 1972.

3. R. C. Scheler, Hydrocarb. Process. **51**, 73, 1972.

4. R. F. Hochman, Proc. Symp. on Properties of High-Temperaure Alloys with Emphasis on Environmental Effects, Z. A. Foroulis and F. S. Pettit, eds., Electrochem. Soc., Pennington, NJ, p. 715, 1977.

5. H. J. Grabke, U. Gravenhorst, and W. Steinkusch, Werkst. Korros. **27**, 291, 1976.

6. H. J. Grabke, J. Hemptenmacher, and A. Munker, Wekst. Korros. **35**, 543, 1984.

7. H. J. Grabke and I. Wolf, Mater. Sci. Eng. **87**, 23, 1987.

8. R. A. Perkins, W. C. Coons, and F. J. Radd, Properties of High-Temperature Alloys, Electrochem. Soc., Pennington, NJ, 733, 1976.

9. H. J. Grabke, Mat. Corr. **49**, 303, 1998.

10. E. Q. Camp, C. Phillips, and L. Gross, Corrosion, **1**, 149, 1945; and **15**, 627, 1959.

11. R. E. Franklin, Acta Cryst. **4**, 253, 1951.

12. H. Krebs, *Fundamentals of Inorganic Crystal Chemistry*, McGraw-Hill, New York, p. 150, 1968.

13. R. O. Dillon and J. A. Woollam, Phys. Rev. B **29**, 3482, 1984.

14. F. Tuinstra and J. L. Koenig, J. Chem. Phy. **53**, 1126, 1970.

15. M. Nakamizo, H. Honda, M. Inagaki, and Y. Hishiyama, Carbon **15**, 295, 1977.

16. M. Nakamizo, H. Honda, and M. Inagaki, Carbon **16**, 281, 1978.

17. D. R. Lide, *CRC Handbook of Chemistry and Physics*, CRC Press, Boca Raton, FL, P12-119 to P12-123, 1999.

18. H. E. Blayden, H. L. Riley, and A. Taylor, J. Am. Chem. Soc. **62**, 180-186, 1940.

19. W. D. Schaeffer, W. R. Smith, and M. H. Polley, Ind. Eng. Chem. **45**, 1721, 1953.

20. C. R. Kinney, Proc. Conf. on Carbon, U. of Buffalo, p. 83, 1956.

21. F. Tuinstra and J. L. Koenig, J. Chem. Phy. **53**, 1126-1130, 1970.

22. R. J. Nemanich and S. A. Solin, Solid State Comm. **23**, 417-419, 1977.

23. R. Al-Jishi, Phys. Rev. B **26** 4514-4522, 1982.

24. R. Vidano and D. B. Fischbach, J. Amer. Ceram. Soc. **61**, 13-17, 1978.

25. D. S. Knight and W. B. White, J. Mater. Res. **4**, 385-393, 1989.

26. R. J. Nemanich and S. A. Solin, Phys. Rev. B **20**, 392-401, 1979.

27. Y. Sato Y, M. Kamo, and N. Setaka, Carbon **16**, 279-280, 1978.

28. C. M. Chun, J. D. Mumford, and T. A. Ramanarayanan, Mat. Corr. **50**, 634-639, 1999.

29. M. Nakamizo, R. Kammereck, and P. L. Walker, Carbon **12**, 259-267, 1974.

30. R. Kammereck, M. Nakamizo, and P. L. Walker, Carbon **12**, 281-289, 1974.

31. T. P. Levi, N. Briggs, I. Minchington, and C. W. Thomas, NACE Corrosion 2001, Paper # 01375.

32. M. Maier, J. F. Norton, and P. D. Frampton, Mat. Corr. **49**, 330-335, 1998.

33. B. Baker and G. D. Smith, NACE Corrosion 2000, Paper # 257.

DISTRIBUTION LIST FOR ANL-02/05

Internal

V. Maroni
C. Marshall
K. Natesan (30)
R. Poeppel
W. W. Schertz
W. Shack
W. K. Soppet
R.W. Weeks
Z. Zeng
TIS Files

External

DOE/OSTI, for distribution (2)
ANL-E Library
ANL-W Library

L. Craig, Jr., Materials Technology Institute, St. Louis, MO 63141 (25 copies)
R. Jain, DOE Office of Industrial Technologies, Washington, DC 20585
D. Ozokwelu, DOE Office of Industrial Technologies, Washington, DC 20585
C. Russomanno, DOE Office of Industrial Technologies, Washington, DC 20585
D. Salem, DOE Office of Industrial Technologies, Washington, DC 20585
P. Scheihing, DOE Office of Industrial Technologies, Washington, DC 20585
C. Sorrell, DOE Office of Industrial Technologies, Washington, DC 20585
B. Valentine, DOE Office of Industrial Technologies, Washington, DC 20585